STRUCTURAL INSIGHTS INTO THE MECHANISM OF MOVEMENT OF THE HETERODIMERIC KINESIN KAR3VIK1

by

JULIA COPE

B.Sc. (Hons), University of Cape Town, 2005

A thesis submitted to the

Faculty of the Graduate School of the

University of Colorado in partial fulfillment

of the requirement for the degree of

Doctor of Philosophy

Department of Molecular, Cellular, and Developmental Biology

2011

This thesis entitled:

Structural insights into the mechanism of movement of the heterodimeric kinesin Kar3Vik1

written by Julia Cope

has been approved for the Department of

Molecular, Cellular, and Developmental Biology

_____

Dr Gia Voeltz, Ph.D., Chair of Committee

_____

Dr Andreas Hoenger, Ph.D., Thesis Advisor

Date _____

The final copy of this thesis has been examined by the

signatories, and we find that both the content and the form

meet acceptable presentation standards of scholarly work

in the above mentioned discipline.

Abstract

Cope, Julia (Ph.D., Molecular, Cellular, and Developmental Biology)

Structural Insights into the mechanism of movement of the heterodimeric kinesin Kar3Vik1

Thesis directed by Associate Professor Andreas Hoenger, Ph.D.

The microtubule-associated motor, Kar3 is a minus-end directed kinesin-14 with important roles in mitosis in *Saccharomyces cerevisiae. In vivo* Kar3 forms a heterodimer with Vik1, a non-motor protein that regulates Kar3's localization and function. Unexpectedly, Vik1 has a structure similar to a kinesin motor domain but lacks an active site for ATP hydrolysis. Despite being unable to hydrolyze ATP, Vik1 was shown by cosedimentation to bind tightly to microtubules supporting a model where both Kar3 and Vik1 interact with the microtubule during Kar3Vik1's motility cycle. As it is the hydrolysis of ATP that allows kinesins to dissociate from the microtubule, the way Kar3Vik1 is able to facilitate motility was not known. This work aimed to identify a novel motor-microtubule interaction and obtain insight into Kar3Vik1's mechanism of movement along microtubules. Using cryo-EM I have shown that Kar3Vik1 binds to microtubules in a highly cooperative fashion through only one of its globular domains. Employing helical reconstruction of Kar3Vik1 bound to microtubules in various nucleotide states, I have revealed that Kar3Vik1 undergoes a large conformational change upon uptake of ATP that results in ~90° rotation of Kar3Vik1's coiled-coil stalk. This stalk rotation likely represents the powerstroke used by Kar3Vik1 for movement. Using a Nanogold® label, I have demonstrated that Kar3 contacts the microtubule to facilitate this powerstroke. Analysis of Kar3Vik1 constructs with crosslinks engineered to constrain the heterodimer at specific locations provided further insight into the conformational changes that take place during Kar3Vik1's

powerstroke. While I have made a significant contribution to our understanding of Kar3Vik1's force generating mechanism for movement, I was not able to visualize Vik1 binding to microtubules. My findings thus suggest that Kar3Vik1 does not move along microtubules in a way that is novel, but instead provide evidence for conservation of a motility mechanism among minus end directed motors.

Acknowledgements

I am grateful to many people who have contributed positively to my training and experience as a graduate student. I thank my advisor, Andy Hoenger, not only for his guidance and advice throughout my research, but also for the numerous opportunities he has given me that I may not have had in other labs. I am further grateful for his strong support of my data when others disagreed, and for his positive reinforcement which I believe is not a common trait among PIs.
To all the members of the BL3DEMC who have constantly impressed me with their wisdom and experience. Cindi Schwartz trained me on all aspects of cryo-EM and helped me in my initial work with PEET, Mary Morphew has answered endless questions about sample preparation and tomography and Eileen O'Toole has saved me time with helpful IMOD tips. They made me feel welcome in the lab and were a strong source of encouragement throughout my research. I am indebted to David Mastronarde who was instrumental to many aspects of my work. He helped me with the application of PEET and analysis of the subvolume averaging data, aided in the complicated installation of the helical reconstruction software, and created new programs at my request, such as those used for difference mapping. I thank John Heumann for his insight and patience in answering all of my PEET-related questions and for his help (and phenomenal spell-checking abilities) when writing our book chapter. I am glad to have been able to work with previous BL3DEMC lab members Mark Ladinsky and Jason Pierson who taught me the fine art of cryo-sectioning and cellular cryo-ET, Sacha de Carlo for teaching me 3D reconstruction methods, and Cynthia Page for advice on working with vimentin.
In the Hoenger Lab, I am grateful to Maria Pagratis for her hard work in the cloning and purification of the proteins used for the work presented in Chapter 5, and also for teaching me many molecular biology techniques. I have true appreciation for Robert Kirmse and Cédric Bouchet-Marquis who have been sources of valuable scientific discussion as well as endless laughter and entertainment. I especially thank Robert for taking the time to read and critique my thesis. Maria, Robert, Cédric and our other office mates over the years have been excellent colleagues and great friends who I will certainly miss when I leave Boulder.
Outside of our lab, it has been a privilege and an inspiration to receive insight from Dick McIntosh, and Paula Grissom in the McIntosh lab has provided me with sound advice and reagents. I am extremely grateful to Bridget Carragher at The Scripps Research Institute for help with installing the helical reconstruction software, and to Hernando Sosa and Ana Asenjo at the Albert Einstein College of Medicine for guidance with the ADP-AlF_4^- experiments. I thank the members of my thesis committee, Gia Voeltz, Mark Winey, Tin Tin Su and Greg Odorizzi for their time and suggestions over the years, and Hernando Sosa for his efforts to travel to Boulder to serve as my external committee member.
The majority of the work presented here was a productive collaboration with the labs of Susan Gilbert at Rensselaer Polytechnic Institute and Ivan Rayment at the University of Wisconsin, Madison. From the Gilbert lab, I acknowledge Rick Chen for the purified Kar3MD and Vik1MHD and Susan for experimental advice. From the Rayment lab, I thank Soheila Vaezeslami and Katherine Rank for sending me various constructs of Kar3Vik1 with which the bulk of the work in this thesis was conducted. The metal-precipitating peptide project reported in Chapter 5 was a collaboration with the lab of Daniel Feldheim at the University of Colorado, Boulder, and I worked together with Carly Carter on this interesting project.
Finally, I acknowledge financial support from the NIH/CU Predoctoral Traineeship Award in Molecular Biophysics T32-GM065103 and NIH/NCRR funding to A. Hoenger.

Table of Contents

List of tables

List of figures

List of abbreviations

3D - three-dimensional; 2D - two-dimensional

ADP - adenosine diphosphate

AMP-PNP - adenylyl imidodiphosphate tetralithium salt

ATP - adenosine triphosphate

DTT - dithiothreitol

EBI - N, N'-ethylene-bis(iodoacetamide)

EM - electron microscopy; Cryo-EM - cryo-electron microscopy

ET - electron tomography; Cryo-ET - cryo-electron tomography

FSC - Fourier shell correlation

HEPES - 4-(2-hydroxyethyl)-1-piperazineethanesulfonic acid

M4M - 1,4-butanediyl bismethanethiosulfonate

MT - microtubule

PIPES - piperazine-N,N′-bis(2-ethanesulfonic acid)

TCEP - tris(2-carboxyethyl)phosphine

WT - wild type

List of constructs used

Kar3MD	Kar3 C-terminal globular head (motor domain)
Vik1MHD	Vik1 C-terminal globular head (motor homology domain)
WT GCN4-Kar3Vik1	Wild-type sequence of Kar3 and Vik1 C-terminal heads and two and a half heptads of the Kar3Vik1 coiled-coil neck and stalk. The coiled-coil is preceded by the leucine-zipper sequence of the GCN4 transcription factor to initialize dimerization.
GCN4-Kar3$_{CL}$Vik1$_{C536C}$	Cysteine-light construct of WT GCN4-Kar3Vik1, where all cysteines have been replaced except for Cys^{536} on Vik1 for specific labeling with maleimide-Nanogold®.
GCN4-Kar3$_{E382C}$Vik1$_{K372C}$	Cysteine-light construct of WT GCN4-Kar3Vik1, where all cysteines have been replaced. Two residues at the base of the Kar3Vik1 coiled-coil have been replaced with cysteines for crosslinking with M4M, a 10Å chemical crosslinker.
SHD-Kar3Vik1$_{E355C-K423C}$	Cysteine-light construct of WT GCN4-Kar3Vik1, where all cysteines have been replaced. A residue in the Vik1 head and in the Vik1 coil have been replaced with cysteines for crosslinking with EBI, a 12Å chemical crosslinker. Instead of the GCN4 leucine zipper sequence, this construct has a synthetic homodimer sequence preceding the coiled-coil to initialize dimerization.

Chapter 1. Introduction

The Kinesin Superfamily

The kinesin superfamily is a large group of microtubule (MT) associated molecular motors that use the hydrolysis of ATP for movement along MTs and are responsible for carrying out a wide variety of essential functions in cells. The first member of the kinesin superfamily, kinesin-1, was discovered by Vale et al. (1985), who partially purified the motor from squid axoplasm and showed that it could translocate MTs in the presence of ATP (see also Brady et al., 1985). Since then, kinesins have been discovered in all model eukaryotes from yeast to humans and have been implicated in roles including organelle and protein transport, assembly and maintenance of the mitotic spindle, movement of chromosomes, and MT depolymerization, among many others (reviewed in Sharp et al., 2000; Hirokawa and Noda, 2008).

Though able to perform diverse roles, all kinesins share a defining feature: a ~360 amino acid globular domain known as the head (also referred to as the motor core) (Figure 1-1) (Hirokawa, 1998; Miki et al., 2005). This globular head contains an active site for binding and hydrolyzing ATP, as well as a specific site for binding to MTs. The head is highly conserved, both in sequence and in structure, across all kinesin superfamily members and across species. The position of the head domain, however, can differ (Lawrence et al., 2002; Hirokawa et al., 2009). The majority of kinesins have their head located at the N-terminus. These kinesins all show movement toward the MT plus end. Other kinesins have their head domain at the C-terminus and show movement toward the MT minus end. A third group of kinesins have their head located in the middle of the molecule and have been implicated in MT depolymerization.

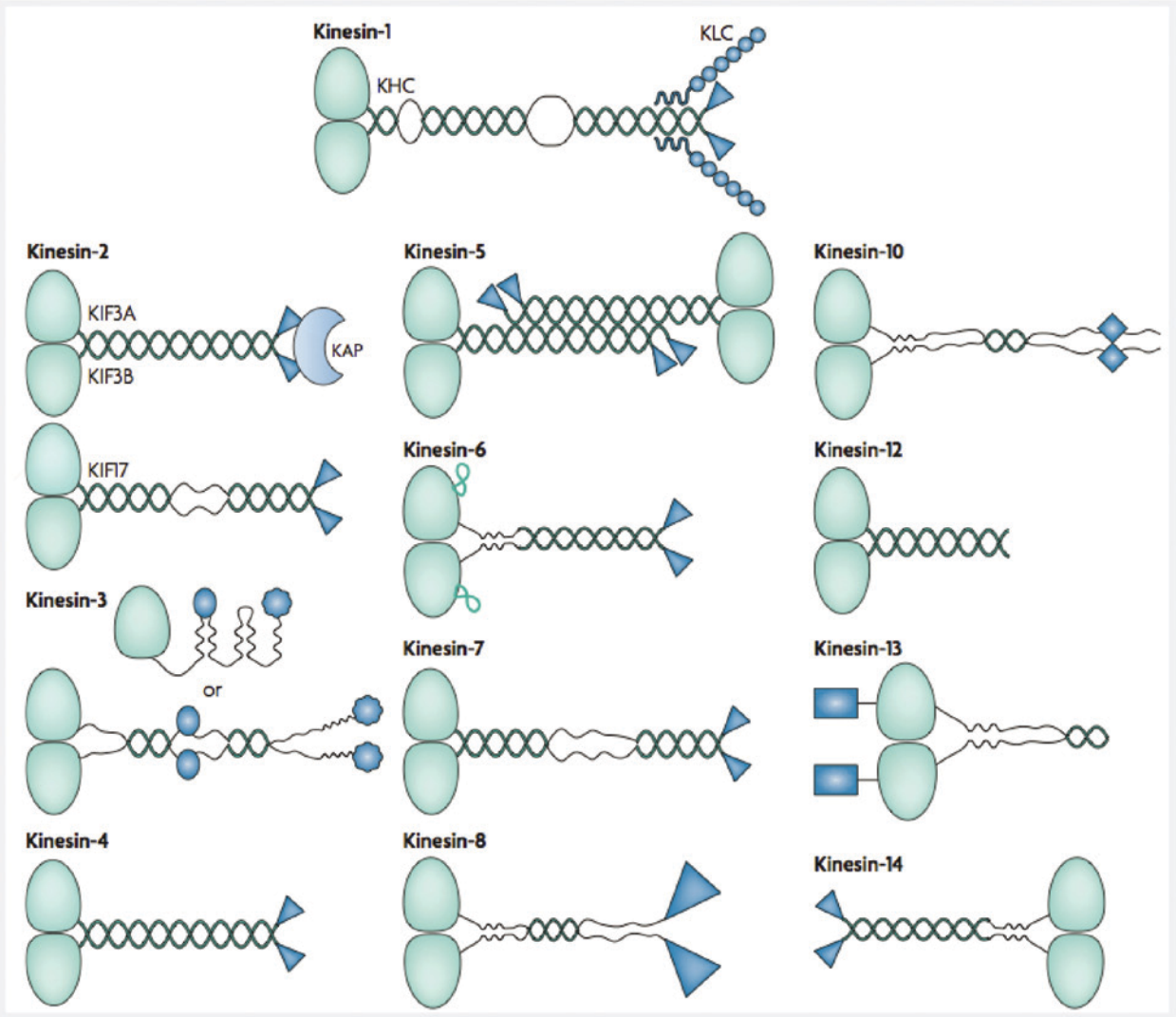

Figure 1-1: Domain organization of kinesin motors. Schematics showing the domain organization typical of kinesin superfamily members. All kinesins have a highly conserved head domain (green) that contains the site for ATP hydrolysis and MT binding. In most cases, the heads are joined by regions of coiled-coil to form dimers or tetramers. Regions outside of the head are diverse and contain family specific features directly related to motor function.

The relatively recent availability of sequence data has enabled a thorough phylogenetic classification of kinesins based on the amino acid sequences of their head domains (Figure 1-2) (Dagenbach and Endow, 2004; Miki et al., 2005). These analyses have identified 14 separate families that make up the kinesin superfamily. While the head is highly conserved, the overall domain organization of kinesins differs between families (Figure 1-1). In general, the globular head is followed by a short neck region. The neck sequence is family specific and there is evidence that this is the region responsible for determining the direction of motility (Vale and Fletterick, 1997; Rice et al., 1999). The neck is followed by a coiled-coil stalk region that facilitates oligomerization. Indeed the majority of kinesins form homodimers, while others form homo- or heterotetramers. The coiled-coil region is then followed by a non-catalytic tail region that is responsible for interacting with the motor's specific cargo (Figure 1-1) (reviewed in Hirokawa et al., 2009). Outside of the head domain, amino acid sequence differs between families and often each kinesin family has its own set of specific features that are directly related to their function (Figure 1-1). For example, members of the kinesin-10 family all possess a helix-hairpin-helix motif in their C-terminal region that may be responsible for their proposed ability to bind directly to, and facilitate movement of chromosomes (Tokai et al., 1996; Miki et al., 2005).

The structure of the MT track

Kinesins use MTs as their 'tracks' for movement. MTs are made up of two building blocks, α-tubulin and β-tubulin and αβ-tubulin heterodimers join axially head-to-tail to form a protofilament (Amos and Klug, 1974). Protofilaments then associate laterally in parallel to form the hollow tubule approximately 25 nm in diameter (Figure 1-3). The identical axial orientation

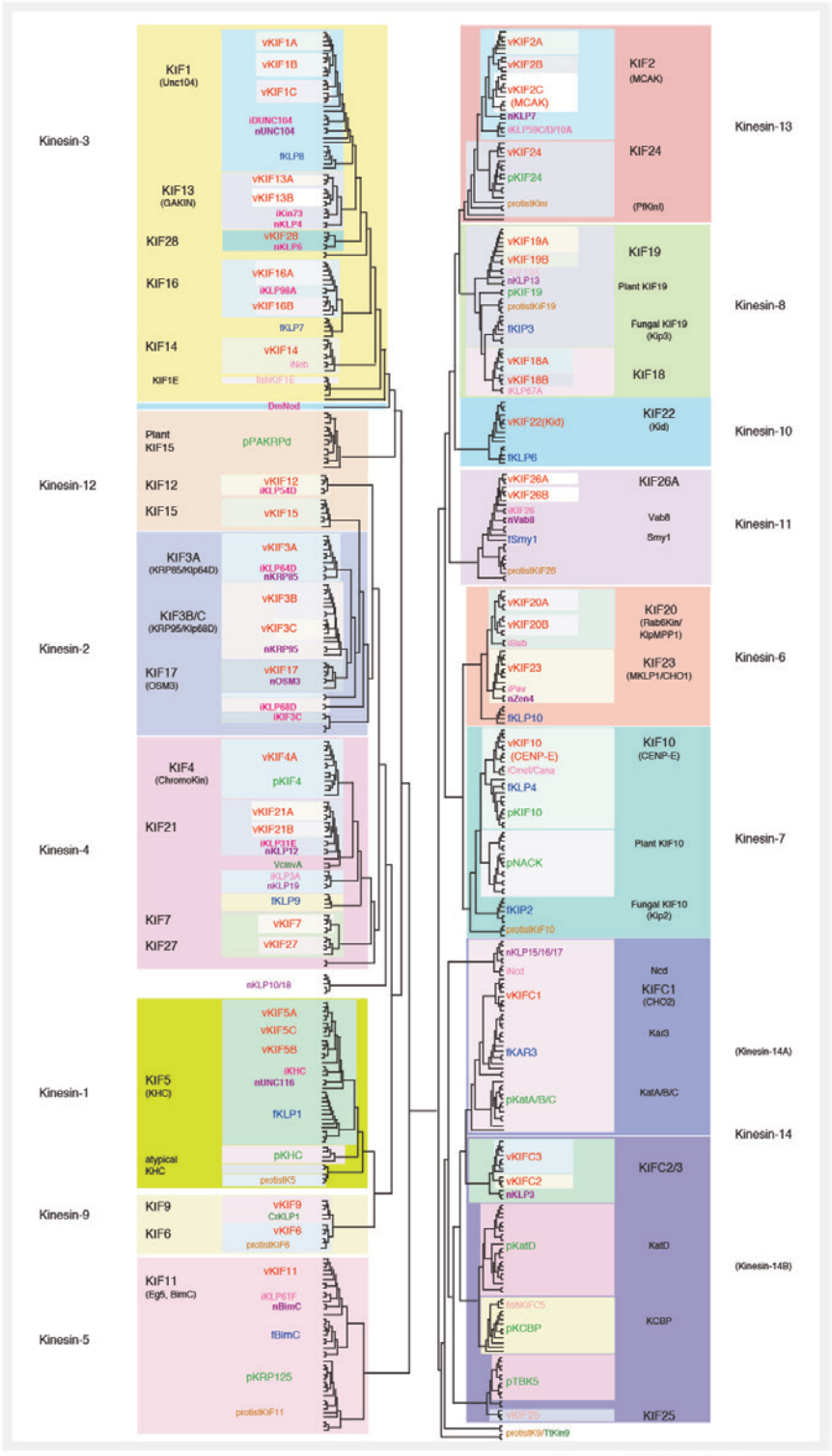

Figure 1-2: The kinesin superfamily tree. Phylogenetic tree constructed based on sequence alignment of the motor head domains of more than 600 kinesins. Kinesins classify into 14 families. Kar3Vik1 is a member of the kinesin-14 family. Taxa definitions are: v - vertabrate, i - insect, n - nematode, p - higher plant, f - fungi (Miki et al., 2005).

of tubulin dimers, and parallel lateral association of protofilaments gives MTs an intrinsic polarity. The polarity is such that β-tubulin is exposed at the MT plus end and α-tubulin is exposed at the MT minus end (Mitchison, 1993; Fan et al., 1996; reviewed in Desai and Mitchison, 1997). Although MTs are rigid polymers, they are highly dynamic and can quickly transition between states of rapid growth and shrinkage (Mandelkow et al., 1988; Mandelkow et al., 1989; reviewed in Howard and Hyman, 2009). The tight packing of tubulin subunits in the MT means that MT dynamics occur at the MT ends with growth and shrinkage taking place predominantly at the plus end (Howard and Hyman, 2003). As kinesins move unidirectionally along MTs, the polar arrangement of MTs is an integral part of kinesin function.

The lateral contacts between adjacent protofilaments in the MT was once a subject of much debate as two different lattice structures were proposed (reviewed in Amos, 1995; Mandelkow et al., 1995). An 'A-lattice' where an α-tubulin subunit contacts a β-tubulin subunit on the adjacent protofilament (Figure 1-3A), or a 'B-lattice' where an α-tubulin subunit contacts another α-tubulin subunit on the adjacent protofilament (Figure 1-3B). Initially, the A-lattice model was favored because MTs formed in this way would possess perfectly helical symmetry. However, with evidence from studies of kinesin-decorated MTs, it is now clear that MTs polymerize in a B-lattice with a 'seam', a break in the helical symmetry where A-lattice contacts exist between only two of the protofilaments (Figure 1-3B) (Song and Mandelkow, 1993; Mandelkow et al., 1986; Kikkawa et al., 1994; McIntosh et al., 2009). *In vivo*, MTs are predominantly comprised of 13 protofilaments and thus all have a seam (Tilney et al., 1973). MTs prepared *in vitro*, as used throughout this thesis, can assemble with 9 - 16 protofilaments, and most have seams (Chrétien and Wade, 1991). The exception is some 10-, 11-, 15- or 16-

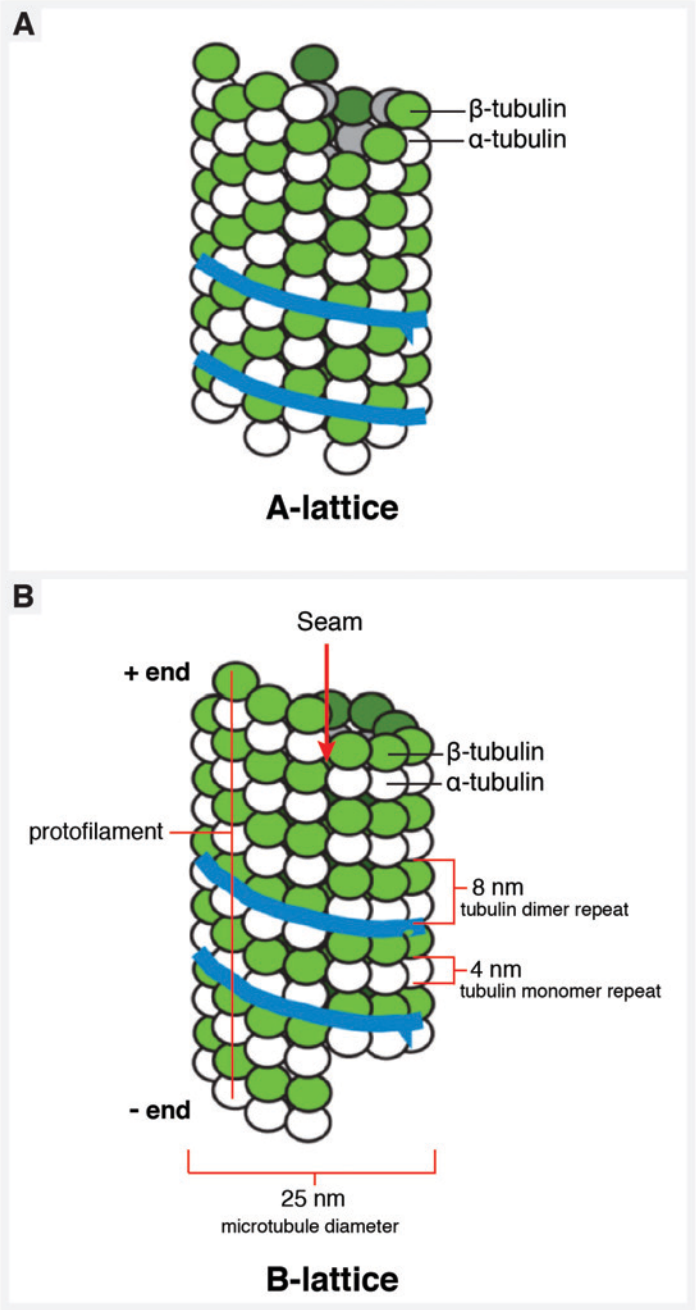

Figure 1-3: MT lattice structure. MTs are composed of dimers of αβ-tubulin that associate head-to-tail to form a protofilament. Protofilaments then join laterally, in parallel, to form a hollow cylinder. This structural arrangement gives MTs an intrinsic polarity with β-tubulin exposed at the MT plus end. Two proposed lattice structures have been debated. The A-lattice **(A)** where an α-tubulin contacts a β-tubulin on the adjacent protofilament, or the B-lattice **(B)** where a β-tubulin subunit contacts another β-tubulin subunit on the adjacent protofilament. A consequence of the B-lattice arrangement is the seam, a break in the helical symmetry where A-lattice contacts occur between one set of adjacent protofilaments. EM studies of kinesin-decorated MTs have provided evidence that MTs form B-lattices *in vitro* and *in vivo*.

protofilament MTs that form perfect helices with continuous B-lattice contacts (Sosa et al., 1997b; Dias and Milligan, 1999). Structural work is conducted throughout this thesis on both helical (Chapters 3 and 4) MTs, and MTs with lattice seams (Chapter 4).

Proposed mechanisms of movement for different kinesin motors

Much work has been done to investigate the mechanisms that different kinesins use for motility along MTs. However, as exemplified below in the case of kinesin-1, even with extensive experimentation, the results are not always straightforward. The proposed mechanisms of movement for two different, well-studied kinesins are described here.

Kinesin-1 (kinesin-1 family)

Kinesin-1 is a homodimeric, plus-end directed motor that is responsible for transporting membrane-bound organelles over long distances in the cell. It has been known for many years that kinesin-1 is a highly processive motor and that a single motor can take hundreds of steps before dissociating from the MT (Hackney, 1995). However, the precise stepping mechanism that kinesin-1 uses for movement along MTs has been a highly debated topic (reviewed in Schliwa et al., 2003). Commonly proposed models included a 'hand-over-hand' mechanism where the leading and trailing heads alternate between steps (Hackney, 1994), or an 'inchworm' mechanism where the leading head remains in front (Block and Svoboda, 1995). For a symmetric hand-over-hand mechanism where the trailing head would always pass the leading head in the same way, the motor's coiled-coil stalk (and its attached cargo) would have to rotate by 180° for every 8 nm step (Hoenger et al., 2000). Hua et al. (2002), have disproved this model by showing that MTs do not rotate more than ~45° by kinesin-1 molecules tethered by their necks to a glass

coverslip. Instead, they proposed that their findings were more consistent with an inchworm mechanism. For an inchworm mechanism only one molecule of ATP is hydrolyzed for an 8 nm advance along the MT, presumably in the leading head while the trailing head is dragged behind. To determine whether this was the case, Kaseda et al. (2003), created kinesin-1 heterodimers comprised of a wild-type head and a mutant head which hydrolyzes ATP much slower than the wild-type head. By optical trapping, they observed alternating fast and slow dwell times between steps consistent with the hand-over-hand model. Similar asymmetric steps were reported by Asbury et al. (2003). Yildiz et al. (2004), later used a fluorophore to specifically label only one head of a kinesin-1 molecule. With a high resolution fluorescence imaging technique, they showed ~17 nm displacements of the fluorophore, once again lending weight to a hand-over-hand model. Given the lack of rotation observed by Hua et al. (2002), the preferred model for kinesin-1 movement is now that of an asymmetric hand-over-hand mechanism where two mechanically different steps are required. The mechanical aspects involved in the asymmetry are not yet known though the possibility that torsion generated from one step could cause overwinding of the coiled-coil that is subsequently relieved by a step to the opposite side has been proposed (Hoenger et al., 2000; Asbury et al., 2003; Schliwa et al., 2003).

A variety of structural and mechanistic experiments with kinesin-1 have led to a motility model centered on nucleotide-state dependent conformational changes in a region directly adjacent to the motor head, known as the neck-linker (Gilbert et al., 1995; Rice et al., 1999; Hoenger et al., 2000; Asenjo et al., 2003; Skiniotis et al., 2003). Upon contact with the MT, the leading head loses ADP from its active site. Uptake of ATP into the leading head induces docking of the neck-linker onto the head, which causes the trailing head to swing forward to a binding site 16 nm away to become the leading head where it subsequently loses ADP from its

active site. Hydrolysis of ATP in the new trailing head converts it to a weakly bound state so it can swing forward when the new leading head binds ATP and docks the neck-linker. This tightly coordinated mechanochemical cycle ensures that one head of kinesin-1 is always in contact with the MT facilitating processive movement for long distances.

Ncd (kinesin-14 family)

Ncd is a homodimeric, minus-end directed motor that is required for proper chromosome segregation during meiosis and early mitosis in *Drosophila* (McDonald et al., 1990; Endow et al., 1990). Though Ncd is also homodimeric, its domain organization is reversed from that of kinesin-1 (McDonald et al., 1990). Ncd has its head domains at the C-termini that are followed by a short coiled-coil neck that extends directly into the coiled-coil stalk, and smaller globular cargo-binding domains at the N-termini. Motility experiments showed that Ncd moves along MTs much slower than kinesin-1 (Table 1-1) (Walker et al., 1990; Endres et al., 2006) and that ~4 Ncd motors are required to sustain movement of a MT (deCastro et al., 1999) while only a single kinesin-1 molecule can accomplish this (Howard et al., 1989). These observations provided evidence that Ncd does not move processively along MTs, and kinetic studies further suggested that Ncd is not chemically processive either (Foster and Gilbert, 2000).

Cryo-electron microscopy (cryo-EM) of Ncd homodimers demonstrated that the motor adopts a binding configuration very different from kinesin-1. In the nucleotide-free and ATP states, kinesin-1 can be seen binding to the MT with both of its motors heads simultaneously to two consecutive tubulin dimers along the same protofilament (Hoenger et al., 1998; Hoenger et al., 2000). Conversely, under the same nucleotide conditions, Ncd can be seen binding to the MT through only one of its heads with the second head oriented away from the MT (Sosa et al.,

1997a). Furthermore, sequence and structural data show that Ncd does not possess a neck-linker region that is essential for motility in kinesin-1. Instead, the coiled-coil neck extends directly from the heads and there appears to be interaction between the neck and the head domains (Sablin et al., 1998). Ncd studies have thus led to a motility model that when not bound to the MT, both Ncd heads contain ADP and have equal probability of making contact with the MT (Wendt et al., 2002). When one of the heads binds to the MT, it induces ADP release from its active site (Foster et al., 2001). Upon uptake of ATP into the bound head, the outer head and the coiled-coil stalk undergo a rotation of ~70° which repositions the stalk toward the MT minus-end and likely provides the force responsible for the anterograde motility (Wendt et al., 2002, Endres et al., 2006). Hydrolysis of ATP in the bound head weakens the affinity of Ncd for the MT and the motor detaches from the MT, most likely with P_i still in the active site (Foster et al., 1998). In this walking model it is believed that the unbound Ncd head that does not contact the MT, never loses ADP from its active site, though this is a still a subject of some debate (deCastro et al., 2000; Foster et al., 2001).

Kinesins involved in mitosis

At the onset of mitosis in all eukaryotic cells, a powerful complex machine, the mitotic spindle is formed. This MT-based structure is responsible for accurately segregating the chromosomes so each daughter cell receives a complete set. The basic features of the mitotic spindle are conserved among all eukaryotes. MTs organize into a bipolar array with their minus-ends focused into poles and their plus-ends extending toward the center (Figure 1-4). The plus ends of some MTs extending from opposite poles overlap with each other in an anti-parallel fashion at the spindle midzone (interpolar MTs). The plus ends of other spindle MTs connect to

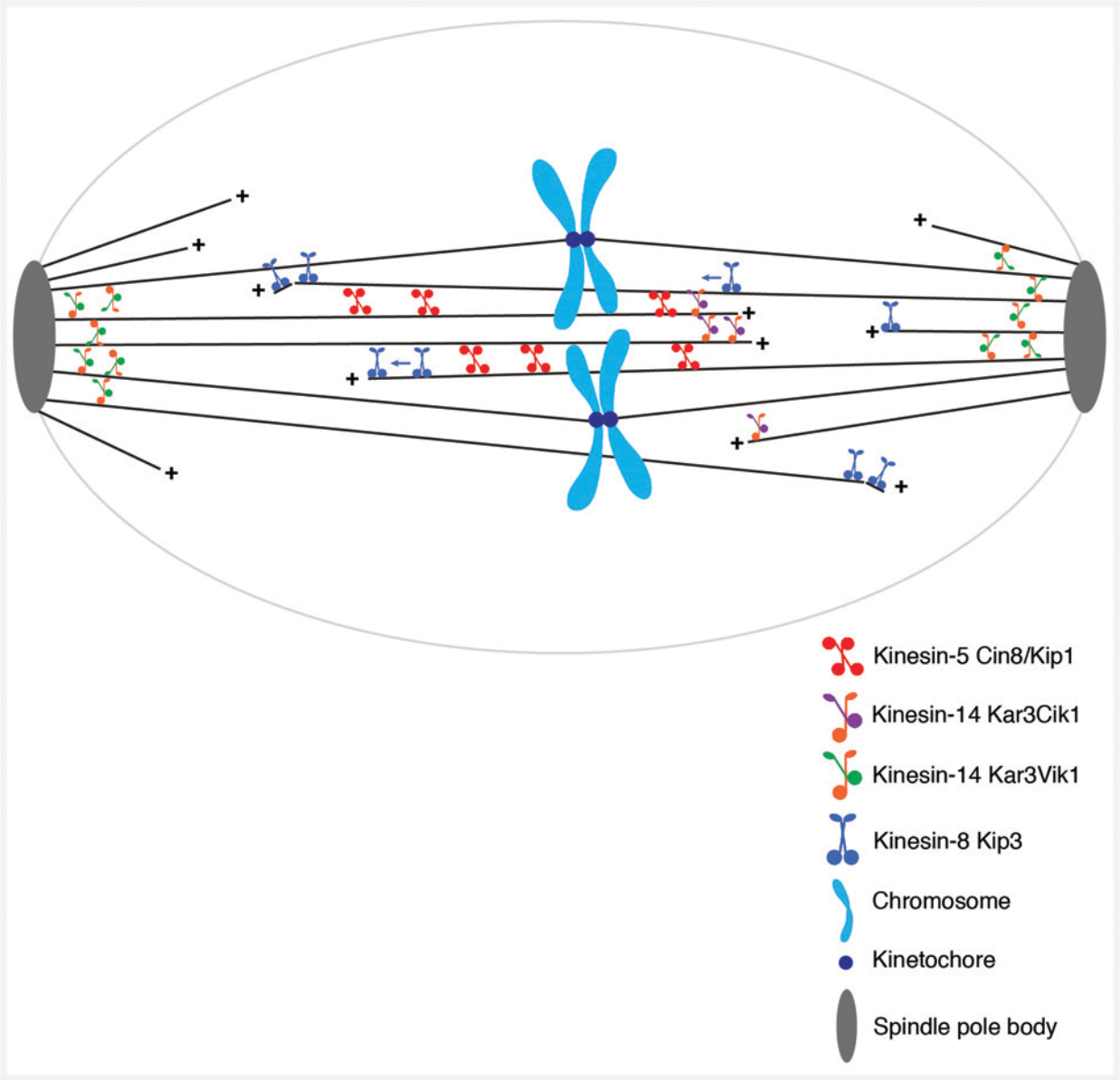

Figure 1-4: Localization of kinesins in the *S. cerevisiae* mitotic spindle. *S. cerevisiae* undergoes a closed mitosis where the nuclear envelope (light gray) remains intact. Interpolar MTs emanate from the spindle pole bodies and overlap in the spindle midzone, while kinetochore MTs attach to chromosomes at their kinetochores. Four of the six kinesins in *S. cerevisiae* localize to nuclear MTs in the mitotic spindle. The kinesin-5s Cin8 and Kip1 function redundantly to separate the spindle pole bodies at the onset of mitosis and crosslink antiparallel MTs overlapping in the midzone (Roof et al., 1992). Kar3Vik1 localizes to the spindle poles and crosslinks parallel MTs to focus the MT minus ends. Kar3Cik1 localizes to MT plus ends to crosslink antiparallel MTs in the midzone. The kinesin-8 Kip3 moves rapidly to MT plus ends where it waits until being bumped off by a second Kip3 molecule to cause MT depolymerization in a MT length-dependent manner (Varga et al., 2009).

the chromosomes (kinetochore MTs). In many organisms, spindle MTs emanate from MT organizing centers, the centrosomes (or the spindle pole bodies in yeast). However other organisms, such as many plant cells, lack centrosomes and indeed, bipolar spindles can still form in cells that have had their centrosomes inactivated (Megraw et al., 2001). The formation of the spindle thus relies on MT-interacting proteins that function to focus parallel MTs at the spindle poles, crosslink antiparallel MTs at the midzone and provide the force to push apart the poles and separate the chromosomes. Kinesins have fundamental roles in these processes. Indeed, of the six kinesins present in *Saccharomyces cerevisiae*, five of them have important roles in mitotic spindle function (Cottingham et al., 1999). The roles of two conserved families of kinesins involved in mitosis that are relevant to this thesis are described.

Kinesin-5

Kinesin-5s are plus end directed motors that comprise the most highly conserved kinesin family in eukaryotic model organisms (Miki et al., 2005). Kinesin-5 motors possess a homotetrameric structure, an antiparallel coiled-coil of two sets of parallel coiled-coil dimers (Figure 1-1) (Kashina et al., 1996). This domain organization results in the motor having two heads on each end. Kinesin-5 family members have essential roles in separation of the chromosomes at the onset on mitosis and subsequent formation of the bipolar mitotic spindle (Blangy et al., 1995). Deletion of kinesin-5 motors results in monopolar spindles and cells fail to proceed through mitosis (Enos and Morris, 1990; Heck et al., 1993; Blangy et al., 1995). Due to their bipolar structure, it was long proposed that kinesin-5s act by crosslinking MTs. Kapitein et al. (2005), showed that the *Xenopus laevis* kinesin-5, Eg5, could crosslink antiparallel MTs and move along both of them to slide them apart. They also reported that Eg5 could statically

crosslink parallel MTs and organize and align MT bundles. Thus, it is believed that kinesin-5s translocate to the plus ends of MTs at the onset of mitosis and begin to crosslink and arrange both parallel and antiparallel MTs to separate the centrosomes and assemble the bipolar spindle seen in metaphase (Figure 1-4) (Valentine et al., 2006). Once the spindle is in place, kinesin-5s may provide structural support and contribute to poleward flux by sliding antiparallel MTs apart towards the spindle poles (Miyamoto et al., 2004). Because of their essential role in mitosis, kinesin-5 motors are an attractive target for anti-cancer drugs. The small-molecule monastrol, has been discovered as a specific inhibitor of Eg5 and causes spindle collapse in mitotic cells (Mayer et al., 1999).

Kinesin-14

Kinesin-14 family members are minus-end directed motors. The majority of kinesin-14s form homodimers, though Kar3, the subject of this thesis, is the only known exception. One of the most researched kinesin-14s is *Drosophila* Ncd, whose domain organization and proposed mechanism of movement is described above. The N-terminal cargo-binding domains of kinesin-14s are basic, proline rich domains which bind to MTs in a non-ATP dependent manner, giving these motors the ability to crosslink MTs (Chandra et al., 1993; Karabay and Walker, 1999; Braun et al., 2009). Consistent with this, kinesin-14s are noted for their robust MT bundling activity *in vivo* and *in vitro* (Kuriyama et al., 1995; Oladipo et al., 2007; Cai et al., 2009). Localization and mutation analysis of kinesin-14 motors have led to the proposal that they function to focus the minus-ends of MTs at the spindle poles and crosslink antiparallel MTs in the spindle midzone (Endow et al., 1994a; Walczak et al., 1998; Mountain et al., 1999; Gardener et al., 2008). In support of this, recent work has reported that Ncd and Klp2, the kinesin-14s in

Schizosaccharomyces pombe, are able to crosslink and slide antiparallel MTs apart, but statically crosslink parallel MTs (Fink et al., 2009; Braun et al., 2009). In many organisms, deleting kinesin-14 can rescue the monopolar spindle phenotype that results from deleting kinesin-5 (Saunders and Hoyt, 1992; O'Connell et al., 1993; Mountain et al., 1999; Sharp et al., 1999; Troxell et al., 2001). This is strong evidence that kinesin-14 motors provide an inward force to antagonize the outward force provided by the kinesin-5s in the mitotic spindle.

Interestingly, the kinesin-14 in human cells, HSET is not required for cells to proceed through mitosis (Mountain et al., 1999). However, HSET has been shown to be essential for the survival of certain types of cancer cells that possess multiple centrosomes, making it an appealing target for cancer-specific therapeutics (Kwon et al., 2008).

Kar3Vik1 is an unusual heterodimeric kinesin

The content of this thesis focuses on my work with *S. cerevisiae* Kar3Vik1, an unusual heterodimeric kinesin-14 with only one motor domain (Kar3) whose activity is regulated through its association with a non-motor protein (Vik1). As for all kinesin-14 family members, Kar3 has a C-terminal motor domain and shows minus-end directed motion along MTs (Meluh and Rose, 1990; Endow et al., 1994b). *In vivo*, Kar3 forms a heterodimer through specific coiled-coil interactions with either Cik1 or Vik1, two non-motor proteins that differentially control Kar3 localization and function (Page et al., 1994; Manning et al., 1999). Kar3 interacts with Cik1 in response to mating pheromone where it functions during meiosis and is essential for nuclear fusion. Here, Kar3Cik1 localizes to cytoplasmic MTs and is thought to bring the nuclei together by depolymerizing MTs from their plus-ends (Sproul et al., 2005). Kar3Cik1 also has a separate function in the nucleus during vegetative growth where it localizes to the plus-ends of spindle

MTs and is thought to provide an inward force during spindle assembly (Figure 1-4) (Gardner et al., 2008). In contrast to Kar3Cik1, Kar3Vik1 is not expressed during meiosis and only functions during vegetative growth where it localizes predominantly at the spindle poles of the mitotic spindle (Figure 1-4) (Manning et al., 1999). Here, Kar3Vik1 is believed to crosslink parallel MTs, contributing to MT minus end focusing and stabilization of the spindle as proposed for other kinesin-14 motors (Allingham et al., 2007).

Unexpectedly, the X-ray crystal structure of the C-terminal globular domain of Vik1 revealed that it has a protein fold remarkably similar to a kinesin motor domain, but does not have an active site for ATP hydrolysis (Figure 1-5) (Allingham et al., 2007). Despite being unable to hydrolyze ATP, Vik1 was shown by equilibrium cosedimentation to be able to bind tightly to MTs *in vitro* (Allingham et al., 2007). Furthermore, the dissociation constant calculated from the cosedimentation experiments for Vik1 MT binding, was similar to that of Kar3Vik1 MT binding in the presence of ADP. This led the authors to speculate that Vik1 contacts the MT first while Kar3 has ADP in its active site, which is usually a weak MT binding state for kinesins.

Proposed models for how Kar3Vik1 may move along MTs

Based on the results described above, Allingham et al. (2007), have proposed two models for how Kar3Vik1 may move along MTs (Figure 1-6). In both models, Vik1 makes contact with the MT first and subsequent binding of Kar3 causes strain in Kar3Vik1's coiled-coil stalk which produces enough force to weaken Vik1's association with the MT so it can detach. Model A assumes that Kar3 and Vik1 both bind to the MT at β-tubulin in an orientation similar to other

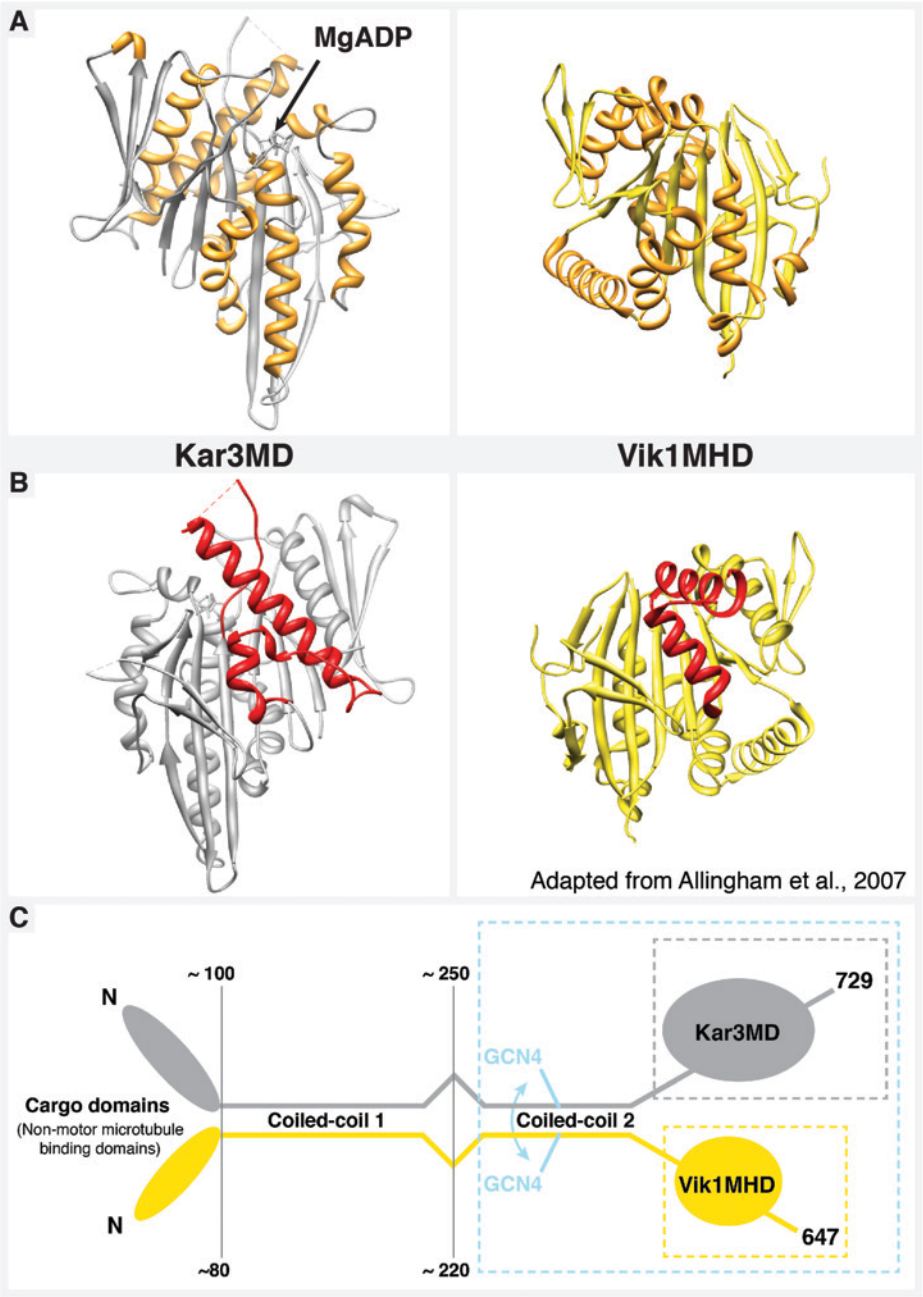

Figure 1-5: X-ray crystal structures of Kar3 and Vik1 and domain organization of Kar3Vik1. (A) Crystal structures of the C-terminal globular domains of Kar3 (left) and Vik1 (right). α-helices are colored orange to highlight the structural similarity of the two domains. **(B)** The crystal structures in **A** rotated 180°. The loops and helices on Kar3 involved in MT binding are colored red. The corresponding loops and helices on Vik1 are notably quite different from those in Kar3. **(C)** Schematic of Kar3Vik1's domain organization. Kar3 and Vik1 heterodimerize through two regions of coiled-coil. The N-terminal domains bind to MTs in a nucleotide-independent manner. GCN4-Kar3Vik1 used for work in this thesis is a truncated Kar3Vik1 construct that contains two and a half heptads of coiled-coil 2, preceded by the leucine zipper sequence from GCN4 which was added to initialize dimerization.

kinesins and interact with consecutive tubulin dimers along the same protofilament. Here, Kar3Vik1 may move by a hand-over-hand mechanism, similar to that described for kinesin-1, or by an inchworm mechanism where one domain remains in front. However, both these models require that the coiled-coil between Kar3 and Vik1 unwind to accommodate the 8 nm distance between consecutive tubulin subunits. Model B favors conformational simplicity and assumes that the neck coiled-coil does not unwind. Here Kar3 and Vik1 are proposed to interact with tubulin subunits on adjacent protofilaments. This walking mechanism requires that Vik1 bind to tubulin in an orientation different from Kar3 and other kinesins. This possibility may be supported by the Kar3 and Vik1 crystal structures that show notable differences in their loops and helices predicted to be involved in MT binding (Figure 1-5B).

My thesis research has aimed to determine the mechanism that Kar3Vik1 uses for minus end directed motility along MTs. Given reports of Vik1's surprising ability to bind to MTs, my work aimed to uncover a novel motor-MT interaction and a stepping mechanism unique from those described for other kinesins.

Kinesin	MT gliding rate	Direction of Movement	Reference
Kar3Vik1	3.14 ± 0.05 μm/min	To minus end	Allingham et al., 2007
Kar3Cik1	2.4 ± 0.06 μm/min	To minus end	Sproul et al., 2005
Ncd	9.0 ± 1.2 μm/min	To minus end	Endres et al., 2006
Kinesin-1	45.6 ± 6 μm/min	To plus end	Hancock et al., 1998

Table 1-1: Comparison of rates at which different kinesins can glide MTs *in vitro*. The kinesin-14s Kar3Vik1, Kar3Cik1 and Ncd have been shown to be non-processive and glide MTs significantly slower than the highly processive kinesin-1.

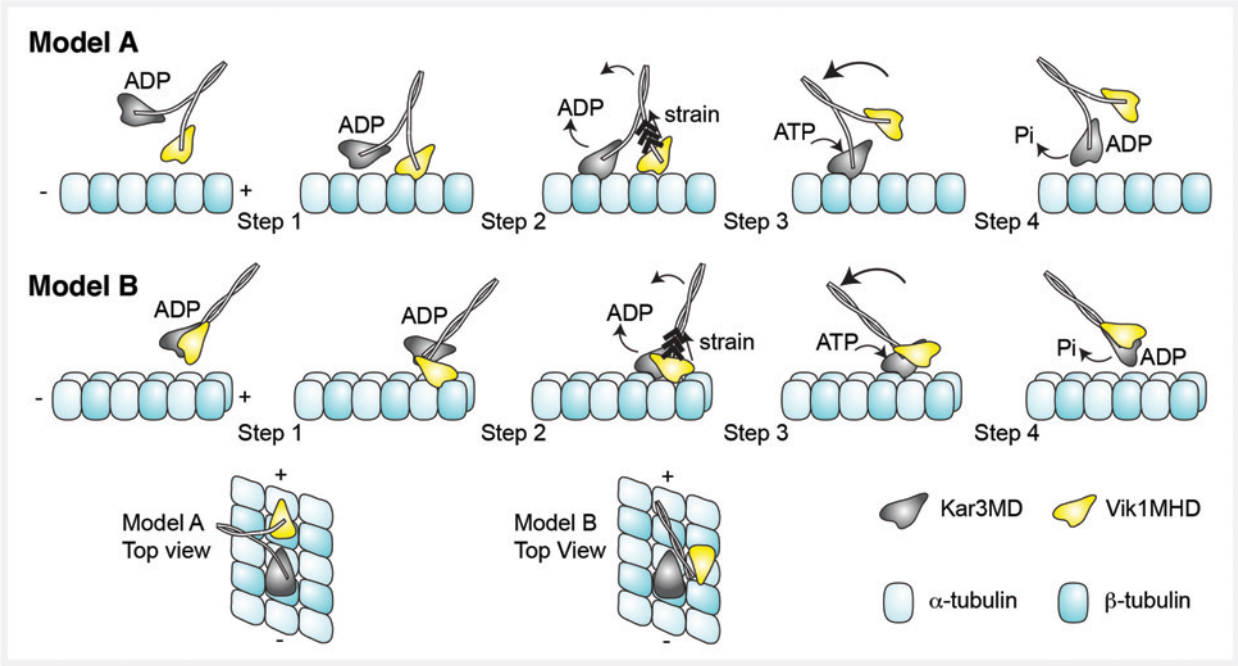

From Rank et al., submitted; adapted from Allingham et al., 2007

Figure 1-6: Proposed mechanisms for Kar3Vik1 movement along MTs. Allingham et al. (2007), proposed two models for how Kar3Vik1 may move along MTs based on equilibrium cosedimentation results that suggest that Vik1 interacts with MTs. In Model A, Kar3 and Vik1 are proposed to both bind in a canonical kinesin orientation to adjacent β-tubulin subunits along the same protofilament. This model requires that the coiled-coil neck between Kar3 and Vik1 unwind to be able to reach the 8 nm distance between the subunits. In Model B, the coiled-coil remains intact and instead proposes that Kar3Vik1 binds to tubulin subunits on adjacent protofilaments, implying that Vik1 adopt a binding pattern very different from a kinesin. In both models, Vik1 contacts the MT first while Kar3 is tethered with ADP bound in its active site. Kar3 then binds to the MT, producing strain in the coiled-coil that reduces Vik1's affinity for the MT so it can subsequently detach.

Chapter 2. The microtubule binding properties of the Kar3 motor domain, the Vik1 motor homology domain, and the Kar3Vik1 heterodimer as visualized by electron microscopy

Introduction

The MT binding properties of the Kar3 motor domain

Residues Leu^{383}-Lys^{729} constitute the Kar3 motor domain (Kar3MD), the C-terminal globular domain that includes Kar3's MT binding site and the active site for hydrolyzing ATP. Because it lacks the coiled-coil stalk region, Kar3MD exists as a monomer (Song and Endow, 1996). Kar3MD has been expressed and purified recombinantly for a variety of *in vitro* investigations that include MT binding assays (Song and Endow, 1996), kinetic analysis (Mackey and Gilbert, 2003; Mackey et al., 2004), and an X-ray crystal structure (Gulick et al., 1998). Cryo-EM and helical reconstruction has been used to study Kar3MD complexed to MTs in various nucleotide states to visualize the conformational changes that occur within the motor domain throughout Kar3's nucleotide hydrolysis cycle (Hirose et al., 2006). Sproul et al. (2005), used immunofluorescence microscopy to examine Kar3MD-MT complexes prepared *in vitro.* Their results showed that under sub-stoichiometric conditions (fewer Kar3MDs than binding sites on tubulin), Kar3MD appeared to bind stochastically to MTs. Allingham et al. (2007), later used immunofluorescence localization of Kar3Vik1 on *in vitro* prepared MTs to show that Kar3Vik1 binds to MTs in a cooperative fashion. This cooperative binding was illustrated by some MTs being saturated by Kar3Vik1 while adjacent MTs did not have any Kar3Vik1 bound. Here I describe my work to confirm the stochastic binding of Kar3MD to MTs at sub-saturating conditions by direct visualization with EM and show how this differs from Kar3Vik1's MT-binding pattern at sub-stoichiometric concentrations.

The MT binding properties of the Vik1 motor homology domain

Residues Thr^{353} - Thr^{647} form the C-terminal globular domain of Vik1. As this domain is structurally similar to that of a kinesin motor domain, but lacks a site for nucleotide hydrolysis, it has been termed the Vik1 motor homology domain (Vik1MHD) (Allingham et al., 2007).

Equilibrium cosedimentation experiments demonstrated that Vik1MHD was able to bind tightly to MTs ($K_{d\mathrm{MT}}$ = ~43 nM), implying that both Kar3 and Vik1 interact with the MT during Kar3Vik1's motility cycle (Allingham et al., 2007). In the highly conserved motor domain of kinesins, including Kar3, the region including helices α4 and α5 and loops 11 and 12 forms the MT binding site (Figure 1-5B, left) (Woehlke et al, 1997; Hirose et al 2006). These corresponding helices and loops in the Vik1MHD crystal structure are notably quite different from those in Kar3 and other kinesins (Figure 1-5B, right), indicating that Vik1 could bind to MTs at a site different from the kinesin binding site and possibly in a different orientation (Allingham et al., 2007). Thus, it was a major goal of this work to visualize Vik1MHD binding to MTs by cryo-EM and to obtain a detailed view for where on the MT lattice the Vik1MHD interactions occur.

The MT binding properties of Kar3Vik1

Previous work to visualize kinesins on MTs by cryo-EM has shown that kinesin heads across the different kinesin families all bind in the same orientation to the same site on the MT (Song and Endow, 1996; Hoenger and Milligan, 1997; Hoenger et al., 2000; Hirose et al., 2006; Bodey et al., 2009). However, homodimeric kinesins from different families have been shown to have remarkably different MT interacting properties. For example, homodimeric kinesin-1 binds to the MT with both of its motors heads simultaneously to two consecutive tubulin dimers along

the same protofilament (Hoenger et al., 2000). Similarly, homodimers (formed by truncation of the coiled-coil) of the tetrameric kinesin-5, Eg5 also bind along a single protofilament with both heads down on consecutive β-tubulin subunits (Krzysiak et al., 2006). In contrast, the homodimeric kinesin-14, Ncd binds to the MT with only one of its motors heads, with the second head remaining detached and extending outward away from the MT (Sosa et al., 1997a).

At the onset of my work, Kar3Vik1 bound to MTs had never been visualized by EM. The fact that Kar3 is a kinesin-14 closely related to Ncd, provided some basis to hypothesize that Kar3Vik1 would bind to MTs in a similar fashion. However, the evidence for Vik1 binding to MTs implies that Kar3Vik1 could also bind with both heads down on the MT as some point during its motility cycle. If a two-head-down state does indeed occur, it is not known whether the motor binds with both heads along the same protofilament, or along adjacent protofilaments.

Equilibrium cosedimentation experiments of Kar3Vik1 in the presence of ADP have reported that maximum MT binding is obtained with only 54% of the motors bound to the MTs (Allingham et al., 2007). This result could indicate that in the ADP state, Kar3Vik1 binds to the MT in such a way so as to prevent the binding of another motor at an adjacent binding site. Conversely, equilibrium cosedimentation experiments in the presence of AMP-PNP showed that 92% of Kar3Vik1 bound to MTs, suggesting that the MT-binding conformation of Kar3Vik1 changes to make all the sites on the MT available for motor binding (Allingham et al., 2007). This chapter describes my work to visualize Kar3Vik1's configuration relative to the MT lattice by trapping the motor in different nucleotide states. The results presented here are snapshots of motor-MT complexes taken at key points in Kar3Vik1's nucleotide-hydrolysis cycle which provides some preliminary insight into how Kar3Vik1 may move along MTs.

Cryo-EM as a tool to study motor-decorated MTs

In the early 1980's Dubochet and colleagues pioneered the technique of freezing samples rapidly enough (10^4 degrees/s) by plunging them into liquid ethane, to prevent specimen damage by ice crystal formation (Dubochet et al., 1981, Dubochet et al., 1988). While the properties, and particularly the formation of vitreous ice are still somewhat elusive, the technique has been widely adopted as a means to preserve specimens as close to their native condition as possible (Dubochet, 2007). Rapid freezing allows for specimens to be immobilized and imaged in a fully-hydrated condition without the use of the dehydrating agents and contrast-generating stains used in plastic-section or chemical fixation EM. This gives the advantages of superior specimen preservation and the potential to resolve much finer details. For these reasons, cryo-EM has been the primary method used for the structural studies on Kar3Vik1-decorated MTs presented here.

Materials and Methods

MT polymerization

MTs were polymerized *in vitro* from 45 μM bovine brain tubulin (Cytoskeleton, Inc., Denver, CO) with BRB80 (80 mM PIPES, pH 6.8, 1 mM MgCl2, 1 mM EGTA) in the presence of 1 mM GTP, 10 μM paclitaxel (Sigma, St. Louis, MO) and 7.5% (v/v) DMSO for 30 min at 35°C, and allowed to stabilize overnight at room temperature. MTs were always used within 24 hours after polymerization at 35°C

Expression and purification of Kar3MD and Vik1MHD

Kar3MD and Vik1MHD were expressed and purified in the lab of Susan Gilbert at Rensselaer Polytechnic Institute, Troy NY as described previously (Kar3MD: Mackey et al., 2004;

Vik1MHD: Allingham et al., 2007). The Kar3MD contains residues Leu^{383}-Lys^{729} of wild-type (WT) Kar3 which corresponds to the entire head domain highly conserved across all kinesin family members. The Vik1MHD contains residues Thr^{353} - Thr^{647} of WT Vik1 which corresponds to Vik1's C-terminal globular domain and is the same construct used for solving the Vik1MHD crystal structure (Allingham et al., 2007).

Expression and purification of WT GCN4-Kar3Vik1

WT GCN4-Kar3Vik1 was expressed and purified in the lab of Ivan Rayment at the University of Wisconsin, Madison WI similarly to previously reported methods (Sproul et al., 2005, Allingham et al., 2007). WT GCN4-Kar3Vik1 is a truncated version of Kar3Vik1 containing residues Lys^{353} - Lys^{729} of Kar3, and Ser^{341} - Thr^{647} of Vik1. This includes the complete C-terminal globular domains of Kar3 and Vik1 and two and a half heptads of the native coiled-coil stalk through which Kar3 and Vik1 heterodimerize. To initialize dimerization, the leucine zipper sequence from the GCN4 yeast transcription factor was encoded onto the N-terminus of the truncated Kar3Vik1.

Vitrification of Kar3MD-MT and Vik1MHD-MT complexes for cryo-EM

Kar3MD-MT complexes were assembled directly on holey carbon C-flat grids (Protochips, Inc., Raleigh, NC). Polymerized MTs were diluted to 3.75 μM with BRB80. 5 μl of diluted MTs were allowed to adsorb to a holey carbon grid for 35-60 s and excess liquid was blotted away. Immediately, 18 μM Kar3MD in ATPase buffer (20 mM HEPES pH 7.2, 5 mM magnesium acetate, 50 mM potassium acetate, 0.1 mM EDTA, 0.1 mM EGTA, 1 mM DTT), and 2 mM AMP-PNP was added to the MTs for 90-120 s. To ensure a sample layer thin enough for cryo-

EM imaging, excess liquid was blotted away by holding a small piece of Whatman #1 filter paper flat against the back of the grid until enough liquid had been blotted away so the filter paper was spontaneously released. Immediately after blotting, Kar3MD-MT complexes were vitreously frozen by rapidly plunging the grid into a cup of liquid ethane using a home-made plunge-freezing device. Frozen samples were stored in liquid nitrogen until being transferred for imaging in the EM.

Vik1MHD was incubated with MTs and plunge-frozen in the same manner except that no nucleotide or nucleotide-analog was added.

Vitrification of WT GCN4-Kar3Vik1-MT complexes for cryo-EM

WT GCN4-Kar3Vik1-MT complexes were vitrified as described above for Kar3MD-MT complexes. Specifics for trapping the complexes in each nucleotide state are detailed.

ADP state

WT GCN4-Kar3Vik1 at a final concentration of 4 μM in ATPase buffer with 5% sucrose and 1 mM ADP was incubated at room temperature for 10 min. MTs at a final concentration of 5 μM with 40 μM paclitaxel were added to the WT GCN4-Kar3Vik1-ADP and incubated for a further 15 min. A droplet of WT GCN4-Kar3Vik1-ADP - MT complexes was applied to a holey carbon grid and vitrified as described above. These samples were prepared according to advice from Susan Gilbert so that EM results would be comparable to those obtained from cosedimentation experiments conducted in her lab.

Nucleotide-free state

The nucleotide-free state was achieved by incubating the motors with the ATP/ADP hydrolyzing enzyme, apyrase grade VII (Sigma, St. Louis, MO). WT GCN4-Kar3Vik1 was diluted to 4.5 μM with ATPase buffer and 1 unit of apyrase. The kinesin-apyrase mixture was incubated on ice for 30-45 min. 5 μl of WT GCN4-Kar3Vik1-apyrase was then added to MTs adsorbed on a holey carbon grid and allowed to incubate for 90-120 s before blotting and plunging into liquid ethane.

ATP state

WT GCN4-Kar3Vik1 was trapped in the ATP state using the non-hydrolyzable ATP analog adenylyl imidodiphosphate tetralithium salt (AMP-PNP) (Sigma, St. Louis, MO).
WT GCN4-Kar3Vik1 at a final concentration 8 μM in ATPase buffer was incubated with 2.2 mM AMP-PNP on ice for 10-30 min. 5 μl of WT GCN4-Kar3Vik1 complexed with AMP-PNP was added to MTs on a holey carbon grid and incubated for another 90-120 s before blotting and plunging as described above.

ADP+P_i state

The nucleotide transition state analog, ADP-AlF_4^- was used to mimic WT GCN4-Kar3Vik1 in a state following ATP hydrolysis, but prior to the release of inorganic phosphate from the active site. ADP-AlF_4^- was prepared using ADP, $AlCl_3$ and KF at final concentrations of 4 mM, 2 mM and 30 mM respectively in PME buffer (10 mM PIPES, 5 mM $MgCl_2$, 1 mM EGTA) with 50 mM KCl (KF was prepared fresh in a plastic tube immediately before use). WT GCN4-Kar3Vik1 at a final concentration of 14 μM was added to the solution of ADP, $AlCl_3$ and KF and incubated for 2 min. MTs as a final concentration of 3.75 μM were added to the WT GCN4-

Kar3Vik1-ADP-AlF_4^- and allowed to incubate for 5-15 min. A droplet of the Kar3Vik1-ADP-AlF_4^--MT complexes was adsorbed to a holey carbon grid for 45 s, and then vitrified as outlined above.

Cryo-EM data collection

Plunge-frozen samples were transferred under liquid nitrogen to a Gatan-626 cryo-holder (Gatan, Inc, Pleasanton, CA). Cryo-EM data was collected on an FEI Tecnai F20 FEG transmission EM (FEI-Company, Eindhoven, The Netherlands) operating at 200 kV. Single frame images were collected at a nominal magnification of 29 000 x and a defocus of -2.5 μm with an electron dose of 15 electrons/$Å^2$. Images were recorded without binning on a 4K x 4K Gatan Ultrascan 895 CCD camera (Gatan, Inc, Pleasanton, CA). With this camera, at a nominal microscope magnification of 29 000 x the image pixel size corresponds to 3.8 Å on the specimen.

Negative stain of MTs with WT GCN4-Kar3Vik1-ADP or Vik1MHD

WT GCN4-Kar3Vik1-ADP and Vik1MHD were incubated with MTs as described for rapid plunge-freezing above, except that instead of plunging grids into liquid ethane, the grids were inverted onto a 7 μl droplet of NanoVan® (Nanoprobes, Yaphank NY) for 20-30 s. Excess stain was wicked away by touching the side of the grid to a piece of filter paper. If a wash was performed after staining, the sample was inverted onto a 20 μl droplet of MilliQ water for 10 s. Excess water was blotted away and grids were left to air-dry for 10-15 min. Specimens for negative-staining were applied to 200-mesh Formvar- and carbon-coated copper grids that were glow-discharged immediately prior to applying the sample. To test whether glow-discharging or

post-stain washing affected the binding of WT GCN4-Kar3Vik1 or Vik1MHD to MTs, samples were also prepared without glow-discharging the grids, and/or without washing after staining. Negatively-stained complexes were imaged on an FEI Tecnai F20 transmission EM operating at 200 kV. Images were collected at a nominal magnification of 50 000 x and a defocus of -1.5 μm with an electron dose of ~20 electrons/$Å^2$. Images were recorded binned by two on a 4K x 4K Gatan Ultrascan 895 CCD camera (Gatan, Inc, Pleasanton, CA) corresponding to a pixel size of 4.5 Å on the specimen.

Unidirectional heavy-metal shadowing of Kar3MD-MT and Vik1MHD-MT

Specimens were prepared for shadowing at the ETH in Zurich, Switzerland according to my protocol. Images of the shadowed samples were collected by Peter Tittmann (EMEZ, ETH-Zuerich Hoenggerberg, Switzerland).

Kar3MD-AMP-PNP and Vik1MHD were incubated with MTs and plunge-frozen essentially as described above. Kar3MD at a final concentration of 4.5 μM in ATPase buffer and 2 mM AMP-PNP was added to 3.75 μM MTs and incubated for 90-120 s. Vik1MHD at 14.5 μM in ATPase buffer was added to 3.75 μM MTs and incubated for 120 s. Following plunge-freezing, grids were freeze-dried and unidirectionally shadowed with tantalum/tungsten as described (Sandblad et al., 2006).

Results

Kar3MD binds stochastically to the MT lattice

Kar3MD was incubated with MTs in the presence of the non-hydrolyzable ATP analog, AMP-PNP at sub-stoichiometric conditions to test whether Kar3MD binds stochastically to MTs as previously reported by immunofluorescence (Sproul et al., 2005). By transmission cryo-EM,

the MTs appeared to be undecorated, and computational Fourier transforms of images did not reveal a 1/8 nm layer line. The 1/8 nm layer line corresponds to the real space distance between motor binding sites on a protofilament (the length of one αβ-tubulin dimer complexed to one motor) and is seen when motors bind at a regular repeat of 8 nm to the MT lattice. The undecorated appearance of the MTs and the absence of a 1/8 nm layer line in Fourier transforms both indicate that Kar3MD was binding randomly to the MT lattice, or was not binding at all.

To confirm that Kar3MD could indeed bind to MTs, MTs were incubated with 4 times more Kar3MD than available binding sites. By cryo-EM, MTs appeared fully decorated as determined by the presence of the regularly-spaced ridges along the sides of the MTs (Figure 2-1B). While difficult to see in the 2D-projections, the Kar3MD binding was confirmed by a clear 1/8nm layer line in Fourier transforms of the images (Figure 2-1B, right).

Unidirectional heavy metal shadowing was performed on MTs decorated with a sub-stoichiometric concentration of Kar3MD as described above to directly visualize the stochastic binding of Kar3MD to the MT lattice. Unlike transmission cryo-EM, freeze-drying of a plunge-frozen specimen followed by unidirectional shadowing permits visualization of the MT's surface features and any proteins attached to the MT exterior. By unidirectional shadowing, Kar3MD was seen to bind randomly to the MT lattice (Figure 2-1A) illustrating that Kar3 alone does not show cooperative binding behavior as it does when in a complex with Vik1 (described below). It is important to note that the binding of Kar3MD to the MT is only 'random' in the sense that it appears to be able to bind at any available kinesin binding site on the MT without showing a preference for a binding site adjacent to a site that is already occupied. In the context described here, 'random' binding should not be confused with 'non-specific' binding which describes an

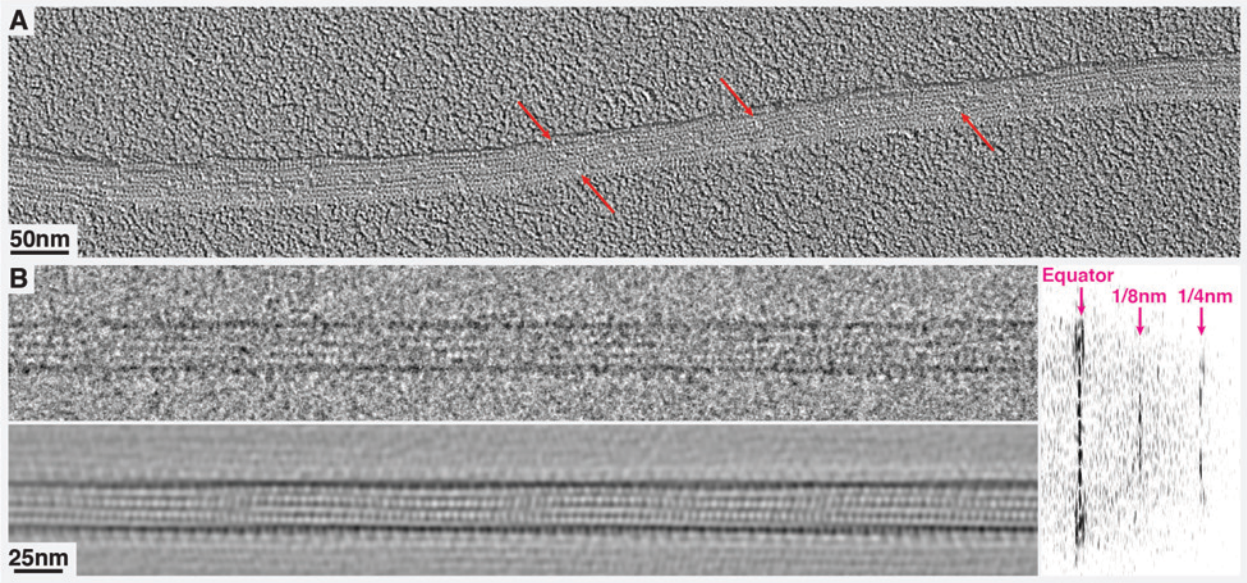

Figure 2-1: Kar3MD binds stochastically to the MT lattice. (A) In the presence of AMP-PNP, the binding of Kar3MD to the MT is non-cooperative as shown by unidirectional heavy-metal shadowing. The shadowing provides a view of the surface of the MT and the Kar3 motor domains appear as raised bumps (red arrows). **(B)** Cryo-EM of MTs incubated with a 4:1 molar ratio of Kar3MD:Kar3MD binding sites on tubulin show that at high concentrations, Kar3MD will saturate all the binding sites on the MT as seen in a projection of the decorated MT (top), but more clearly in the Fourier filtered image (bottom). The regular decoration of the Kar3MD every 8 nm along the MT is confirmed by the presence of the 1/8 nm layer line in the Fourier transform of the image (right).
Heavy metal shadowing of Kar3MD-MT complexes was performed by Andy Hoenger, and image was taken by Peter Tittmann at the ETH, Zurich, Switzerland.

interaction for a protein that may bind in different orientations and/or at inconsistent locations on the MT lattice.

Vik1MHD cannot be seen interacting with the MT by EM

Numerous and varied attempts were made to visualize the interaction between Vik1 and MTs. Initial work was done by cryo-EM (Figure 2-2A) using a variety of HEPES-based and PIPES-based buffers, different ratios of Vik1MHD to tubulin, and a range of incubation times. Despite closely mimicking the conditions described by others that support Vik1MHD binding (Allingham et al., 2007, S. Gilbert personal communication), Vik1MHD domains were never seen binding to MTs by cryo-EM.

It is possible that the percentage of decoration was too low (< 50%) to be seen by cryo-EM and so attempts were made to visualize Vik1MHD binding using negative stain EM (Figure 2-2B). The methylamine vanadate stain used here coats the proteins and causes strong deflections of the electron beam, generating greater contrast and making biological samples easier to see in the EM (though this comes at the cost of specimen dehydration, possible distortions of the sample and staining artifacts). In addition to various buffer conditions, samples were prepared on grids both with and without glow-discharging the grids prior to addition of the sample and both with and without a brief water wash following staining. Vik1MHD could not be seen binding to MTs under any of these conditions.

In addition to negative stain, heavy metal shadowing was performed to try to detect Vik1MHD on the MT surface. In nearly all images, the MTs appeared predominantly undecorated (Figure 2-2C). In a few cases, some proteins (~2-7 per image) can be seen on a MT,

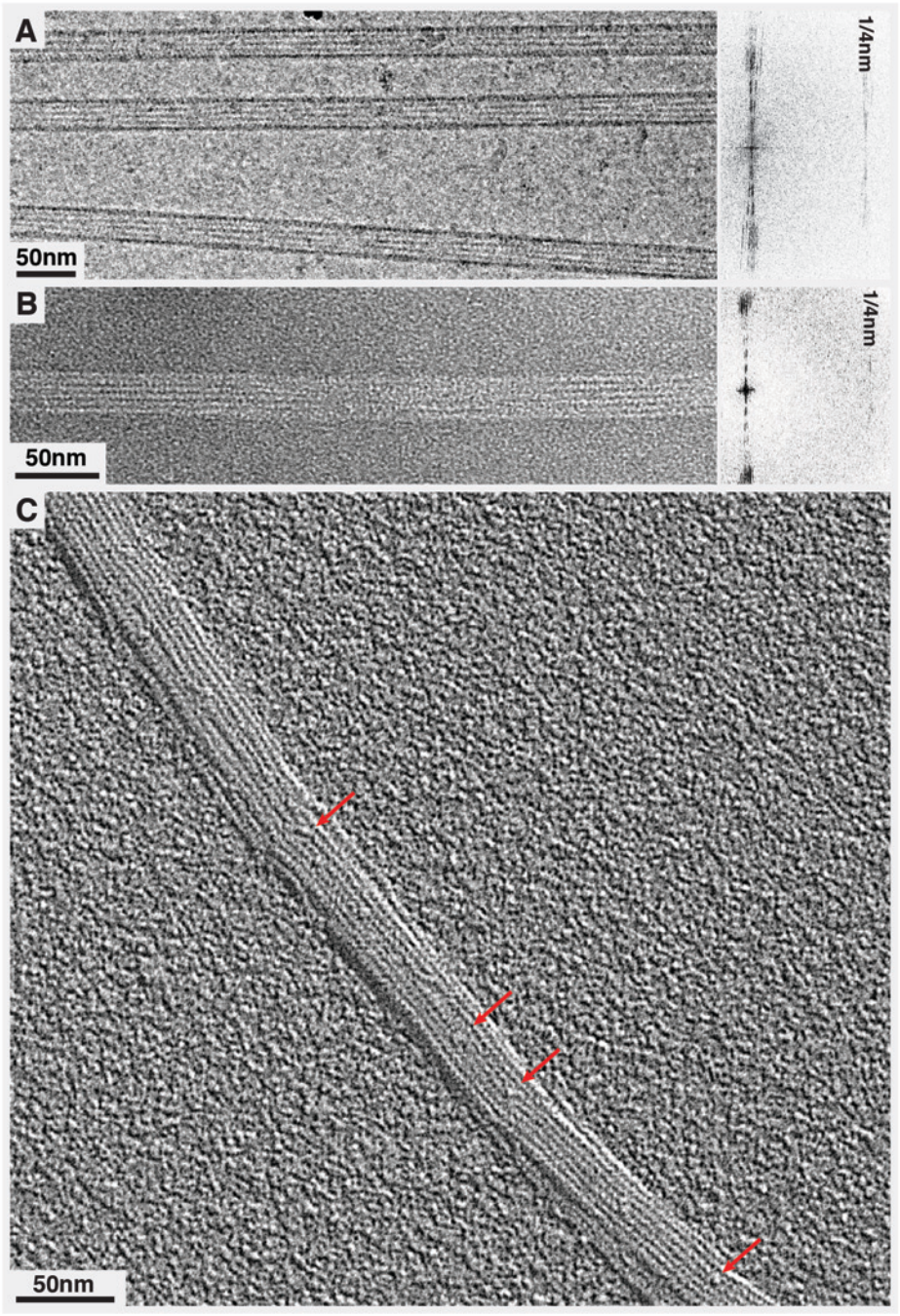

Figure 2-2: Vik1 cannot be seen binding specifically to MTs by various EM methods. Cryo-EM **(A)** and negative stain **(B)** of MTs incubated with Vik1MHD reveal undecorated MTs. The lack of a 1/8 nm layer-line also confirms the absence of a regular binding pattern by Vik1. **(C)** Unidirectional shadowing of MTs incubated with Vik1MHD shows ~6 bumps that may represent binding of Vik1MHD to the MT. However, this number is extremely low considering that Vik1MHD was added in a four-fold excess to the number of binding sites available on tubulin. *Heavy metal shadowing of Vik1MHD with MTs was performed by Andy Hoenger, and images were taken by Peter Tittmann at the ETH, Zurich, Switzerland.*

but they do not appear to bind with any regularity despite Vik1MHD being present in a four-fold excess to the number of binding sites available.

Kar3Vik1 cannot be seen binding to MTs in the ADP state by cryo-EM

ADP generally represents a weak MT binding state for kinesins. However, Kar3Vik1 has been shown by equilibrium cosedimentation to interact with MTs in the presence of ADP and it has thus been proposed that the heterodimer contacts the MT in this state through Vik1 (Allingham et al., 2007). As Vik1MHD alone could not be detected binding to MTs, I reasoned that I may be able to detect binding through Vik1 by examining WT GCN4-Kar3Vik1 complexed to MTs in the ADP state because the heterodimer is larger (thus easier to see) and because Vik1 likely possesses more native behavior when in a complex with Kar3.

Many attempts were made to visualize binding of WT GCN4-Kar3Vik1 to MTs in the presence of ADP. By cryo-EM, MTs incubated with WT GCN4-Kar3Vik1-ADP appeared completely undecorated except for a few noticeable densities appearing occasionally on the MTs that could indicate binding of the heterodimer (Figure 2-3A, Figure2-4A). Intriguingly, there was an unusually large number of tubulin sheets and stabilized protofilaments seen in the presence of WT GCN4-Kar3Vik1-ADP (Figure 2-3A). This could indicate binding of Kar3Vik1 to the MTs in a manner that stabilizes the interactions between protofilaments, but at a concentration that is too low to be seen by cryo-EM.

In addition to the standard methods of plunge-freezing described here, samples of WT GCN4-Kar3Vik1-ADP with MTs were also prepared on grids that had not been glow-discharged and were blotted for only a fraction of a second before plunging. These special measures were performed as described by Sindelar and Downing (2007) who developed these techniques after

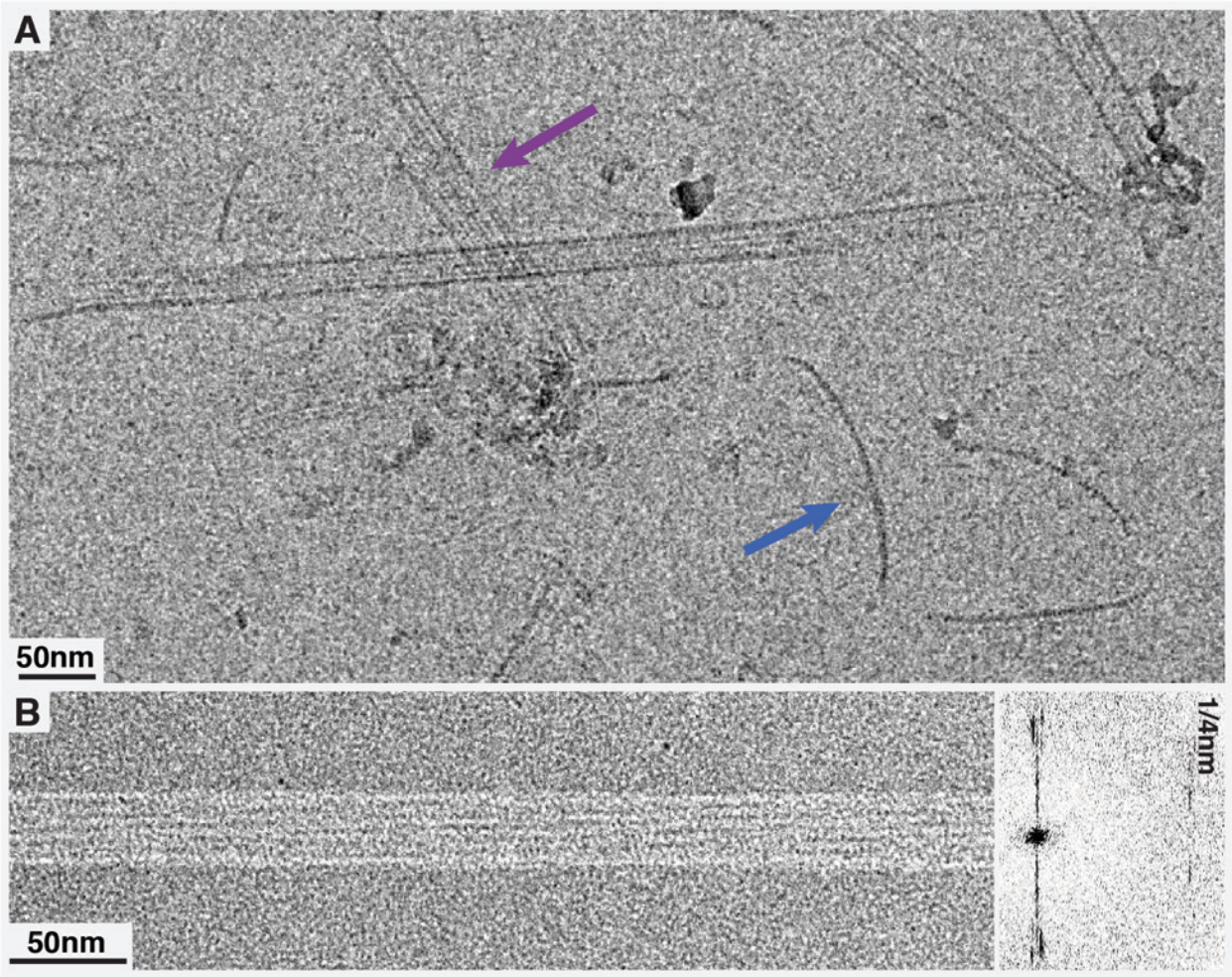

Figure 2-3: WT GCN4-Kar3Vik1 cannot be seen binding to MTs in the ADP state.
(A) MTs incubated with Kar3Vik1 in the presence of ADP, appear predominantly undecorated when visualized by cryo-EM. However, an unusually large number of tubulin sheets (purple arrow) and stabilized protofilaments (blue arrow) can be seen possibly indicating that some Kar3Vik1 is binding in a way that stabilizes interactions between protofilaments, but at a concentration that is too low to be seen. **(B)** Samples prepared in the same manner for negative stain-EM reveal naked MTs indicated by empty protofilaments in the image (left) and absence of a repeat other than the 1/4 nm layer line (corresponding to the tubulin monomer repeat) in the Fourier transform (right).

having difficulty preserving kinesin decoration on MTs during plunge-freezing. However, despite these precautions, WT GCN4-Kar3Vik1-ADP was not detected on MTs by cryo-EM. WT GCN4-Kar3Vik1-ADP samples prepared similarly with negative-staining also revealed predominantly naked MTs (Figure 2-3B).

Kar3Vik1 binds to MTs in a one-head-down, one-head-up binding configuration in the nucleotide-free, ATP and ADP+P_i states

Kar3Vik1 binding to MTs in the nucleotide-free state was examined by treating the motors with the ATP- and ADP-hydrolyzing enzyme apyrase, prior to incubation with the MTs. In this state, WT GCN4-Kar3Vik1 can be seen binding to the MT through only one of its globular domains, with the second globular domain extending away (Figure 2-4B). Similarly, WT GCN4-Kar3Vik1 incubated with AMP-PNP to trap the ATP-binding state, bound to the MT lattice in this one-head-down, one-head-up binding configuration (Figure 2-4C). Finally, WT GCN4-Kar3Vik1 was treated with ADP-AlF_4^- which is thought to mimic a state after the hydrolysis of ATP, but before the release of phosphate from Kar3's active site (Wittinghofer, 1997; Asenjo et al., 2003). In the ADP-AlF_4^- state, WT GCN4-Kar3Vik1 was also seen to bind to the MTs in the same asymmetric conformation seen with the nucleotide-free and AMP-PNP states (Figure 2-4D). In all states, Kar3Vik1 binds only once per αβ-tubulin dimer which is consistent with what has been reported for monomeric Kar3MD (Hirose et al., 2006) and also for dimeric Ncd (Sosa et al., 1997a; Wendt et al., 2002). In the 2D projections shown in Figure 2-4 it is impossible to know whether it is Kar3 or Vik1 in contact with the MT, though this is addressed in Chapter 3.

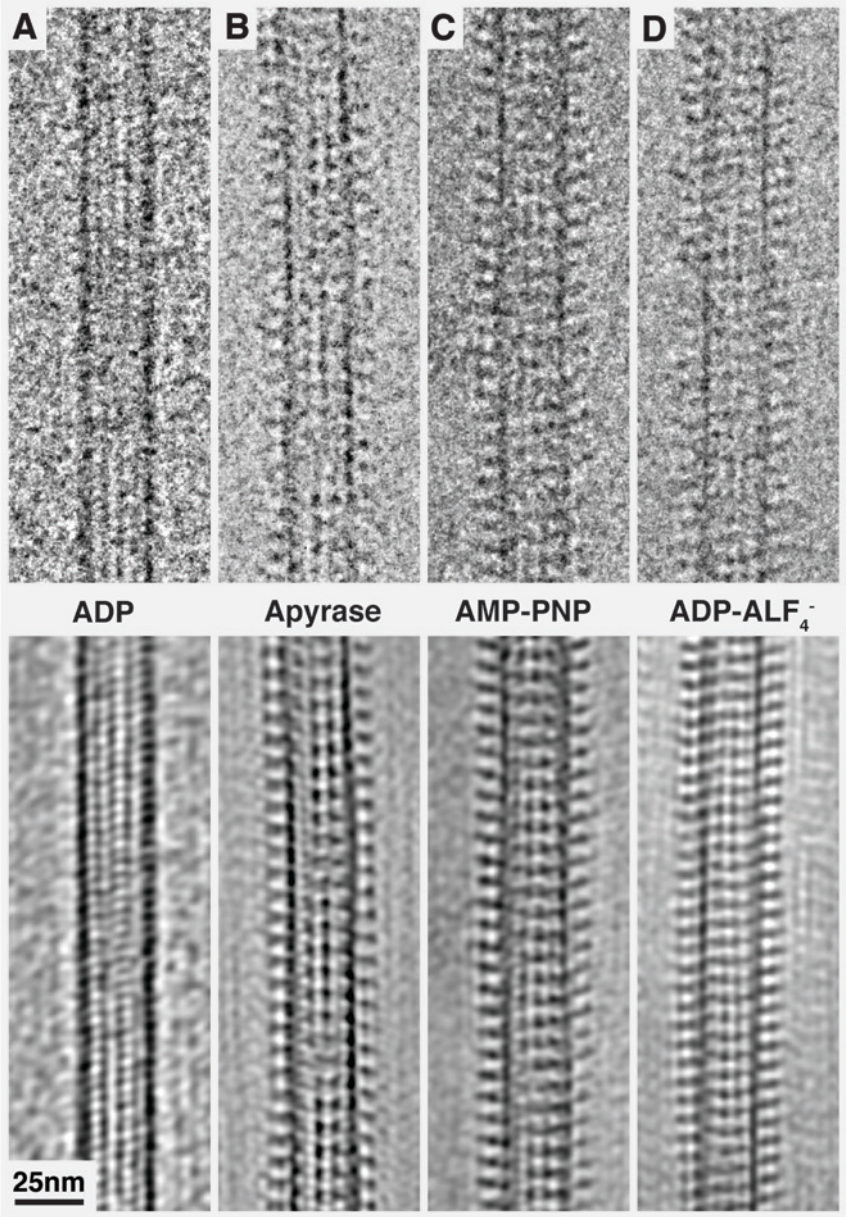

Figure 2-4: The MT binding configuration of Kar3Vik1 in different nucleotide states.
2D projections of Kar3Vik1-decorated MTs (top) and corresponding Fourier filtered images (bottom). **(A)** In the presence of Kar3Vik1-ADP, MTs appear predominantly undecorated. **(B)** In the nucleotide-free state, achieved by incubating Kar3Vik1 with apyrase, MTs appear completely decorated and clearly show Kar3Vik1 binding to the MT with only one of its globular domains, with the second domain detached and extending away from the MT. Similarly, Kar3Vik1-AMP-PNP, trapped in the ATP state **(C)**, and Kar3Vik1-ADP-AlF_4^-, mimicking the ADP+P_i state **(D)** bind to the MT in a one-head-down, one-head-up configuration. In these images, it is not possible to know whether it is Kar3 or Vik1 in contact with the MT but this is addressed in Chapter 3.

Kar3Vik1 shows cooperative binding along MTs

To determine whether Kar3Vik1 binds to MTs in a cooperative manner as reported previously (Allingham et al., 2007) and perhaps identify some basis for the cooperativity, WT GCN4-Kar3Vik1 was incubated with MTs at sub-stoichiometric conditions, with more motor binding sites available on MTs than motors. Cryo-EM images remarkably showed MTs that were completely decorated by WT GCN4-Kar3Vik1 while other MTs in close proximity remained undecorated by the motor (Figure 2-5A). Furthermore, MTs were seen to be partially decorated by WT GCN4-Kar3Vik1 in a manner that had some protofilaments fully decorated, while other protofilaments of the same MT remained completely free of motor decoration (Figure 2-5B). This binding pattern illustrates that Kar3Vik1 decorates the MT lattice in a highly cooperative fashion, with the cooperativity being in the axial direction along the length of the MT. The cooperative behavior was noted to be the strongest in the nucleotide-free state (Figure 2-5A and B), but was also seen in the presence of AMP-PNP (Figure 2-5C) and ADP-AlF_4^-. The MT partially decorated with WT GCN4-Kar3Vik1 in Figure 2-5C allows for an unobstructed view of the motor bound to the side wall of the MT. In this clear side-view, the asymmetric binding configuration of WT GCN4-Kar3Vik1 to the MT as described above can be easily visualized.

Discussion

This EM investigation has revealed that in the nucleotide-free, ATP, and ADP+P_i states, Kar3Vik1 binds asymmetrically to the MTs through only one of its globular domains, with the second globular domain detached and extending away from the MT. This binding configuration of Kar3Vik1 is highly reminiscent of that of homodimeric Ncd (Sosa et al., 1997a, Wendt et al., 2002), but differs from kinesin-1 and other dimeric kinesins that bind simultaneously with both

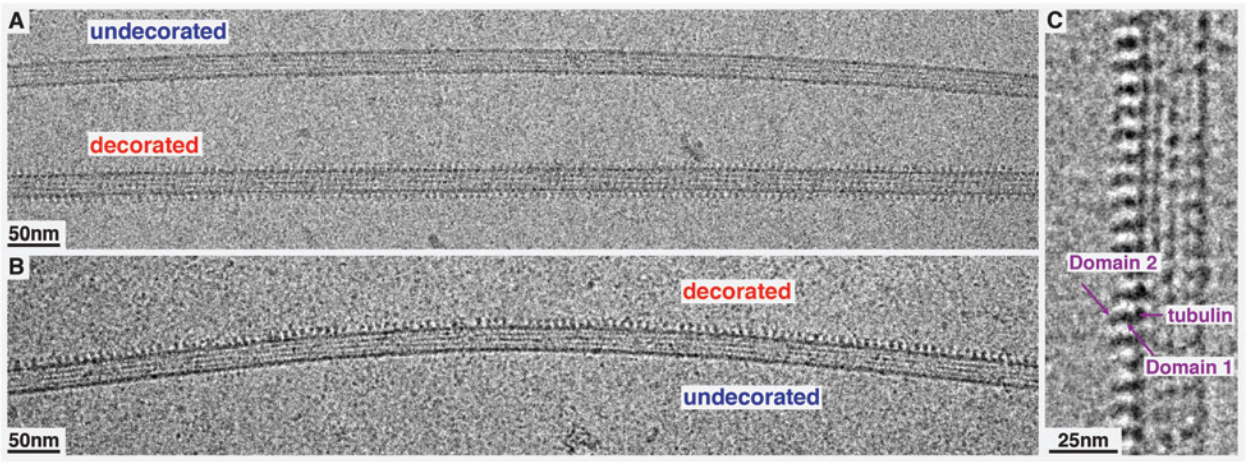

Figure 2-5: Kar3Vik1 binds cooperatively to MTs through only one of its globular domains. (A) Cooperative binding by Kar3Vik1 is demonstrated by one MT being completely decorated by Kar3Vik1, while an adjacent MT is completely free of motor decoration. **(B)** A single MT showing one protofilament that is fully decorated by Kar3Vik1 while other protofilaments remain undecorated, illustrating that the cooperativity occurs in the axial direction along the MT. **(C)** An optimal side-view of a MT partially decorated by Kar3Vik1 shows clearly that the heterodimer binds to the MT through only one of its globular domains, with the second domain extending outwards. Cooperative binding appears to be strongest in the nucleotide-free state (**A** and **B**), but is also seen in the AMP-PNP state (**C**).

globular domains to consecutive tubulin subunits along a single protofilament (Hoenger et al., 2000, Krzysiak et al., 2006).

The complete decoration of MTs seen by cryo-EM in the presence of AMP-PNP agrees well with equilibrium cosedimentation experiments of Kar3Vik1 where maximum MT binding was achieved at ~1:1 ratio of motors to binding sites on tubulin (Allingham et al., 2007). Conversely, cosedimentation experiments of Kar3Vik1 with a high concentration of ADP have shown maximum MT binding at a ~1:2 ratio of motors to binding sites on tubulin leading to the proposal that Vik1 is in contact with the MT in this nucleotide state, and the motor is bound in an orientation that prevents the binding of another motor at an adjacent binding site (Allingham et al., 2007). This disagrees with my EM data that instead reveal predominantly undecorated MTs in the presence of ADP.

In a related result, Allingham et al. (2007), have reported Vik1MHD binding to MTs by equilibrium cosedimentation. However, I have not been able to visualize Vik1MHD binding to MTs despite employing a variety of sample preparation methods and EM techniques. This inconsistency is difficult to explain, though it could be related to the fact that the timing of MT-binding in the cosedimentation experiments (30 min centrifugation after incubating Vik1MHD with MTs) differs substatially from those applied in cryo-EM (rapid plunge-freezing after incubating Vik1MHD with MTs). Perhaps the interaction between Vik1MHD and the MT is too transient to be detected by EM. It is also possible that the increase in salt concentration in the sample buffer due to evaporation immediately prior to plunge-freezing causes Vik1MHD to dissociate from the MT. These reasons still support a model where Vik1 does interact with the MT. However, it could also be that during centrifugation, the MTs behave like a net and non-

specifically pull Vik1 down. Indeed the strong negative charge of MTs means that under certain conditions proteins can bind to MTs in a way that is not biologically relevant. These arguments favor a model where Vik1 does not interact with the MT during its walking cycle, but still acts in an important way to influence Kar3's activity. Additional experiments aimed at clarifying Vik1's role in Kar3Vik1's motility cycle are reported in Chapter 3.

The strong cooperative MT-binding behavior displayed by Kar3Vik1, is starkly contrasted by that of the Kar3MD alone which binds stochastically to the MT lattice. Taken together, these results provide evidence that Vik1 modulates the MT-binding properties of Kar3. A similar cooperative binding pattern has been reported for Ncd (Wendt et al., 2002), but has not been seen for kinesin-1 or dimeric Eg5 (Sproul et al., 2005, Krzysiak et al., 2006). In 2D-projections of Kar3Vik1-decorated MTs, the individual motors do not appear to be touching each other. Thus, it is unlikely that the cooperativity arises from contacts between the dimers as has been reported for cooperative binding by the Ndc80 complex (Alushin et al., 2010). Rather, binding of Kar3Vik1 to the MT could cause adjustments in tubulin that make an adjacent kinesin binding site on the MT more accessible. *In vivo*, this cooperativity may allow Kar3Vik1 to recruit additional Kar3Vik1 dimers (or perhaps other MT-binding proteins) to the spindle poles during formation of the mitotic spindle. In Kar3Vik1's proposed role of focusing and stabilizing the spindle MTs by crosslinking, and because Kar3Vik1 lacks processivity, it could be beneficial to work in a coordinated manner with other Kar3Vik1 molecules.

Chapter 3. Visualization and structural analysis of Kar3Vik1's powerstroke by cryo-electron microscopy

A large portion of the material in this section will soon appear in:

Rank, KC., Chen, JC., **Cope, J.**, Porche, K., Hoenger, A., Gilbert, SP., Rayment., I *Submitted*

Cope, J., Rank, KC., Rayment, I., Hoenger, A. *Manuscript in preparation*

Introduction

The results described in Chapter 2 show Kar3Vik1 binding to MTs through only one globular domain, with the second globular domain extending away from the MT in all nucleotide states where complete decoration was obtained. While these binding configuration results are informative, they cannot provide insight into two major questions essential for understanding Kar3Vik1's mechanism of movement: 1) what structural changes occur within the heterodimer in response to changes in nucleotide state, and 2) which component of the heterodimer, Kar3 or Vik1, is in contact with the MT in each nucleotide state.

Here I have used cryo-EM and subsequent helical reconstruction to analyze the nucleotide-state dependent conformations of MT-bound WT GCN4-Kar3Vik1 in the presence of nucleotide-state analogs. To differentiate between Kar3 and Vik1 in my reconstructions, I have benefited from a 'cysteine-free' Kar3Vik1 construct. Kar3 and Vik1 each have five cysteine residues in their globular head domains (Figure 3-1A). The cysteine-free Kar3Vik1, developed in the lab of Ivan Rayment, has had all of these cysteines removed and replaced by alanine, valine or leucine. Cysteine-free Kar3Vik1 has been characterized in the lab of Susan Gilbert and shown to have activity similar to WT GCN4-Kar3Vik1 in MT motility assays, ATPase assays, and MT binding

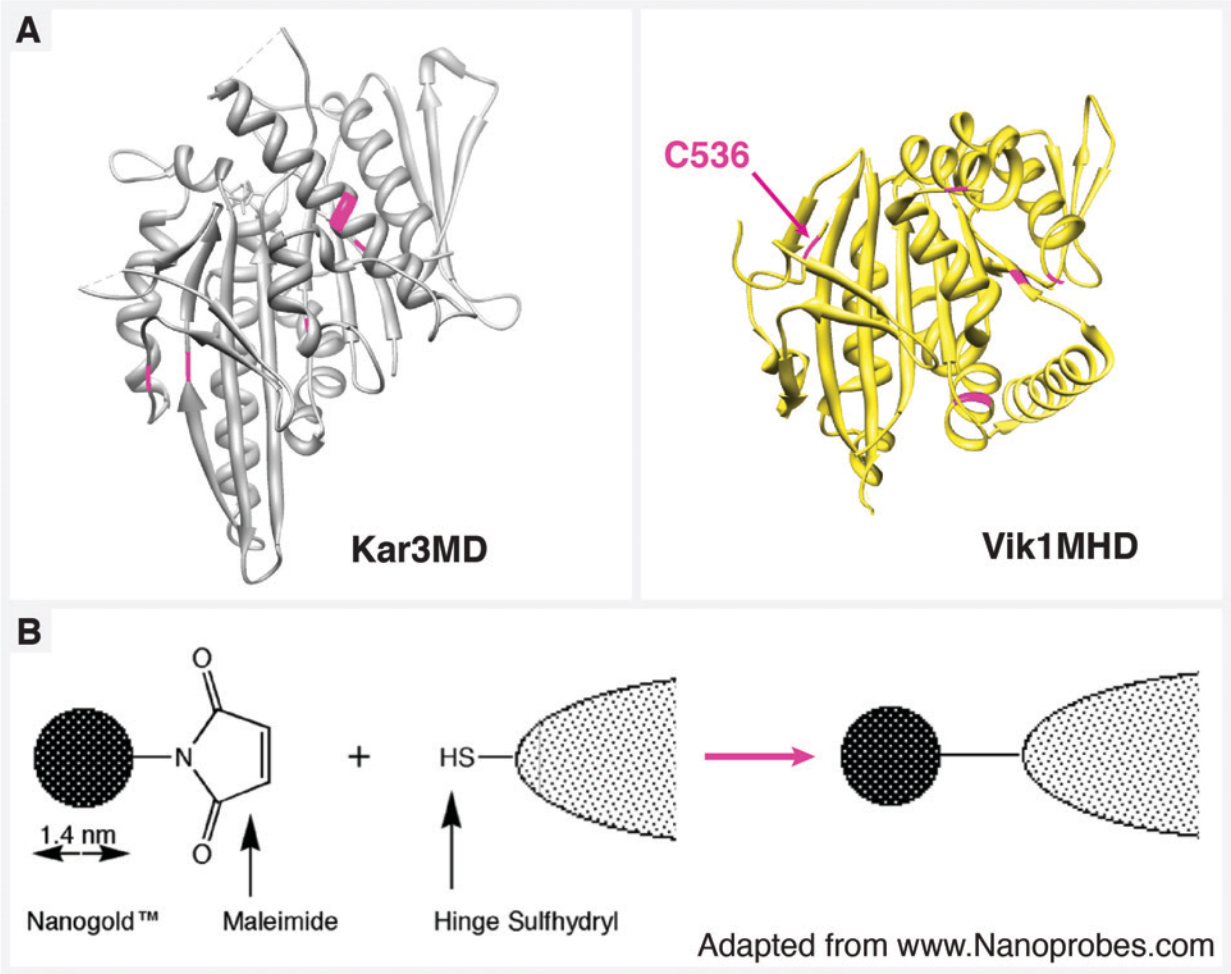

Figure 3-1: Nanogold®-labeling can be used to specifically label cysteine residues. (A) The C-terminal globular domains of Kar3 and Vik1 each have 5 cysteine residues highlighted in pink. In the 'cysteine free' Kar3Vik1 constructs, all of the cysteines have been replaced with alanine, valine or leucine. A 'cysteine-light' construct used in this chapter, has had one of the cysteines, C536, inserted back into its original position on Vik1 for labeling with Nanogold®. **(B)** A Nanogold® particle with a thiol-reactive maleimide was used to specifically label the sulfhydryl group on C536 to identify Vik1 in helical reconstructions.

affinity. For my work, I have used a 'cysteine-light' construct GCN4-Kar3$_{CL}$Vik1$_{C536C}$, generated from the cysteine-free mutant with only a single cysteine inserted back into its original position on Vik1 (Figure 3-1A). I labeled this cysteine specifically with a 1.4 nm Nanogold® particle through a maleimide-linker (Figure 3-1B) to identify Vik1 in Kar3Vik1-MT complexes.

The cysteine-free Kar3Vik1 construct is also an extremely useful tool for gaining insight into Kar3Vik1's mechanism of movement as cysteine residues can be inserted at desired positions for crosslinking by chemical linkers of various sizes. In this chapter, two crosslinked constructs have been used. GCN4-Kar3$_{E382C}$Vik1$_{K372C}$ has two cysteines engineered at the base of Kar3Vik1's coiled-coil stalk (Figure 3-12A). Crosslinking these residues prevents the coiled-coil from unwinding and allows us to test whether this is necessary for Kar3Vik1's motility. The second construct, SHD-Kar3Vik1$_{E355C-K423C}$, has a cysteine in Vik1's stalk coil and another cysteine in Vik1's globular domain (Figure 3-14A). Crosslinking these cysteines constrains rotation of Vik1 relative to the stalk and also prevents Vik1 from detaching from the stalk. Here I have used cryo-EM and helical reconstruction to gain structural insight into the effect of these crosslinks on Kar3Vik1's powerstroke.

Helical reconstruction as a tool to study motor-decorated MTs

The first 3D reconstruction from EM images was performed by DeRosier and Klug (1968), who determined the 3D structure of the T4 bacteriophage tail using helical reconstruction. The general principle of 3D reconstruction from 2D images is based on the central section theorem which states that the Fourier transform of a 2D projection of a 3D structure (such as an EM image) is identical to the central section of the 3D transform of the object. The 3D transform of a structure can thus be determined by collecting 2D projections of the structure at various angles

that each correspond to a different central section of the structure's 3D transform. When a structure possesses helical symmetry, it is particularly fortunate because the repeating unit in the helical lattice is present at all of the angles needed to obtain a complete 3D transform, from which the 3D structure can be obtained with isotropic resolution (DeRosier and Moore, 1970; Hoenger and Gross, 2008).

A small subset of MTs prepared *in vitro*, namely those composed of 10, 11, 15 or 16 protofilaments, form perfect helices. Other MTs possess a lattice seam that breaks the helical symmetry as described in Chapter 1 (Chretien and Wade 1991; Kikkawa et al., 1994; Sosa et al., 1997b). For the work in this chapter, helical reconstruction was performed using a Fourier-Bessel method exclusively on 15-protofilament MTs which is a well-established technique for obtaining 3D structural information of kinesin-MT complexes (Arnal et al., 1996; Sosa et al., 1997a; Hoenger et al., 2000; Endres et al., 2006 are a few of many).

A MT decorated with Kar3Vik1 (or other kinesin motor domain) can be described as a superposition of a number of helices that each have different helical pitches. For example, the 15 protofilaments of the MT form 15 parallel helices with a very long pitch (the microtubule supertwist), while the αβ-tubulin subunits each decorated with a single motor can be followed by two parallel helices with a much shorter pitch (Figures 3-5 and 3-6). The Fourier transform of a motor-decorated 15-protofilament MT thus produces layer lines that each correspond to a distinct helical feature on the MT (Figures 3-5 and 3-6) (Beuron and Hoenger, 2001; Hoenger and Gross, 2008). Based on the central section theorem described above, to obtain a complete 3D transform of one αβ-tubulin dimer decorated with a single motor, it has to be projected at small angular increments from 0°-180°. Because of the helical rotation of a 15-protofilament microtubule, there is usually sufficient information in a single image to obtain two complete 3D

reconstructions from one single tube. However, in practice, the signal-to-noise ratio in a single cryo-electron micrograph is much too low to obtain useful structural detail and many datasets have to be aligned and averaged together to achieve reliable information to 20-30Å resolution.

Helical reconstructions of WT GCN4-Kar3Vik1 in different nucleotide states, and structural analyses of Nanogold®-labeled and crosslinked Kar3Vik1 constructs are presented in this chapter. The findings provide insight into the mechanism responsible for Kar3Vik1's minus-end directed movement. This is the first time that the powerstroke has been directly visualized for a heterodimeric kinesin.

Materials and Methods

Expression and purification of WT GCN4-Kar3Vik1 and other Kar3Vik1 constructs

The design, cloning, expression and purification of WT GCN4-Kar3Vik1, GCN4-$Kar3_{CL}Vik1_{C536C}$, GCN4-$Kar3_{E382C}Vik1_{K372C}$ and SHD-$Kar3Vik1_{E355C\text{-}K423C}$ was carried out in the lab of Ivan Rayment. All constructs contain the complete C-terminal globular domains of Kar3 and Vik1 as well as two and a half heptads of the native coiled-coil. To initialize dimerization, the native coiled-coil sequence is preceded by the GCN4 leucine zipper sequence or a synthetic homodimer (SHD) sequence (Rank et al., submitted).

Following purification GCN4-$Kar3_{E382C}Vik1_{K372C}$ was crosslinked with 1,4-butanediyl bismethanethiosulfonate (M4M) to create a 10 Å linker at the base of the coiled-coil stalk. Similarly, after purification, SHD-$Kar3Vik1_{E355C\text{-}K423C}$ was crosslinked with N, N'-ethylene-bis(iodoacetamide) (EBI) to create a 12 Å linker attaching the globular domain of Vik1 to Vik1's stalk. In both cases, 99% of the motor population is estimated to be crosslinked. Details on construct design, purification and chemical crosslinking are described in Rank et al. (submitted).

Maleimide-Nanogold® labeling of GCN4-Kar3$_{CL}$Vik1$_{C536C}$

Maleimide-Nanogold® (Nanoprobes, Yaphank, NY) was purchased as a powder lyophilized from 20 mM sodium phosphate, pH 6.5 and 150 mM NaCl. Immediately before use, 200 µl Milli-Q deionized water was added to the Maleimide-Nanogold® powder and the mixture was vortexed gently to resuspend all of the powder. The resuspension contained 6 nmol of Maleimide-Nanogold®. 42 µl (3 nmol) of GCN4-Kar3$_{CL}$Vik1$_{C536C}$ was added to the resuspended Maleimide-Nanogold® and incubated for 8-10 hours at 4˚C.

Separation of unbound Nanogold® from labeled/unlabeled GCN4-Kar3$_{CL}$Vik1$_{C536C}$

To increase labeling efficiency, Maleimide-Nanogold® was added in 2 fold excess to the number of protein molecules to be labeled. To reduce background, GCN4-Kar3$_{CL}$Vik1$_{C536C}$-Nanogold® was run through a Sephadex-G75 column to separate the labeled (and unlabeled) motors from unbound Nanogold®. 9 ml of PME buffer (10 mM PIPES pH 6.9, 5 mM $MgCl_2$, 1 mM EGTA) with 100 mM KCl was added to 0.4 mg of dry Sephadex-G75 Superfine resin (GE Healthcare, Uppsala, Sweden). The resin was left to swell for 3 hours at 90˚C. After swelling, the Sephadex-G75 matrix was poured into a narrow glass column. The column was packed by gravity flow and washed with PME buffer with 100 mM KCl, 0.2 mM ATP, 0.2 mM TCEP and stored overnight at 4˚C. After equilibration at 4˚C, the column was washed with an additional 15 ml of PME buffer with 100 mM KCl, 0.2 mM ATP, 0.2 mM TCEP. GCN4-Kar3$_{CL}$Vik1$_{C536C}$-Nanogold® was applied to the column and immediately 16 fractions of ~150 µl each were collected. The fractionation range of Sephadex G-75 Superfine resin for globular proteins is 3000 - 70 000 Da. With a molecular weight of > 85 660 Da, Nanogold®-labeled and unlabeled GCN4-Kar3$_{CL}$Vik1$_{C536C}$ eluted in the void volume (fractions 6-9), while unbound Nanogold® with a

molecular weight of 15 000 Da, interacted with the matrix and eluted later (fractions 11-14) (Figure 3-2A). Nanogold®-labeled GCN4-Kar3$_{CL}$Vik1$_{C536C}$ was used immediately for plunge-freezing with MTs for cryo-EM or flash-frozen in liquid nitrogen for storage at -80˚C.

Estimation of GCN4-Kar3$_{CL}$Vik1$_{C536C}$ labeling by Maleimide-Nanogold® using UV/visible spectrophotometry and SDS-PAGE

UV/visible spectrophotometry

The manufacturer's recommended method for estimating the efficiency of Nanogold®-labeling is spectrophotometry. The total concentration of Nanogold® in the mixture can be calculated by measuring the absorbance at a wavelength of 420 nm (A_{420}). The total protein concentration can be calculated by measuring the absorbance at 280 nm (A_{280}) and correcting the value for absorbance at 280 nm due to the Nanogold®. The efficiency of labeling can then be determined by calculating the ratio of (total Nanogold® concentration)/(total protein concentration). After running GCN4-Kar3$_{CL}$Vik1$_{C536C}$-Nanogold® through the Sephadex-G75 column, the A_{420} and A_{280} of each of the fractions collected was measured. However, the extinction coefficient of GCN4-Kar3$_{CL}$Vik1$_{C536C}$, 43 780, is extremely low and because Nanogold® has a very high absorbance peak at 280 nm, the A_{280} due to the motor was not detectable. Thus, this method was unsuccessful for determining the amount of Nanogold® labeling of GCN4-Kar3$_{CL}$Vik1$_{C536C}$.

SDS-PAGE

To determine which fractions contained Nanogold®-labeled GCN4-Kar3$_{CL}$Vik1$_{C536C}$, fractions eluted from the Sephadex-G75 column were prepared for SDS-PAGE by mixing 15 µl of each fraction with 10 µl 1 M DTT, 25 µl NuPAGE® LDS Sample Buffer (Invitrogen, Carlsbad, CA)

and 60 µl Milli-Q water. Samples were boiled at 100 ˚C for 5 min. As a control, GCN4-Kar3$_{CL}$Vik1$_{C536C}$ without Nanogold® was prepared for SDS-PAGE in the same way. 30 µl of each sample was loaded onto a NuPAGE® 4-12% Bis-Tris Gel (Invitrogen, Carlsbad, CA) alongside a Dual Color Precision Plus Protein Standard (Bio-Rad, Hercules, CA). Samples were run through the gel at 100 V for 6 hours to obtain maximum separation. Gels were rinsed in distilled water for 1 hour and subsequently stained with SimplyBlue SafeStain (Invitrogen, Carlsbad, CA), then destained overnight with distilled water. Fractions 7 and 8 showed the highest amount of protein present (Figure 3-2A).

To determine approximately how much GCN4-Kar3$_{CL}$Vik1$_{C536C}$ had been labeled with Nanogold®, the ratio of Nanogold®-labeled to unlabeled GCN4-Kar3$_{CL}$Vik1$_{C536C}$ was determined using the Gel Analyzer Tool in ImageJ (National Institutes of Health, Bethesda, MD). The bands of Nanogold®-labeled and unlabeled Vik1$_{C536C}$ were selected and their relative intensities were plotted (Figure 3-2B). The area underneath each of the two resulting peaks was then measured. A comparison of the areas under the peaks showed the relative percentage of labeled and unlabeled Vik1$_{C536C}$. The percent labeling was typically determined to be 60-80%.

Vitrification of Kar3Vik1-MT complexes for cryo-EM

WT GCN4-Kar3Vik1, unlabeled GCN4-Kar3$_{CL}$Vik1$_{C536C}$, Nanogold®-labeled GCN4-Kar3$_{CL}$Vik1$_{C536C}$, SHD-Kar3Vik1$_{E355C-K423C}$-EBI, and GCN4-Kar3$_{E382C}$Vik1$_{K372C}$-M4M were complexed to MTs in the presence of apyrase, AMP-PNP, or ADP-AlF_4^-, and plunge-frozen into liquid ethane in preparation for cryo-EM as described for WT GCN4-Kar3Vik1 in Chapter 2.

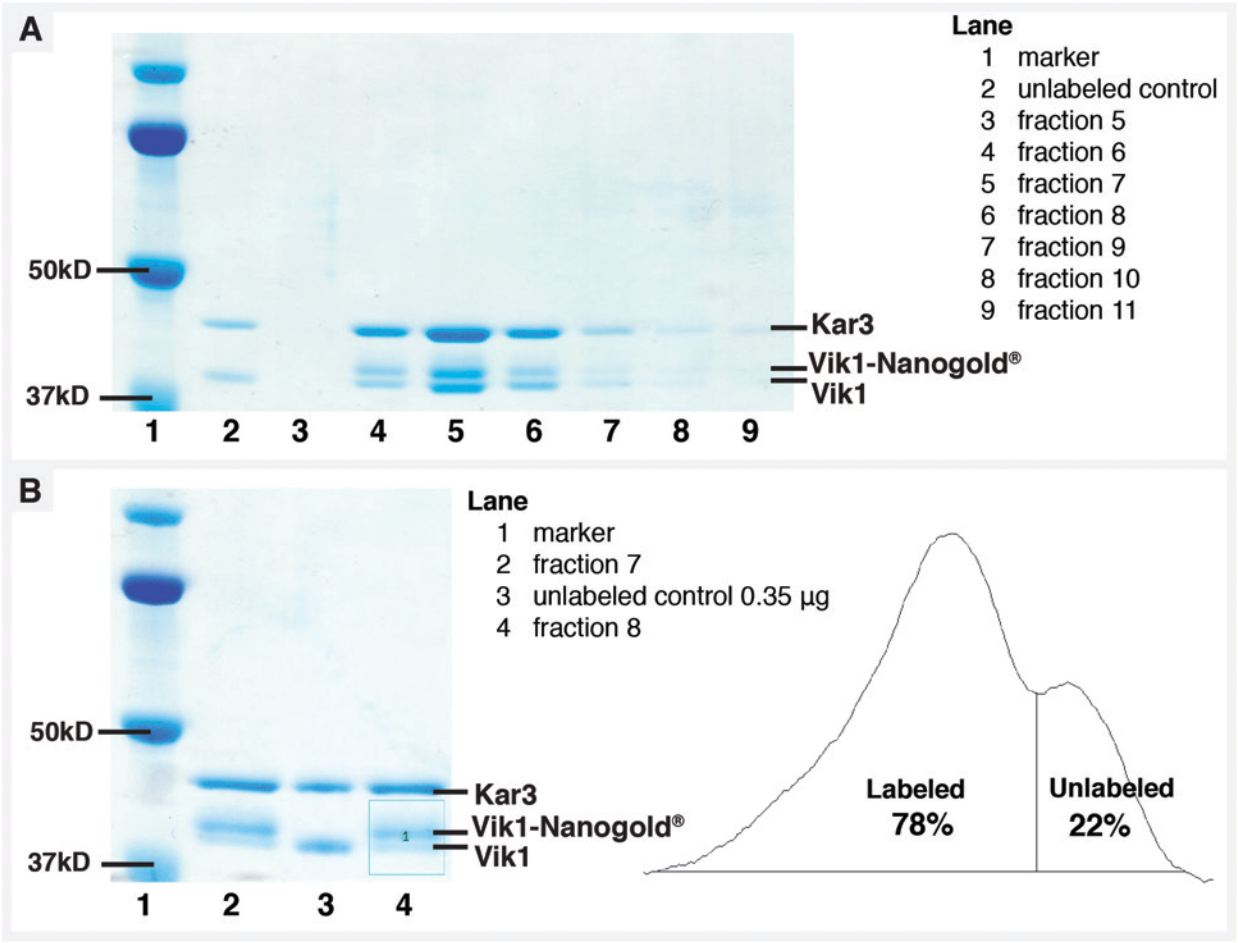

Figure 3-2: Quantification of Nanogold®-labeling efficiency. (A) Labeled and unlabeled GCN4-Kar3$_{CL}$Vik1$_{C536C}$ was separated from unbound Nanogold using gel filtration and elutions from the size-exclusion column were separated by SDS-PAGE. The majority of the protein eluted in fraction 7. Unbound Nanogold® eluted in fractions 11-14 which is not visible on the gel but can be seen by the brown color of the solution (not shown). **(B)** The percentage of Nanogold®-labeled Vik1$_{C536C}$ was determined using the Gel Analyzer Tool in ImageJ. The relative intensity of the labeled and unlabeled Vik1$_{C536C}$ bands (turquoise box) was plotted and the area under the peaks was measured to quantify the percent labeling of Vik1$_{C56C}$. Typically labeling efficiencies of 60-80% were achieved.

Cryo-EM data collection for helical reconstruction

2D projections of vitrified Kar3Vik1-MT complexes were acquired on an FEI Tecnai F20 FEG transmission EM (FEI-Company, Eindhoven, The Netherlands) operating at 200 kV at a nominal magnification of 29 000 x and a defocus of -2.5 μm, with an electron dose of 15 electrons/$Å^2$. The exposure time was set to 0.35 s to minimize drift while imaging. Images were recorded without binning on a 4K x 4K Gatan Ultrascan 895 CCD camera (Gatan, Inc, Pleasanton, CA) with the resulting pixel size corresponding to 3.8 Å on the specimen.

Helical reconstruction of Kar3MD-MT and Kar3Vik1-MT complexes

Selection of 15-protofilament MTs

Cryo-EM images were opened in IMOD (Kremer et al. 1996) and inspected visually for completely decorated MTs with 15 protofilaments. 15-protofilament MTs were identified by their characteristic moiré pattern resulting from the superposition of protofilaments on the top and bottom of the MT in projection (Figure 3-3) (Chrétien and Wade, 1991). Once identified, 15-protofilament MTs were extracted from the images at full resolution using 'trimvol' in IMOD. The IMOD program 'newstack' was used to rotate the extracted images to orient the MT with its length along the *X*-axis (horizontally). The rotated images were converted to SUPRIM format for input into the helical processing software. Subsequent steps were carried out using the helical averaging software package PHOELIX (Whittaker et al., 1995, Carragher et al., 1996), based on the SUPRIM (Schroeter and Bretaudiere, 1996) and MRC (Crowther et al., 1996) image processing packages.

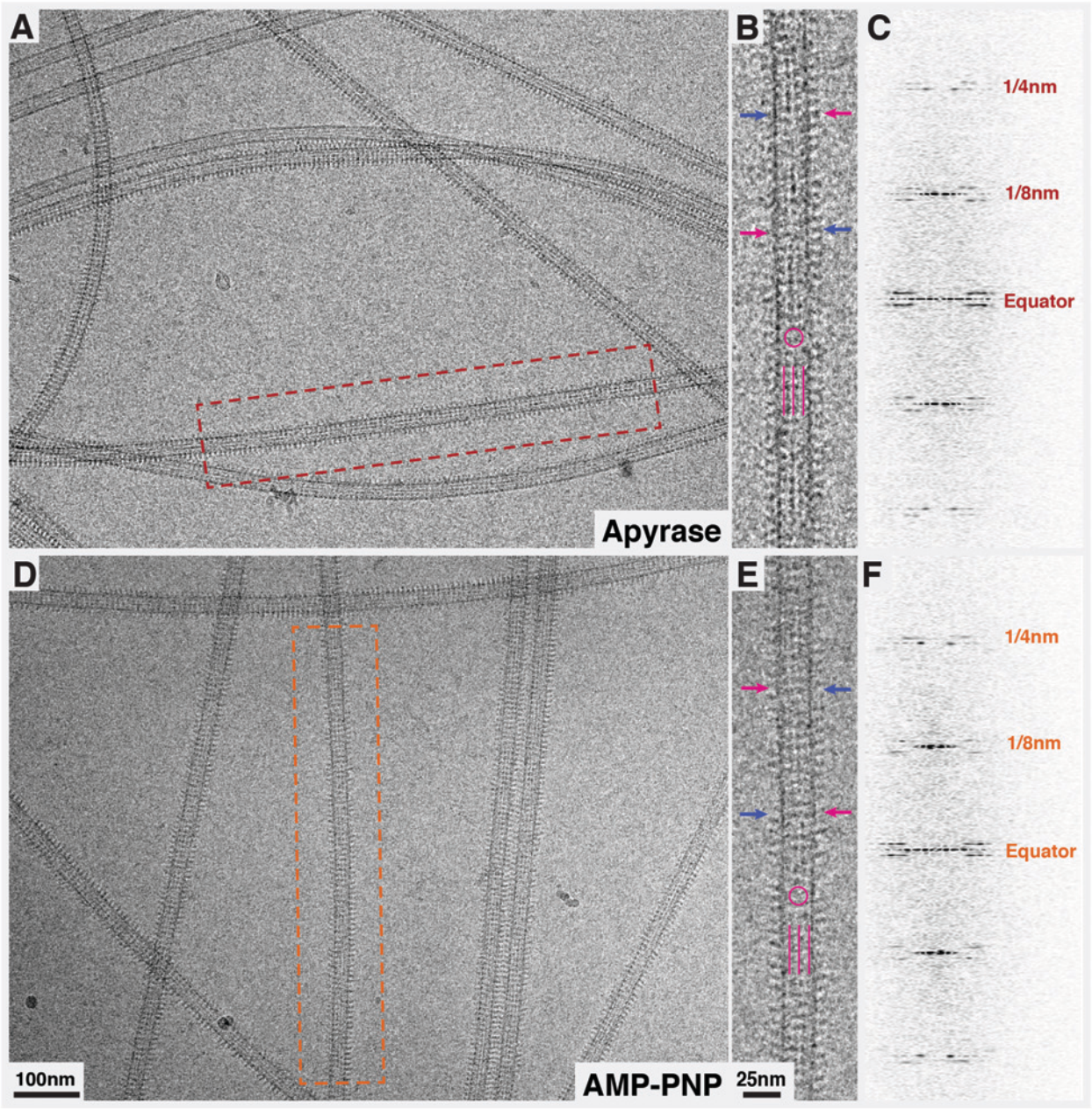

Figure 3-3: Identification of 15-protofilament MTs for helical processing. Cryo-electron micrograph of MTs decorated with WT GCN4-Kar3Vik1 in the nucleotide-free **(A-C)** and AMP-PNP **(D-F)** states. The MTs boxed in red **(A)** and orange **(D)** are magnified in **B** and **E** respectively alongside their corresponding Fourier transforms **(C & F)**. These MTs are identified as each having 15 protofilaments by examining their moiré patterns produced from the superposition of protofilaments in projection. The alternation of three stripes (pink lines) and blurry areas (pink circles) along the length of the MT, and the alternation of thick (pink arrows) and thin (blue arrows) walls is characteristic of 15-protofilament MTs as they indicate the length of the MTs supertwist. The layer lines at 1/4 nm in the power spectra show that these MTs have a right-handed supertwist and thus form perfect helices that can be used for helical reconstruction.

Extraction of layer line information from 15-protofilament MTs

MTs (from SUPRIM images described above) were isolated from the surrounding background in the image by placing points along the axis of the MT and boxing out a region around the MT to be averaged. The MT was then straightened computationally using PHOELIX as described (Whittaker et al. 1995). Following straightening, large-scale background variation was subtracted from the image to account for changes in ice thickness that may occur across the length of the MT.

Helical averaging of 15-protofilament MTs

Layer-line data from a large number of MTs were shifted to a common phase origin according to a reference image and subsequently averaged. Three rounds of averaging were carried out and the reference was iteratively improved with each new average. Helical averaging was always completed with more than one reference to ensure that final averages were not biased by the reference used. Only datasets with a phase residual of less than 20 degrees relative to the reference were included in the final reconstruction. All datasets were truncated to a maximum resolution of 15 Å. The final helical averaging of the different constructs in each nucleotide state was carried out with the identical reference (a MT decorated with Kar3Vik1 in the AMP-PNP state). This shifted the layer line data to the identical phase origin so all helical reconstructions would be directly comparable to each other. The number of individual datasets included in each of the helical reconstructions presented in this chapter is shown in Table 3-1. 3D electron density maps of the averages were visualized in IMOD. Surface rendering of the maps was carried out in UCSF Chimera (Pettersen et al., 2004).

Kar3Vik1 construct	No. of datasets	Approx. No. of asymmetric units
Kar3MD – AMP-PNP	46	28 000
GCN4-Kar3Vik1 – Nucleotide-free	52	42 000
GCN4-Kar3Vik1 – AMP-PNP	67	27 000
GCN4-Kar3Vik1 – ADP-AlF_4^-	14	6000
GCN4-$Kar3_{CL}Vik1_{C536C}$ – Nucleotide-free	59	37 500
GCN4-$Kar3_{CL}Vik1_{C536C}$ – AMP-PNP	37	36 000
Nanogold®-GCN4-$Kar3_{CL}Vik1_{C536C}$ – Nucleotide-free	46	22 000
Nanogold®-GCN4-$Kar3_{CL}Vik1_{C536C}$ – AMP-PNP	33	15 000
GCN4-$Kar3_{E382C}Vik1_{K372C}$-M4M – Nucleotide-free	45	24 000
GCN4-$Kar3_{E382C}Vik1_{K372C}$-M4M – AMP-PNP	41	24 000
SHD-$Kar3Vik1_{E355C\text{-}K423C}$-EBI – Nucleotide-free	54	30 000
SHD-$Kar3Vik1_{E355C\text{-}K423C}$-EBI – AMP-PNP	87	32 000

Table 3-1: Number of datasets and approximate number of asymmetric units included in helical reconstructions of Kar3MD and Kar3Vik1 constructs. The approximate number of asymmetric units averaged in the final reconstruction was determined by measuring the length of each MT included in the average, divided by 8 (the length of one αβ-tubulin repeat), multiplied by 15 (the number of protofilaments in each MT).

Difference mapping to show statistically significant differences in helical averages

The standard deviation within datasets used for each helical reconstruction was determined by generating individual reconstructions from each of the datasets that were included in the final reconstruction. All individual reconstructions were shifted to the same phase origin and their

density was normalized so they could be compared to each other voxel by voxel. The standard deviation of the voxel densities at each corresponding position in all of the individual reconstructions was determined using 'clip' in IMOD. To calculate statistically significant differences between averages of Kar3Vik1 complexed to MTs in different nucleotide states (or Nanogold®-labeled and unlabeled Kar3Vik1) the final helical average from one state was subtracted from the final average of a second state. The statistical significance of the difference at each voxel was determined using the standard deviations showing the internal differences for each of the two states generated as described above. The significance level was set to 0.001 so that only differences with a 99.9% probability of being true differences, as determined by a one-tailed t-test, were shown in the difference maps (see Milligan and Flicker, 1987). Differences were deemed 'significant' with a level of 0.001 based on a t-statistic determined from the degrees of freedom in the data. The degrees of freedom were calculated by summing the number of datasets in the two reconstructions being compared, then subtracting two.

Docking of crystal structures into electron density maps

The crystal structure of the αβ-tubulin dimer (PDB accession: 1JFF) (Lowe et al., 2001) was docked manually into the electron density maps using UCSF Chimera. The SHD-Kar3Vik1$_{E355C-K423C}$ -EBI X-ray crystal structure (Rank et al., submitted) was docked into the maps manually using Chimera by positioning Kar3 onto the MT based on the results of Hirose et al. (2006). To reinforce this manual docking, the SHD-Kar3Vik1$_{E355C-K423C}$ -EBI crystal structure was docked quantitatively into the map of the nucleotide-free state using the FFT-Accelerated 6D Exhaustive Search tool in Situs (Chacón and Wriggers, 2002). This program was used to perform a rigid-body, exhaustive search around translational and rotational space to obtain the best global fit of

Kar3Vik1 into the electron density map. The fit that gave the highest correlation score from this quantitative docking was in very close agreement with our initial manual docking result.

To dock SHD-Kar3Vik1$_{E355C-K423C}$ -EBI into the AMP-PNP state maps, the crystal structure was divided into two rigid-body components that could be manipulated separately: 1) the Kar3 motor domain core (residues Gly^{385}-Lys^{729}), and 2) the complete Vik1 domain with the coiled-coiled stalk. Each component was docked interactively by eye into the maps to obtain the best fit.

Results

In the nucleotide-free state, Kar3Vik1's coiled-coil points toward the MT plus end

WT GCN4-Kar3Vik1-MT complexes in the nucleotide-free state were analyzed by helical reconstruction to determine the MT-bound conformation of Kar3Vik1 that occurs when Kar3 releases nucleotide. The 3D map from helical averaging of Kar3Vik1 bound to MTs in the nucleotide-free state shows the two globular domains of Kar3 and Vik1 stacked on the MT with only one domain interacting with tubulin (Figure 3-4A). A strong density extending from between the two globular domains corresponding to Kar3Vik1's coiled-coil neck and stalk, can be seen. In the nucleotide-free state, the stalk points toward the plus end of the MT at an angle of approximately 25° from the MT's longitudinal axis (Figure 3-4). The amplitude and phase plots of the final average as well as phase plots of individual datasets included in the final reconstruction are shown in Figure 3-5 to illustrate data quality and reliability.

Binding of ATP to Kar3 causes a rotation of Kar3Vik1's stalk toward the MT minus end

The helical reconstruction electron density map of WT GCN4-Kar3Vik1-AMP-PNP bound to MTs looks strikingly different from that of Kar3Vik1 bound in the nucleotide-free state

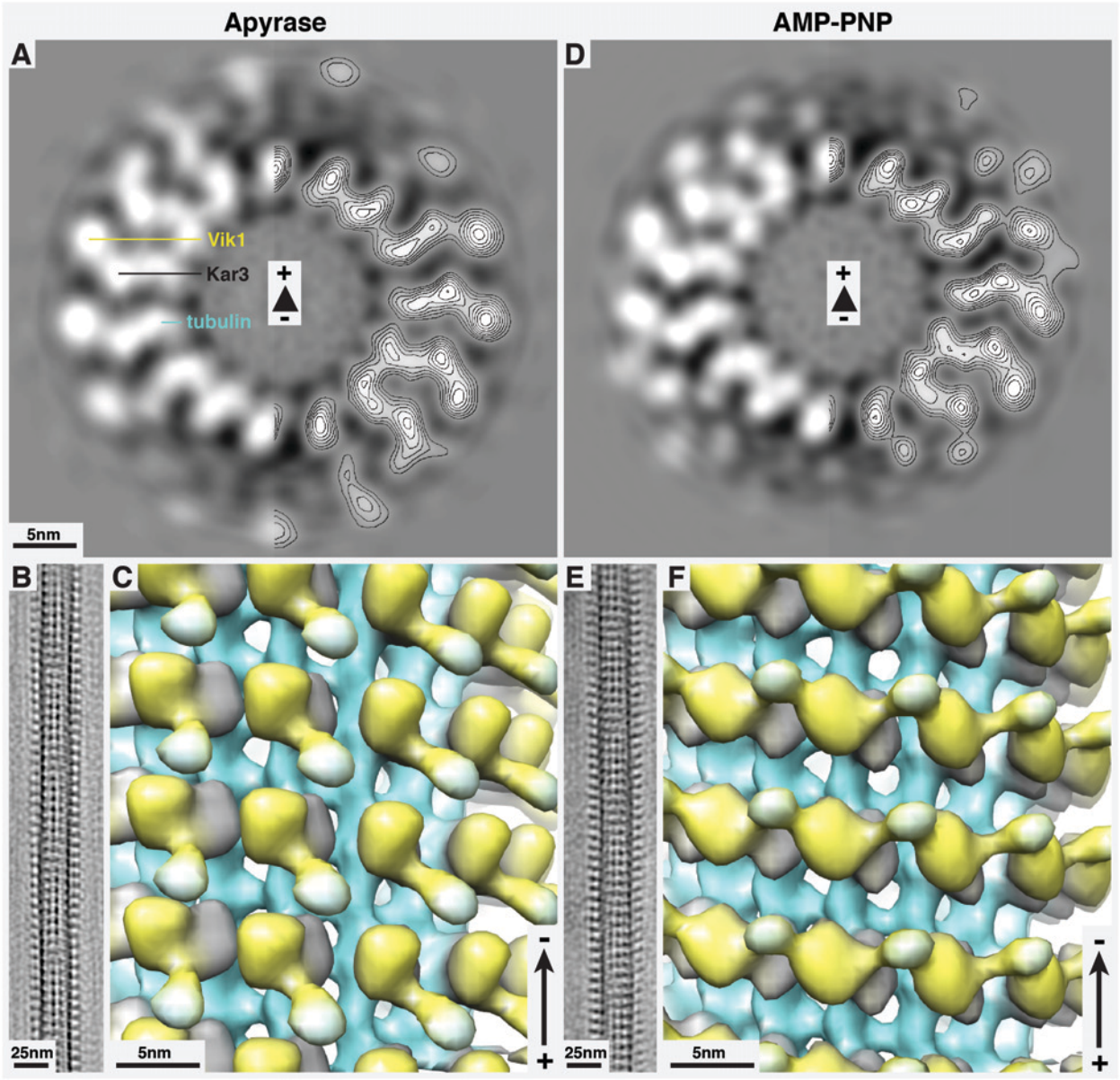

Figure 3-4: Cryo-EM and helical reconstruction reveals a crucial part of the Kar3Vik1 powerstroke. Helical reconstructions of Kar3Vik1-decorated MTs in the nucleotide-free **(A-C)** and AMP-PNP **(D-F)** states. **A** and **D** show 3.8 Å cross-sectional views through the 3D helical averages with the MT plus end pointing away from the reader. **B** and **E** are representative MTs that have been Fourier filtered to show the complete decoration of the MTs by Kar3Vik1 and display moiré patterns characteristic of 15-protofilament MTs. Surface rendering of the helical reconstruction of Kar3Vik1 complexed to MTs in the nucleotide-free state is shown in **C**, where Kar3Vik1's coiled-coil stalk can be seen pointing toward the MT plus end. The surface rendering of the reconstruction of Kar3Vik1 bound to MTs in the AMP-PNP state **(F)**, reveals a large conformational change in the outer domain that rotates the coiled-coil stalk ~90° to position it toward the MT minus-end. This stalk rotation is likely to have a crucial role in facilitating Kar3Vik1's retrograde motility.
Color key: tubulin - turquoise, Kar3 - gray, Vik1 - yellow, GCN4 coiled-coil - pale blue

(Figure 3-4). The density corresponding to the coiled-coil stalk can once again be visualized, but here it points toward the minus end of the MT (Figure 3-4F). The stalk appears to undergo a rotation of approximately 90° upon uptake of ATP. In addition to the rotation of the stalk, the outer domain also undergoes a significant rotation. Despite the conformational changes that occur in the stalk and outer domain, the domain in contact with the MT appears to remain unchanged from its nucleotide-free state position. The amplitude and phase plots of the AMP-PNP-state helical average as well as phase plots of individual datasets included in the final reconstruction are shown in Figure 3-6.

The ADP+P_i transition state strongly resembles the ATP state

The MT binding conformation of Kar3Vik1 following ATP hydrolysis was analyzed by helical reconstruction of WT GCN4-Kar3Vik1 bound to MTs in the presence of ADP-AlF_4^-. WT GCN4-Kar3Vik1 ADP-AlF_4^- bound to MTs strongly resembled that of the Kar3Vik1-AMP-PNP MT-bound state. (Figure 3-7). The resemblance of the maps of the AMP-PNP and ADP-AlF_4^- binding states suggests that Kar3Vik1 does not use the hydrolysis of ATP to 'reset' the position of its stalk. Rather, ATP hydrolysis converts the motor to a weak MT-binding state and the stalk returns to its original position after Kar3Vik1 detaches from the MT.

Kar3 is the domain in contact with the MT in the nucleotide-free and ATP states

Nanogold®-labeling was carried out to determine which globular domain of the heterodimer (either Kar3 or Vik1) is in contact with the MT to facilitate the coiled-coil stalk rotation. A single-cysteine Kar3Vik1 construct, GCN4-$Kar3_{CL}Vik1_{C536C}$ was engineered that could be labeled specifically with a maleimide-Nanogold® tag at residue 536 on Vik1. Helical

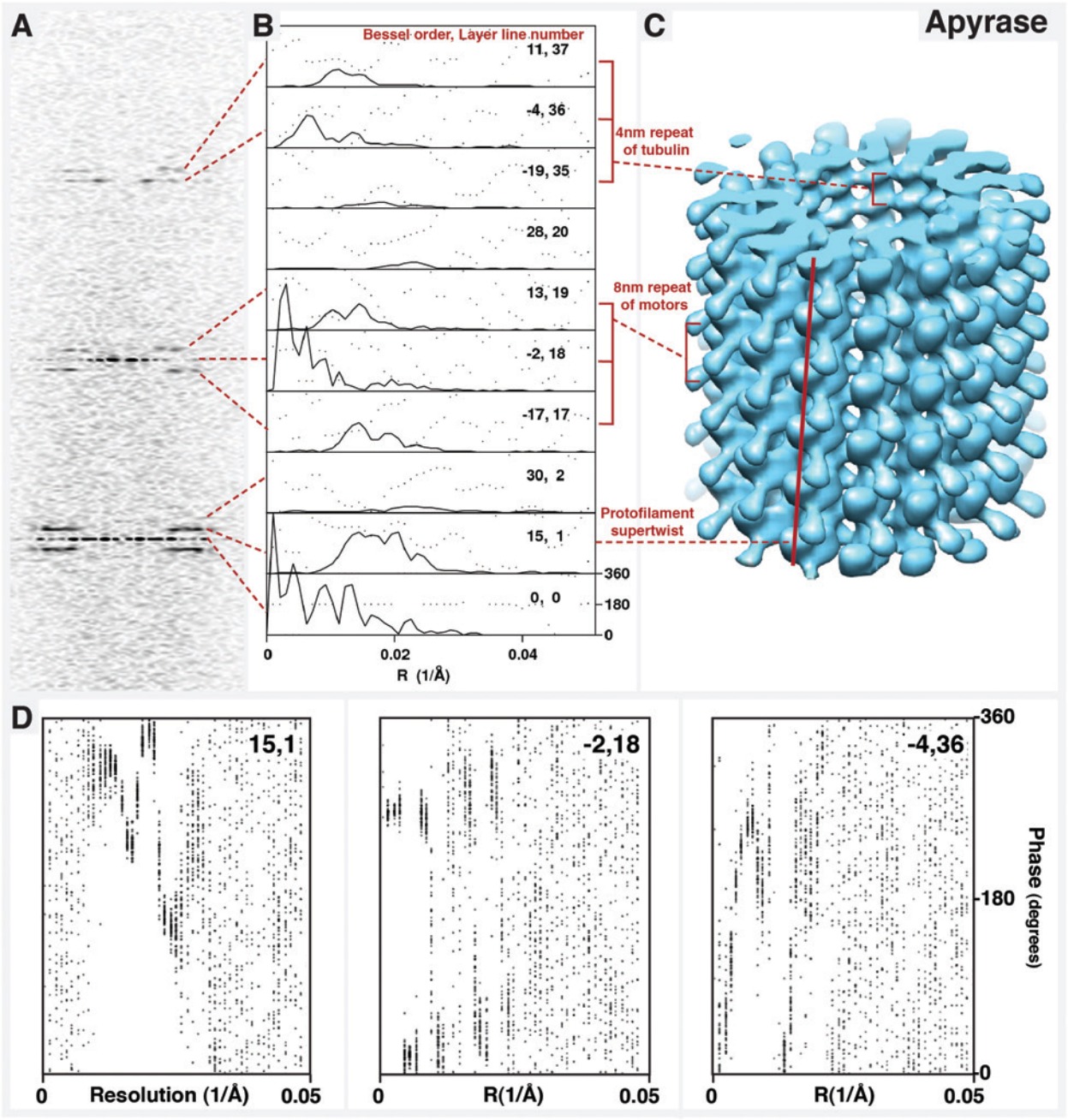

Figure 3-5: Quality of data included in the Kar3Vik1 nucleotide-free state helical average. **(A)** Fourier transform of a Kar3Vik1-decorated MT in the nucleotide-free state showing layer lines each corresponding to a different helical feature in the real-space reconstruction **(C)**. **(B)** The phases (dotted lines) and amplitudes (solid lines) of each of the layer lines of the final average are plotted. The amplitudes indicate the contribution of each layer line to the average. Relatively little scattering in the phase plots shows that the average is composed of good quality data. **(D)** Phase plots for three layer lines of all the individual datasets included in the final reconstruction (each dot is one phase value). The clustering of datasets at certain phases reflects reliable data while the unclustered phases are considered noise. Thus, the resolution limit of the 3D map can be determined from these plots to be ~25 Å. (See Beuron and Hoenger, 2001).

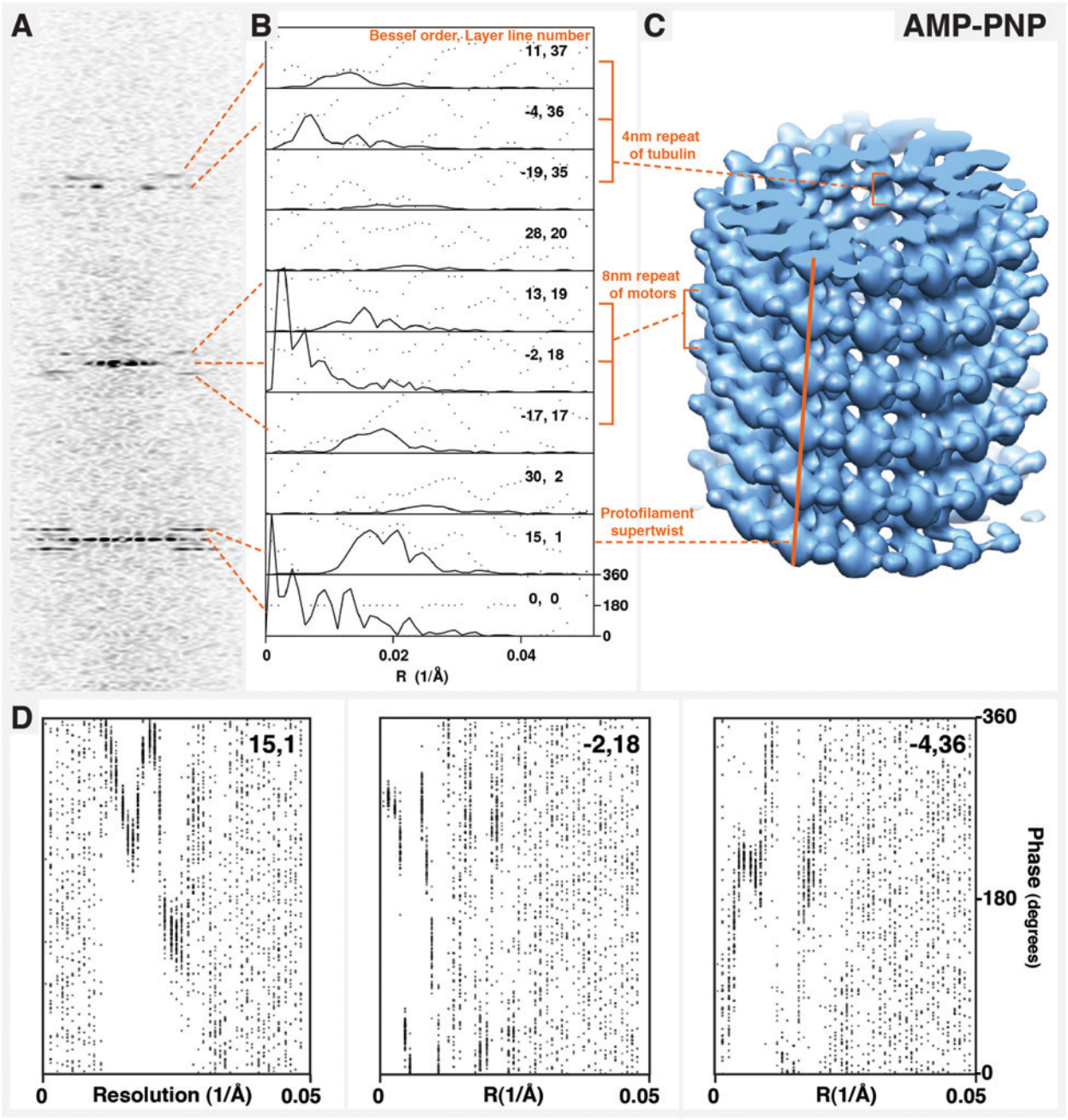

Figure 3-6: Quality of data included in the Kar3Vik1 AMP-PNP state helical average. **(A)** Fourier transform of a Kar3Vik1-decorated MT in the AMP-PNP state. **(B)** The phase (dotted lines) and amplitude (solid lines) plots of the layer lines obtained from the average in **(C)** shows incorporation of high quality data as described for Figure 3-5. **(D)** Phase information for select layer lines of the individual datasets included in the final average. As in Figure 3-5, clustering of the datasets shows the reliable resolution of the 3D reconstruction to be ~25 Å.

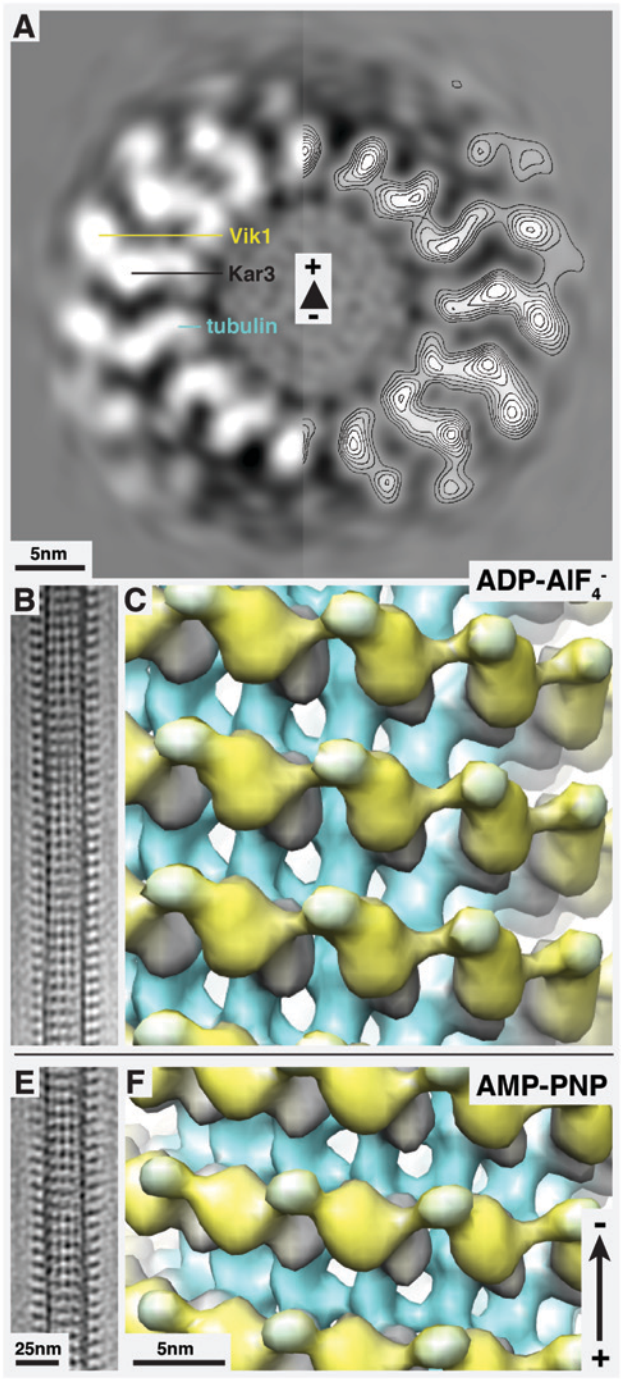

Figure 3-7: Cryo-EM helical reconstruction of Kar3Vik1-MTs in the ADP-P_i state.
(A) 3.8 Å cross-sectional slice through the helical average of MTs decorated with WT GCN4-Kar3Vik1 in the presence of ADP-AlF_4^-. **(B)** Fourier-filtered image of one of the MTs included in the final average. **(C)** Surface rendering of the helical average shows that when incubated with ADP-AlF_4^-, Kar3Vik1 adopts a MT-binding configuration very similar to that of the AMP-PNP state **(E & F)** with the coiled-coil stalk pointing toward the MT minus end. Images in **E** and **F** are the same as those shown in Figure 3-4.
Color key: tubulin - turquoise, Kar3 - gray, Vik1 - yellow, GCN4 coiled-coil - pale blue

reconstructions of unlabeled GCN4-Kar3$_{CL}$Vik1$_{C536C}$ complexed to MTs in the nucleotide-free and AMP-PNP states were indistinguishable from those of WT GCN4-Kar3Vik1 (Figure 3-9A and B) indicating that the replaced residues in the single-cysteine construct did not have adverse effects on motor function.

Nanogold®-labeled GCN4-Kar3$_{CL}$Vik1$_{C536C}$ binds to MTs in a manner akin to unlabeled GCN4-Kar3$_{CL}$Vik1$_{C536C}$ and WT GCN4-Kar3Vik1 as visualized by cryo-EM (Figure 3-8), showing that the presence of the 1.4 nm gold particle did not obstruct Kar3Vik1's MT binding site in the nucleotide-free and AMP-PNP states.

Three-dimensional maps obtained by helical reconstruction of Nanogold®-labeled GCN4-Kar3$_{CL}$Vik1$_{C536C}$ bound to MTs in the nucleotide-free state showed a distinct additional density on the globular domain extending away from the MT (Figure 3-9C, Figure 3-10C and E). Similarly, in the AMP-PNP state, a clear extra density protruding from the outer globular domain of the heterodimer was detected (Figure 3-9D, Figure 3-10D and F). Difference mapping, carried out to compare helical reconstructions of unlabeled GCN4-Kar3$_{CL}$Vik1$_{C536C}$ and Nanogold®-labeled GCN4-Kar3$_{CL}$Vik1$_{C536C,}$ showed that the additional density in both states is statistically significant ($P < 0.001$) and corresponds to the position of the Nanogold® label with high probability (Figure 3-9). These results confirm that in the nucleotide-free and AMP-PNP states, it is Kar3 in contact with the MT while Vik1 remains detached.

Vik1 causes slight changes in Kar3's interaction with the MT

In Chapter 2, I showed that Kar3MD binds stochastically to MTs, while Kar3Vik1 decorates MTs in a cooperative fashion. As Kar3 is in contact with the MT in the nucleotide-free and AMP-PNP states, I was interested in knowing whether Kar3MD alone binds to MTs in a

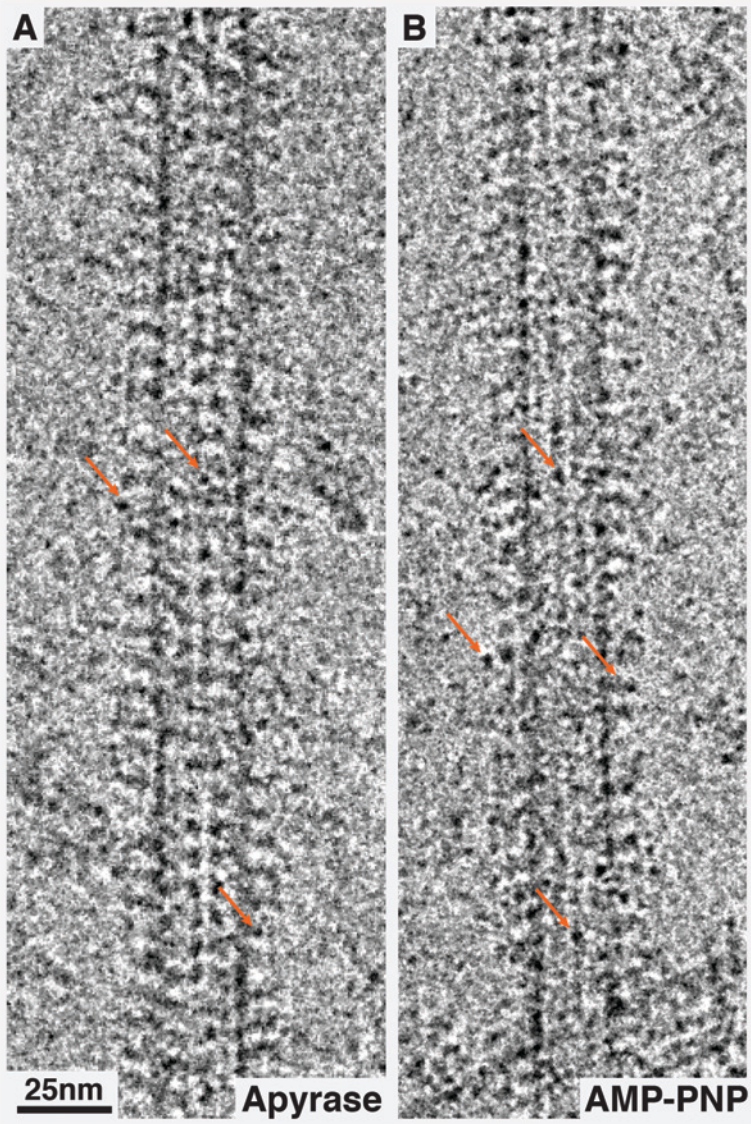

Figure 3-8: Cryo-electron micrographs of Nanogold®-labeled GCN4-Kar3$_{CL}$Vik1$_{C536C}$. MTs decorated with Nanogold®-labeled GCN4-Kar3$_{CL}$Vik1$_{C536C}$ in the nucleotide-free **(A)** and AMP-PNP **(B)** states. Orange arrows point to a few select gold particles. Due to the superposition of 3D information in these 2D projections, it is not possible to know whether the Nanogold® is localized at the domain in contact with the MT, or the domain extending away.

conformation different from that of Kar3 when in a heterodimer with Vik1. MTs were decorated with Kar3MD in the presence of AMP-PNP and analyzed by helical reconstruction (Figure 3-11A). Difference mapping was used to subtract the reconstruction of Kar3MD-AMP-PNP decorated MTs from that of WT GCN4-Kar3Vik1-AMP-PNP decorated MTs (Figure 3-11B). Statistically significant ($P < 0.001$) differences between the 3D reconstructions are shown (Figure 3-11C). It appears that when Kar3Vik1 is bound to the MT, Kar3 adopts a slightly more curved conformation than Kar3MD alone (Figure 3-11C and D). This comparison suggests that Vik1 influences the position of Kar3 at the MT, but not to a great extent.

GCN4-Kar3$_{E382C}$Vik1$_{K372C}$-M4M and SHD-Kar3Vik1$_{E355C\text{-}K423C}$-EBI can both complete the minus end directed stalk rotation

Chemical crosslinks were placed at specific locations in Kar3Vik1 to obtain additional insight into the structural changes required for Kar3Vik1 motility. For example, model A proposed for Kar3Vik1's mechanism of movement requires that the coiled-coil joining Kar3 and Vik1 separates, while in proposed model B the coiled-coil does not unwind (Figure 1-6). To differentiate between these two models, two amino acids at the base of the coiled coil stalk in Kar3 and Cik1 were replaced with cysteine residues and subsequently crosslinked with M4M, a 10 Å linker so the coiled-coil is unable to separate (Figure 3-12A) (Rank et al., submitted). This crosslinked construct, GCN4-Kar3$_{E382C}$Vik1$_{K372C}$-M4M (hereafter referred to as GCN4-Kar3Vik1-M4M) was analyzed by cryo-EM and helical reconstruction to gain structural insight into how the 10 Å constraint affects Kar3Vik1's ability to perform the coiled-coil stalk rotation.

2D projections of MTs decorated with GCN4-Kar3Vik1-M4M in the nucleotide-free and AMP-PNP states appeared similar to those of WT GCN4-Kar3Vik1 (Figure 3-12). In the AMP-

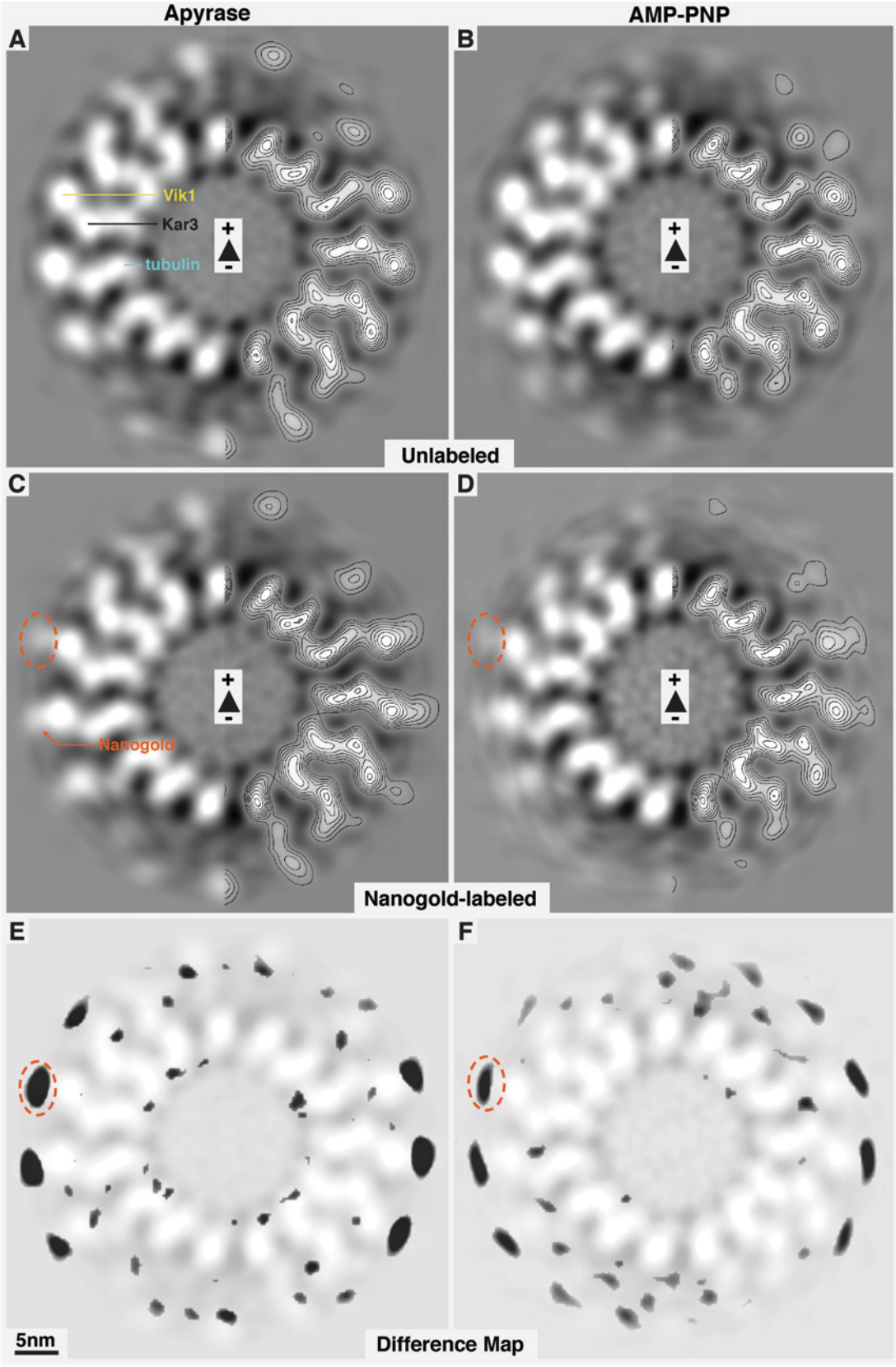
Apyrase
AMP-PNP
A
B
Vik1
Kar3
tubulin
+
-
Unlabeled
C
D
Nanogold
Nanogold-labeled
E
F
5nm
Difference Map

Figure 3-9: Cryo-EM helical reconstruction and comparison of unlabeled and Nanogold®-labeled Kar3$_{CL}$Vik1$_{C536C}$-MT complexes. (A & B) 3.8 Å cross-sections through helical averages of MTs decorated with GCN4-Kar3$_{CL}$Vik1$_{C536C}$ that has not been labeled with Nanogold®, in the nucleotide-free **(A)** and AMP-PNP **(B)** states. These maps appear indistinguishable from those of WT GCN4-Kar3Vik1 (Figure 3-4). **(C & D)** 3.8 Å cross-sections through helical averages of MTs decorated with Nanogold-labeled GCN4-Kar3$_{CL}$Vik1$_{C536C}$. An additional density (orange circle) corresponding to the Nanogold® is clearly seen protruding from the domain extending away from the MT in both the nucleotide-free **(C)** and AMP-PNP states **(D)**. **(E)** Difference map calculated by subtracting the unlabeled map in **A** from the Nanogold®-labeled map in **C**. Differences that are statistically significant for $P < 0.001$ are shown as black densities. The helical average from **C** is overlaid on the difference map to show that the significant differences correspond to the position of the Nanogold® providing evidence that Vik1 is the outer domain and Kar3 is in contact with the MT. **(F)** Difference map obtained by subtracting the average in **B** from the average in **D**, overlaid with the average from **D**, shows similar results for the AMP-PNP state.

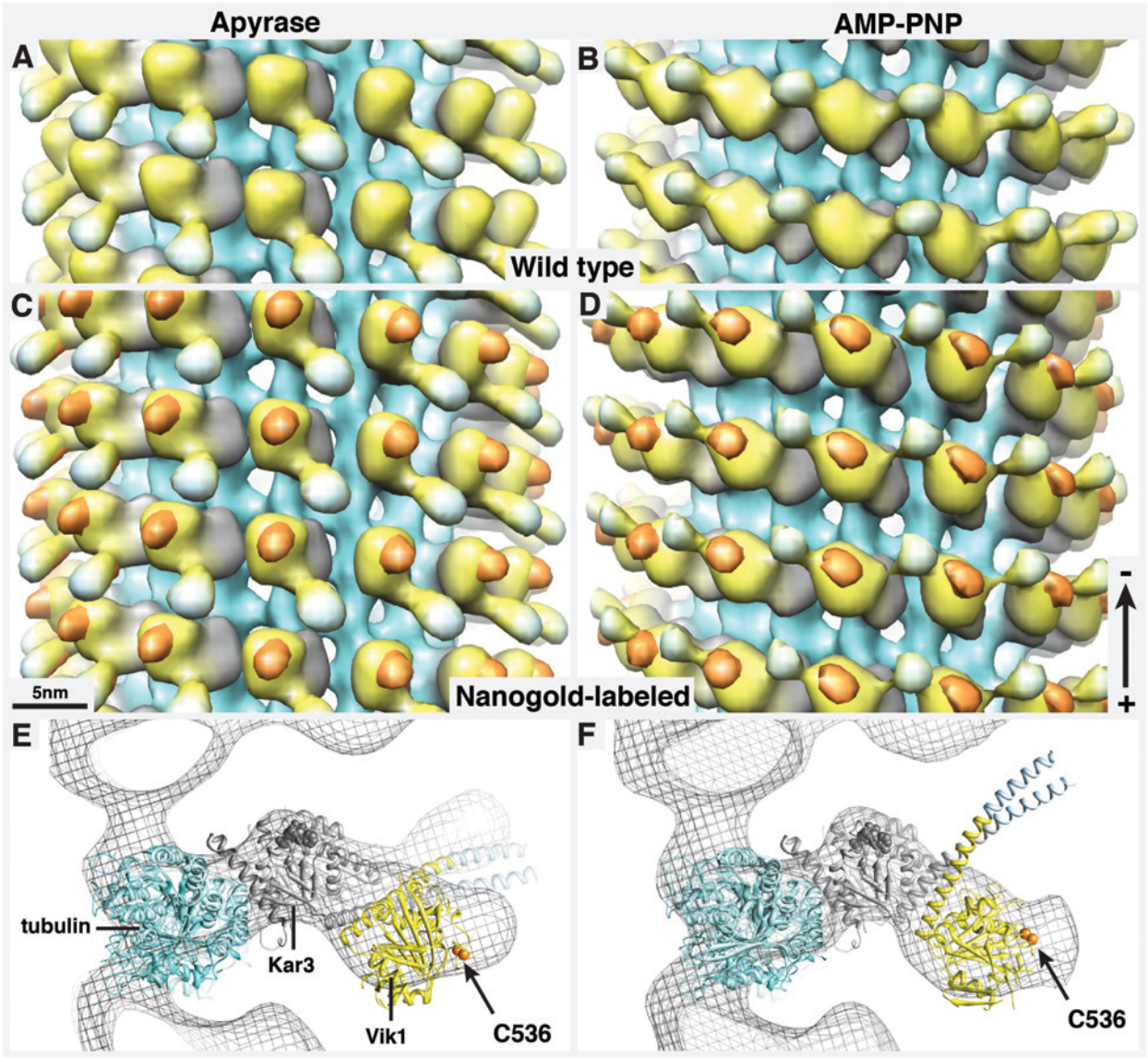

Figure 3-10: Nanogold®-labeling shows Kar3 is in contact with the MT in the nucelotide-free and AMP-PNP states. Longitudinal views of helical averages of Nanogold®-labeled GCN4-Kar3$_{CL}$Vik1$_{C536C}$ in the nucleotide free **(C)** and AMP-PNP **(D)** states. The density corresponding to the gold label is colored orange. **(A & B)** Surface renderings of WT GCN4-Kar3Vik1-MT helical averages are shown for comparison. **(E & F)** The X-ray crystal structures of tubulin (PDB accession: 1JFF; Lowe et al., 2001) and Kar3Vik1 (Rank et al., submitted) docked into the scaffolds of Nanogold®-labeled GCN4-Kar3$_{CL}$Vik1$_{C536C}$ helical averages in the nucleotide-free **(E)** and AMP-PNP states **(F)**. Vik1 C536, the residue that was labeled with the Nanogold® is colored in orange showing close agreement with the location of the Nanogold® in the helical reconstructions.
Color key: tubulin - turquoise, Kar3 - gray, Vik1 - yellow, GCN4 coiled-coil - pale blue, Nanogold® - orange

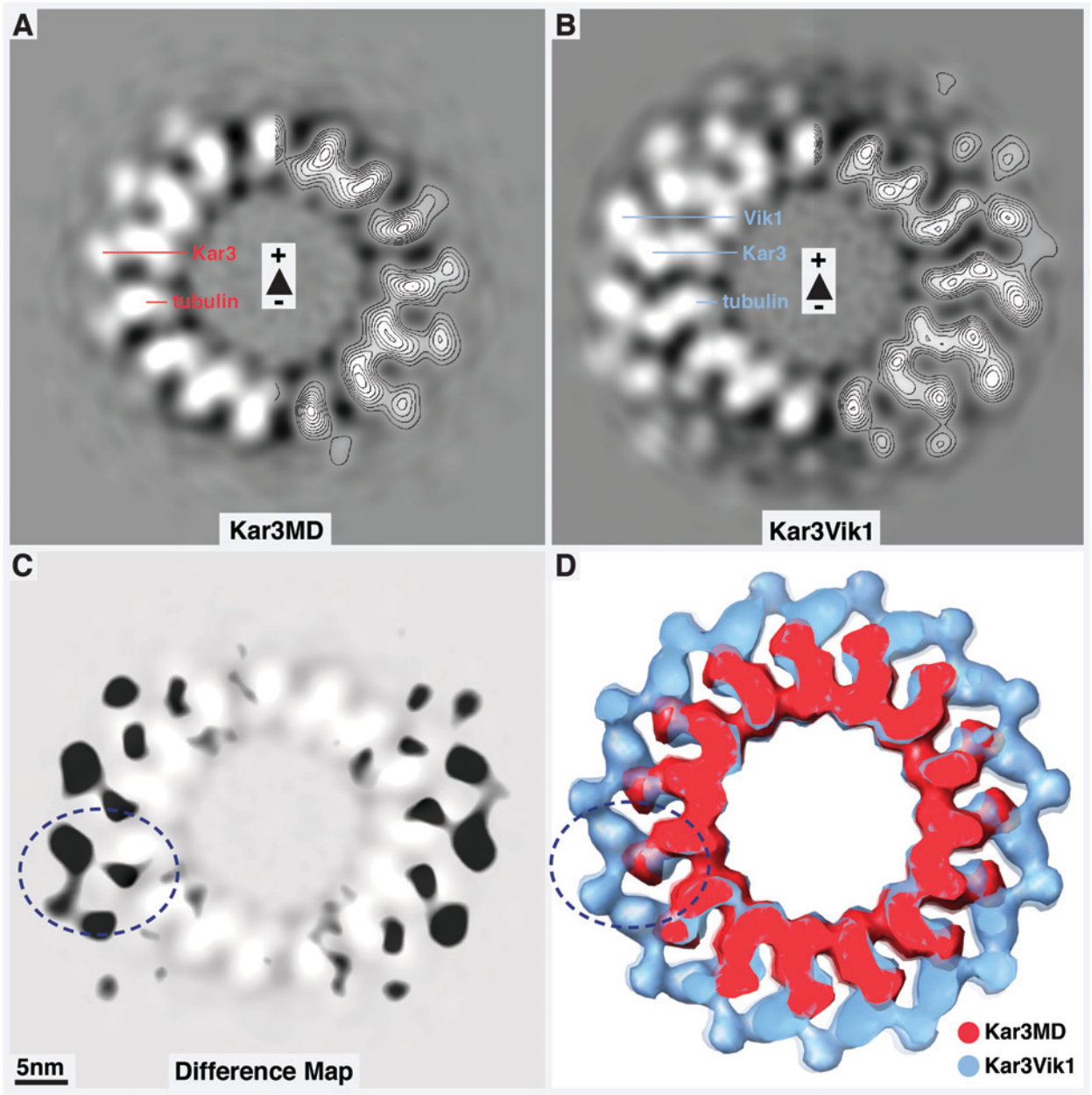

Figure 3-11: Vik1 causes only slight changes in Kar3's interaction with MTs. (A) 3.8 Å cross-section through a helical reconstruction of MTs decorated with Kar3MD in the AMP-PNP state. For comparison, a slice through a reconstruction of MT's decorated with WT GCN4-Kar3Vik1-AMP-PNP (Figure 3-4) is shown in **B**. **(C)** Difference map obtained by subtracting the Kar3MD-MT average in **A** from the Kar3Vik1-MT average in **B**. Significant differences ($P < 0.001$) are shown in black. The cross-section in **A** is overlaid on the difference map for clarity. In addition to the density corresponding to Vik1 and the coiled-coil stalk, a small significant change in Kar3's position is seen (navy circle). **(D)** Overlay of surface renderings of the Kar3MD-MT average (red) and Kar3Vik1-MT average (blue). The overlay shows how Kar3 adopts a slightly more curved conformation relative to the MT when complexed with Vik1 than Kar3MD alone.

PNP state MTs were never fully decorated, though this could be due to aggregated motors (thus a lower concentration of active motors) in the solution rather than a direct effect of the crosslink.

The helical reconstruction of GCN4-Kar3Vik1-M4M in the nucleotide-free state is indistinguishable from that of WT GCN4-Kar3Vik1 (Figure 3-13A-C). Similarly, the average of GCN4-Kar3Vik1-M4M in the AMP-PNP state shows that this construct is able to carry out the 90° stalk rotation similar to WT GCN4-Kar3Vik1 (Figure 3-13D-F). The maps appear slightly different because the MTs incubated with GCN4-Kar3Vik1-M4M were less decorated by the motor than those with GCN4-Kar3Vik1. These findings suggest that the 10 Å crosslink does not constrain the movements necessary for the powerstroke to occur and that unwinding of the coiled-coil is not required for the stalk rotation. Though, these results do not exclude the possibility that the coiled-coil has to separate at another point during Kar3Vik1's motility cycle.

A second crosslinked construct, SHD-Kar3Vik1$_{E355C\text{-}K423C}$-EBI (hereafter referred to as SHD-Kar3Vik1-EBI) was tested. This construct has a cysteine inserted into Vik1's coil and a second cysteine placed in Vik1's globular domain. The cysteines are crosslinked with EBI, a 12 Å linker, thus securing Vik1's core domain to the coiled-coil (Figure 3-14A) (Rank et al., submitted). This crosslink tests whether the core domain of Vik1 has to rotate or detach completely from the coiled-coil to facilitate movement.

Cryo-EM of MTs decorated with SHD-Kar3Vik1-EBI in the nucleotide-free and AMP-PNP states showed MT binding similar to WT GCN4-Kar3Vik1 (Figure 3-14), and the helical reconstruction of SHD-Kar3Vik1-EBI bound to MTs in the nucleotide-free state was indistinguishable from WT GCN4-Kar3Vik1 (Figure 3-15A-C). The helical average of SHD-

Kar3Vik1-EBI in the AMP-PNP state shows that SHD-Kar3Vik1-EBI can complete the 90° stalk rotation as visualized for WT GCN4-Kar3Vik1 (Figure 3-15D-F). However, there is also an additional stalk density in the reconstruction which could indicate that a subset of the SHD-Kar3Vik1-EBI population remains trapped in the nucleotide-free state position with the stalk still pointing toward the MT plus end. These data suggest that Vik1 does not detach from the coiled-coil to facilitate the powerstroke, however some rotation of Vik1 relative to the stalk may be necessary for coordinating the stalk rotation.

Kar3Vik1 crystal structure docking into cryo-EM maps indicates close agreement with the MT-bound nucleotide-free state conformation

The presence of the EBI crosslink in SHD-Kar3Vik1-EBI had a significant stabilizing effect on the heterodimer allowing the X-ray crystal structure of SHD-Kar3Vik1-EBI to be solved recently (Rank et al., submitted). I used this crystal structure to improve understanding of the structural configurations in our three-dimensional cryo-EM maps obtained from helical reconstruction (Figure 3-16). Treating the SHD-Kar3Vik1-EBI crystal structure as a rigid-body, both interactive and quantitative methods were used to dock the structure into the EM maps.

Docking of SHD-Kar3Vik1-EBI into the cryo-EM scaffolds revealed an excellent fit into the nucleotide-free state EM map, despite the ADP bound in the crystal structure (Figure 3-16A and B). The close fit into the nucleotide-free binding state map suggests that relatively little conformational change occurs when Kar3 comes into contact with the MT. This marked structural agreement also confirms that the retrograde stalk rotation is unlikely to occur when ADP is released from the active site upon MT binding as has been proposed previously (Yun et

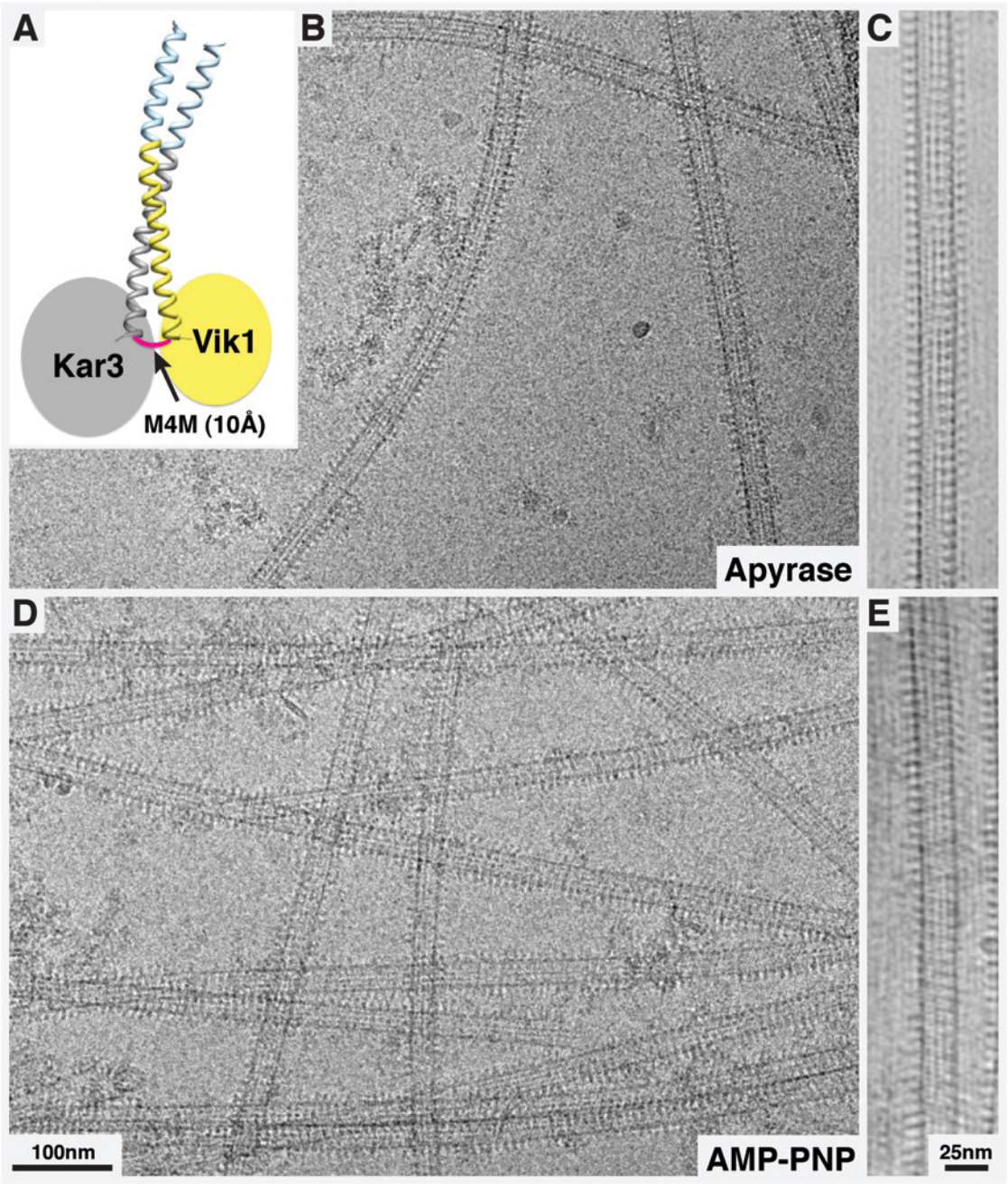

Figure 3-12: Cryo-EM of GCN4-Kar3Vik1-M4M bound to MTs. (A) Cartoon showing the location of the M4M chemical crosslink. M4M creates a 10 Å crosslink between two cysteine residues at the base of the coiled-coil stalk. **(B)** Cryo-electron micrograph of MTs decorated with GCN4-Kar3Vik1-M4M in the nucleotide-free state. **(C)** Fourier filtered MT in the nucleotide-free state shows a motor configuration similar to WT GCN4-Kar3Vik1 (Figure 3-4). Cryo-electron micrograph **(D)** and Fourier filtered image **(E)** of MTs decorated with GCN4-Kar3Vik1-M4M in the AMP-PNP state. Fourier filtering **(E)** shows that the MT is not completely decorated by the motor.

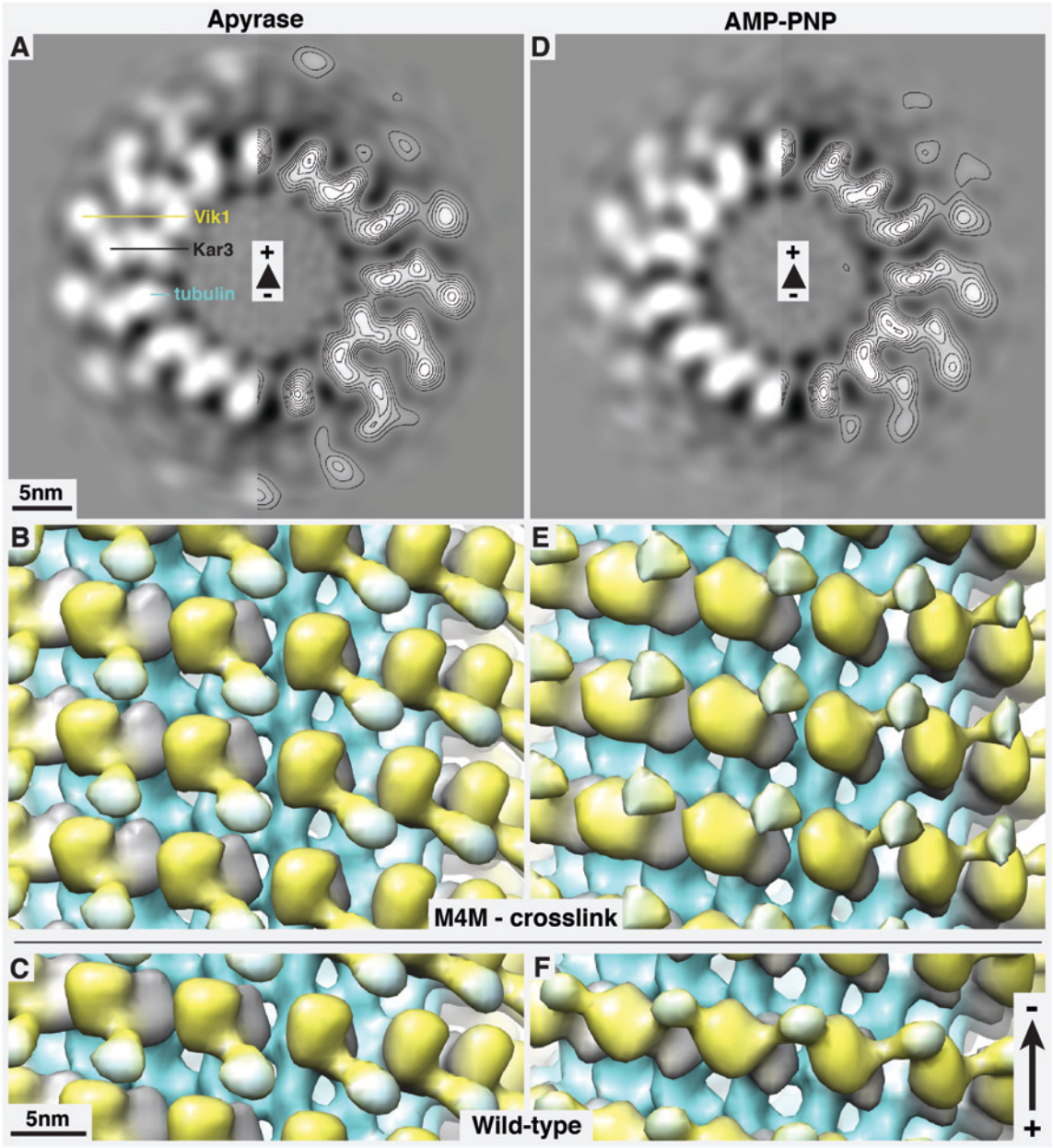

Figure 3-13: Helical reconstruction of GCN4-Kar3Vik1-M4M (10 Å crosslink at base of the coiled-coil). Helical averages of MTs decorated with GCN4-Kar3Vik1-M4M in the nucleotide-free **(A & B)** and AMP-PNP **(D & E)** states. **A & D** show 3.8 Å cross sectional slices through the MT. **B & E** show surface renderings of the averages with the MT minus-end pointing toward the top of the page. Surface renderings of WT GCN4-Kar3Vik1 reconstructions are shown in **C & F** for comparison. In the nucleotide-free state, the M4M crosslinked construct is indistinguishable from WT GCN4-Kar3Vik1. The AMP-PNP state shows that GCN4-Kar3Vik1-M4M is able to complete the minus-end directed stalk rotation similar to WT GCN4-Kar3Vik1 but the surface renderings appear different because MTs included in the GCN4-Kar3Vik1-M4M average were not completely decorated and thus the map has a lower signal to noise ratio. **Color key:** tubulin - turquoise, Kar3 - gray, Vik1 - yellow, GCN4 coiled-coil - pale blue

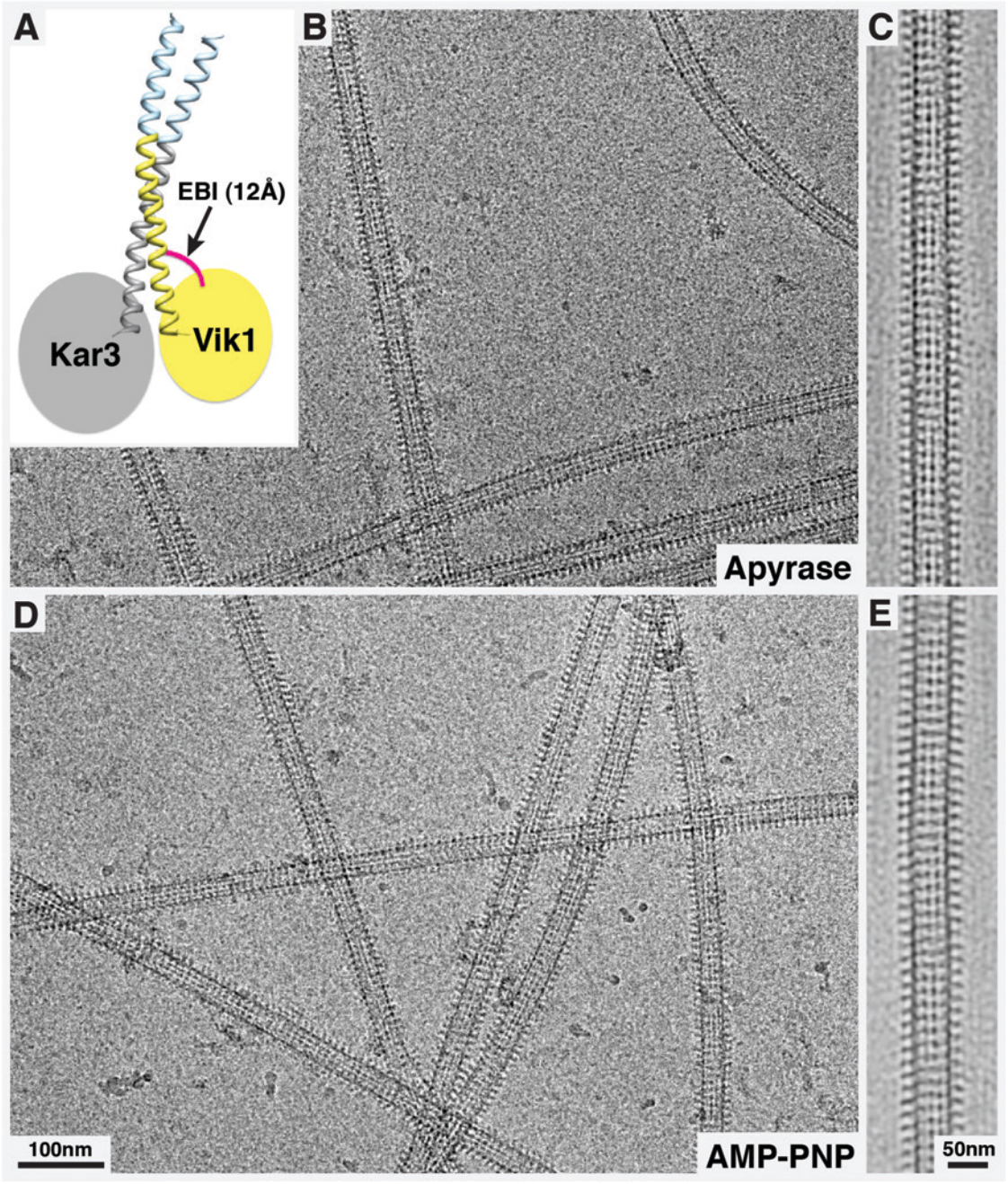

Figure 3-14: Cryo-EM of SHD-Kar3Vik1-EBI bound to MTs. (A) Cartoon showing the location of the EBI crosslink. EBI creates a 12 Å crosslink between a cysteine residue in the stalk coil of Vik1 and a second cysteine in the globular domain of Vik1. Cryo-electron micrograph **(B)** and Fourier filtered image **(C)** of MTs decorated with SHD-Kar3Vik1-EBI in the nucleotide-free state. Cryo-electron micrograph **(D)** and Fourier filtered image **(E)** of MTs decorated with SHD-Kar3Vik1-EBI in the AMP-PNP state. In both states the MTs are completely decorated by the crosslinked motor in configurations similar to WT GCN4-Kar3Vik1.

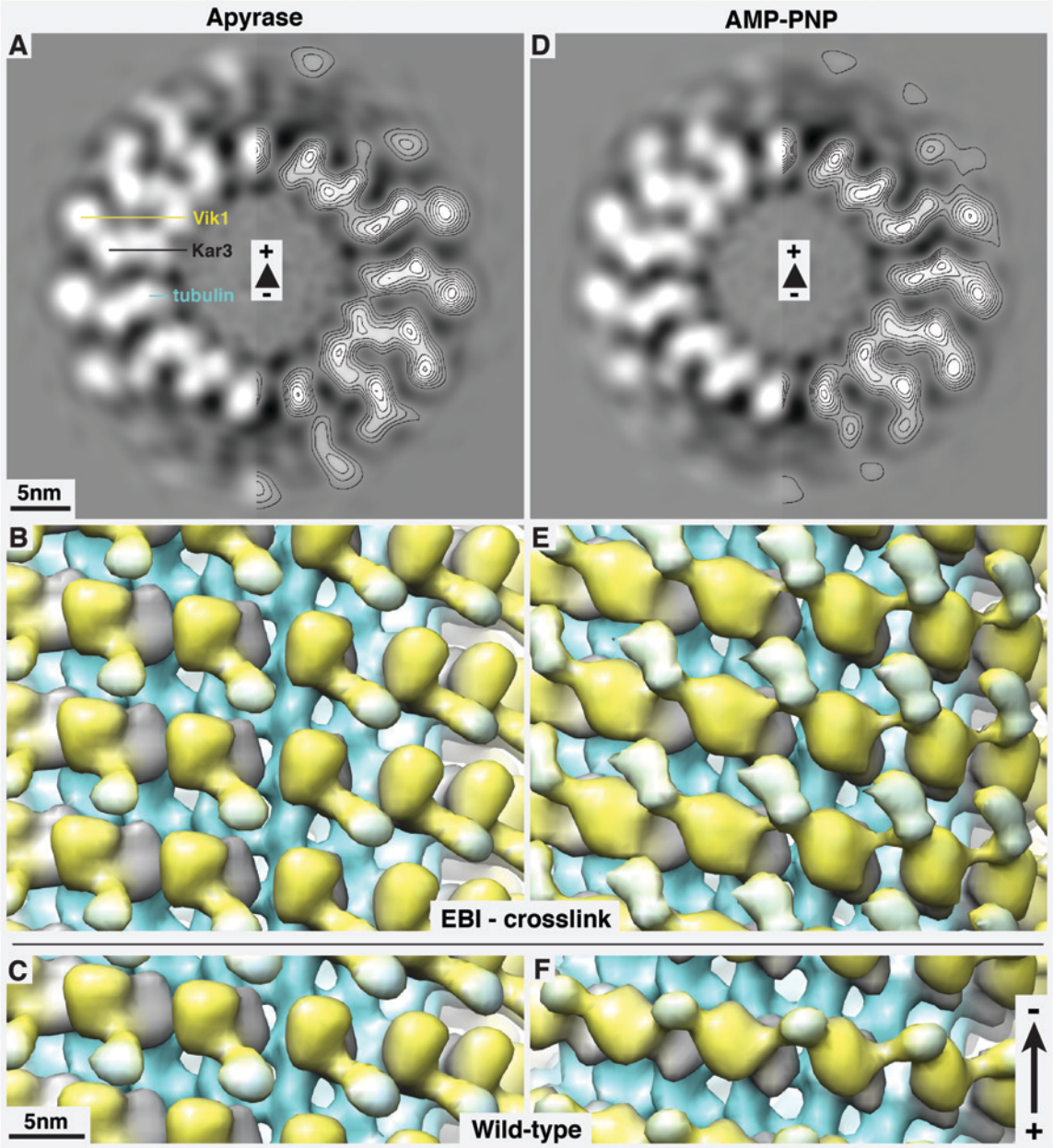

Figure 3-15: Helical reconstruction of SHD-Kar3Vik1-EBI (12 Å crosslink between the stalk and Vik1 core). Helical averages of MTs decorated with SHD-Kar3Vik1-EBI in the nucleotide-free **(A & B)** and AMP-PNP **(D & E)** states. **A & D** show 3.8 Å cross sectional slices through the MT. **B & E** are surface renderings of the averages. Surface renderings of WT GCN4-Kar3Vik1 reconstructions are shown in **C & F** for comparison. In the nucleotide-free state, the EBI crosslinked construct is indistinguishable from WT GCN4-Kar3Vik1. The AMP-PNP state shows that SHD-Kar3Vik1-EBI is able to complete the powerstroke similar to WT GCN4-Kar3Vik1. However, the presence of an additional density at the stalk suggests that a subset of the crosslinked motors remain trapped in the nucleotide-free state conformation with the stalk pointing toward the MT plus end.
Color key: tubulin - turquoise, Kar3 - gray, Vik1 - yellow, SHD coiled-coil - pale blue

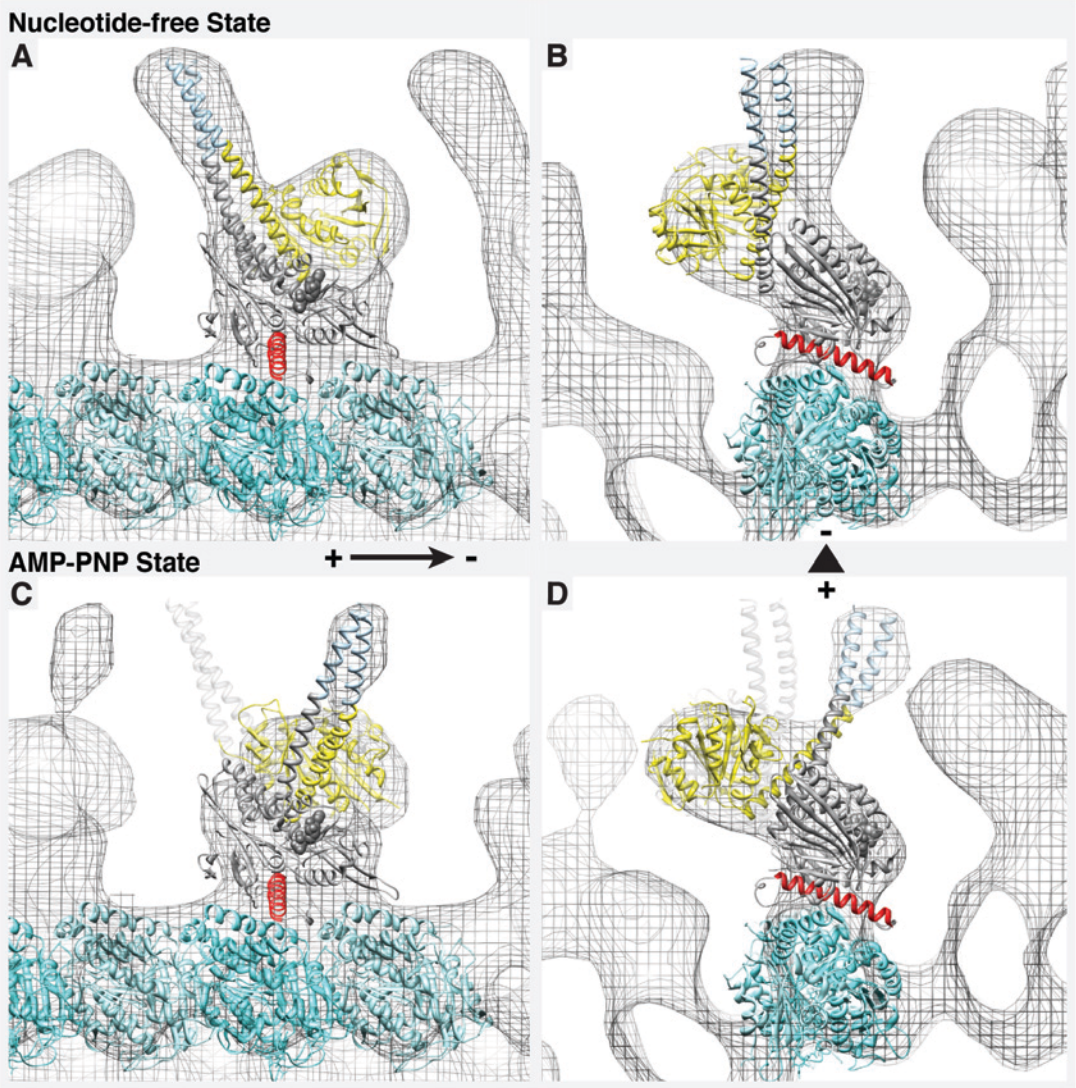

Figure 3-16: The SHD-Kar3Vik1-EBI crystal structure agrees well with cryo-EM data. Docking of the Kar3Vik1 X-ray crystal structure into the 3D maps obtained from helical averaging of WT GCN4-Kar3Vik1-decorated MTs in the nucleotide-free **(A & B)** and AMP-PNP **(C & D)** states. **A** and **C** show views along the MT length with the minus end pointing to the right. **B** and **D** provide views through the MT cross-section with the minus end pointing away from the reader. The ADP-state crystal structure fits extremely well into the map of WT GCN4-Kar3Vik1 in the nucleotide-free state, suggesting that only small structural changes occur when Kar3 makes contact with the MT. In the AMP-PNP state, the Kar3 head remains well-docked in the cryo-EM map, indicating that uptake of ATP causes small changes in Kar3's nucleotide-binding pocket that are transmitted into a large structural rearrangement of Vik1 and the stalk to position the stalk toward the minus end of the MT. To fit into the maps in **C** and **D**, Vik1 and the stalk were rotated at G385 on Kar3 by approximately 90° around an axis perpendicular to the stalk. In **C** and **D**, the docked position of Kar3Vik1 in the nucleotide-free state is shown in transparent gray. Helix α4 of Kar3 is colored in red in all the maps to orient the reader.
Color Key: Kar3 - gray; Helix α4 of Kar3 - red ; Vik1 - yellow; SHD coiled-coil - pale blue; α-tubulin - light turquoise; β-tubulin - dark turquoise

al., 2003, Hirose et al., 2006), and instead takes place upon uptake of ATP. Similar agreement between the ADP-bound Ncd crystal structure and the cryo-EM maps of Ncd complexed to MTs in the nucleotide-free state has been reported (Wendt et al., 2002, Endres et al., 2006).

To fit the SHD-Kar3Vik1-EBI crystal structure into the AMP-PNP-state map, the heterodimer was separated into two components: the Kar3 head domain (residues Gly^{385}-Lys^{729}), and the complete Vik1 domain with the coiled-coiled stalk. The Kar3 head remained well-docked into the maps of the AMP-PNP state, indicating that only slight, or no rotation of Kar3 occurs upon uptake of AMP-PNP. Conversely, Vik1 and the stalk had to be rotated by approximately 90° around an axis perpendicular to the coiled-coil to fit optimally into the electron density map (Figure 3-16C and D). This close fit was obtained by rotating Vik1 and the stalk as a rigid body, reinforcing the notion that contacts between the coiled-coil and Vik1's core remain intact during the retrograde powerstroke.

Discussion

I have successfully used cryo-EM in combination with helical reconstruction to directly visualize a rotation of Kar3Vik1's coiled-coil stalk. Using site-specific Nanogold®-labeling, I could unambiguously demonstrate that Kar3 is the domain in contact with the MT during this stalk rotation. These results illustrate that in the nucleotide-free state, Kar3Vik1's coiled-coil stalk is positioned toward the MT plus end. In the presence of AMP-PNP, Vik1 and the stalk are rotated 90° from their nucleotide-free state position so the stalk points toward the MT minus end. This large structural rearrangement of the stalk seen in the presence of AMP-PNP is likely to be a crucial part of the mechanism that Kar3Vik1 uses for retrograde motion. My cryo-EM data are consistent with the stalk rotation occurring upon uptake of ATP, rather than upon loss of ADP

from the active site as was once proposed for Ncd (Yun et al., 2003) and for Kar3 (Hirose et al., 2006).

The similarity of the AMP-PNP and ADP-AlF_4^- states (Figure 3-7) suggests that it is not the hydrolysis of ATP that resets the position of the stalk to the plus end direction. Rather, ATP-hydrolysis changes Kar3 to a weak MT-binding state that allows it to detach from the MT, either before or after the release of phosphate from the active site.

While Vik1 and the stalk undergo a rotation upon ATP-binding, Kar3 appears to maintain its position on the MT and does not, or only slightly, rotates with the rest of the complex. This result is unlike those reported for kinesin-1 (Rice et al., 1999) and KIF1A (Kikkawa et al., 2001) which are both proposed to rotate on the microtubule upon uptake of ATP. However, this result is consistent with the findings of Hirose et al. (2006), whose cryo-EM work with the monomeric Kar3MD did not show a rotation of Kar3 on the MT in response to changes in nucleotide state. Hence, the binding of ATP to the active site triggers rearrangements that are transmitted through the molecule to initiate rotation of the coiled-coil. The resolution in the cryo-EM maps is not high enough to be able to detect the movements responsible for this. Previously suggested models have proposed that conformational changes in helix α4 of Kar3 (see Figure 3-16) and a subsequent shift of the central β-sheet are likely to be important for communicating the presence of nucleotide to the rest of the complex (Hirose et al., 2006).

Chemical crosslinks engineered to impose constraints on Kar3Vik1 at two different positions provide additional insight into Kar3Vik1's mechanism of movement. Motility experiments with GCN4-Kar3Vik1-M4M have shown that this mutant, with a 10 Å crosslink at

the base of the stalk, can glide MTs at a speed similar to WT Kar3Vik1. However, after 20 minutes, a large percentage of the MTs have stopped moving and appear to be detached from the motors (Rank et al., submitted). It has been proposed that this detachment results from a lack of coordination in the motor domains. The cryo-EM data presented here show that GCN4-Kar3Vik1-M4M can complete the full 90° rotation of the stalk as seen for WT GCN4-Kar3Vik1. This result is consistent with the motility data because if coordinated motion of the motors is lost over time, this will not be visible in the helical reconstruction. My findings suggest that the coiled-coil stalk does not need to unwind in order to generate the minus-end directed stalk rotation, but taken together with the motility results, it cannot be excluded that the 10 Å linker constrains movements necessary at other points in Kar3Vik1's motility cycle.

Helical reconstruction of SHD-Kar3Vik1-EBI shows that this construct, with the Vik1 head domain secured to the coiled-coil, is able to execute the full 90° stalk rotation. However, in the presence of AMP-PNP, this crosslinked construct shows an additional stalk-related density that coincides with the position of the stalk in the nucleotide-free state. This result suggests that a subset of the SHD-Kar3Vik1-EBI population remains trapped in the nucleotide-free state position with the stalk pointing toward the MT plus end. These data are consistent with motility results reporting that SHD-Kar3Vik1-EBI is able to glide MTs, but at a slightly slower velocity than WT Kar3Vik1 (Rank et al., submitted). These findings imply that the coiled-coil stalk does not need to detach from the Vik1 head to facilitate Kar3Vik1's powerstroke. However, it is possible that the 12 Å linker constrains some rotation of Vik1 relative to the stalk that is necessary for efficient uptake of nucleotide, or for properly signaling the presence of nucleotide in Kar3's active site to the rest of the molecule.

The coiled-coil stalk rotation of Kar3Vik1 described here is strongly reminiscent of the 'lever arm' rotation that has been reported for Ncd (Wendt et al., 2002; Endres et al., 2006). This indicates a conservation of a mechanism of movement among the minus end directed kinesins and is discussed in further detail in Chapter 6.

Chapter 4. Utilizing the helical and non-helical MT binding properties of Kar3Vik1 to drive development of subvolume averaging software

A large portion of the material in this section can be found in the following two references:

Cope, J., S. Gilbert, I. Rayment, D. Mastronarde, and A. Hoenger. 2010. Cryo-electron tomography of microtubule-kinesin motor complexes. *J Struct Biol*. 170:257-265.

Cope, J., J. Heumann, and A. Hoenger. 2011. Cryo-electron tomography for structural characterization of macromolecular complexes. *Curr Protoc Protein Sci*. 65:17.13.1-17.13.31.

Introduction

An overview of electron tomography

The principle of electron tomography (ET) has been in use for many years but was first applied to biological material in the late 1960's (De Rosier and Klug, 1968) and the recent advent of digital cameras, automated tilt series acquisition software and improved computational possibilities have given tomography a renewed boost (Lučić et al., 2005, Vanhecke et al., 2010). The principle of ET is based on the central section theorum described in Chapter 3, which postulates that the Fourier transforms of 2D projections through an object at different tilt angles correspond to central slices of the object in 3D Fourier space. In Chapter 3, where reconstruction of helical MTs is described, the helical path of the MT 'tilts' the object of interest for us at all angles needed to obtain a complete 3D reconstruction. For specimens that lack helical symmetry, their 3D structure can be determined by tilting the specimen in the EM and collecting a series of 2D projections taken at various angles (Figure 4-1A). These tilt series projections, which aim to sample as much of Fourier space as possible, are then used to reconstruct the 3D structure by a mathematical reconstruction algorithm, such as weighted back-projection (Figure 4-1B). The

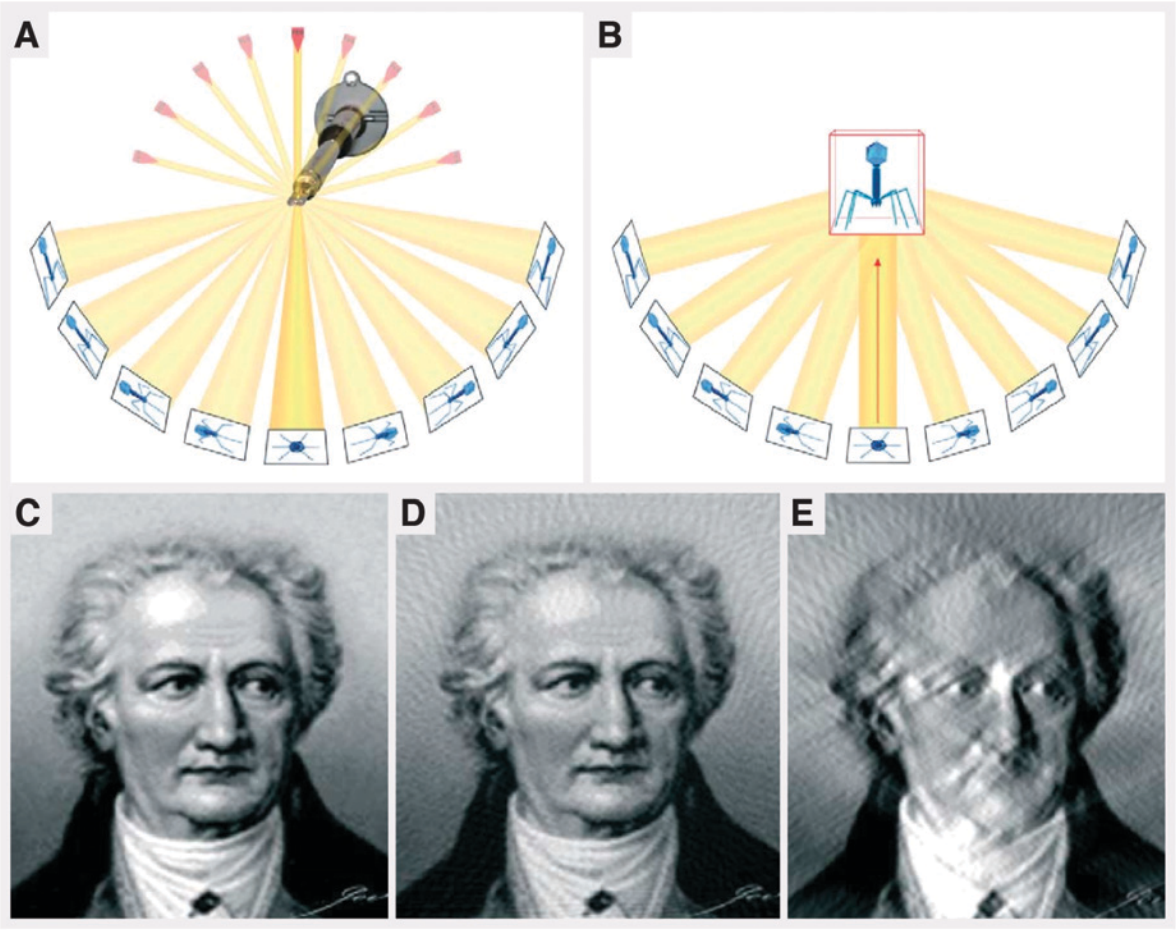

Figure 4-1: The principles of ET. (A) A series of 2D projections of the specimen of interest is collected by tilting the specimen in the EM and taking an image every ~1.5° for a ±60° tilt range. **(B)** A weighted backprojection process is then used to computationally create a 3D reconstruction of the specimen from the images collected in the tilt series. **(C)** An image of Goethe is used to represent a 2D projection of a 3D object. **(D)** A reconstruction of Goethe as would be achieved from collecting a series of tilted images every 2° over a ±90° tilt range. The ripples are introduced because images are collected only every 2°. Including more images in the reconstruction by collecting images at a smaller tilt increment would reduce the size of the ripples. In cryo-EM, the sensitivity of the sample greatly limits the number of images that can be acquired of the specimen of interest. **(E)** A reconstruction of Goethe showing the effect of the missing wedge resulting from collecting images between ±60° instead of ±90°. The missing wedge causes degradation of the data predominantly in the plane perpendicular to the tilt axis. The vertical detail in the image, such as Goethe's ear and nose, is well preserved, while a loss of resolution is strongly apparent in the horizontal detail, such as Goethe's mouth (McIntosh et al., 2005).

resulting 3D reconstruction, known as a tomogram, has the remarkable advantage of being able to be rotated and 'sliced' computationally in any direction at any position or orientation. Slices can be as thin as a single voxel (typically 0.5 - 1 nm^3) providing views without interference from structures (or noise) above or below the selected slice.

The major advantage of cryo-ET is that no initial assumptions about symmetry or shape are made and it is thus uniquely suited to the study of any complex cellular structure. In many cases, macromolecular complexes can be identified and studied directly within cryo-tomograms, especially if the complex has a distinct shape. MTs (Bouchet-Marquis et al., 2007), actin filaments, ribosomes (Medalia et al., 2002), and the Golgi apparatus (Bouchet-Marquis et al., 2008), are just a few examples. The 26s proteasome has been identified in its native context because of its characteristic shape (Medalia et al., 2002) and ATP-synthase molecules have been seen in cryo-tomograms of isolated mitochondria (Nicastro et al., 2000).

While being well suited to complex cellular structures, cryo-ET can also be applied to purified complexes isolated from cells. However, isolated complexes are whenever possible, traditionally studied using 2D image averaging techniques such as electron crystallography, single particle or icosahedral reconstruction, and helical reconstruction. These are all well-established methods for recovering 3D structural information from 2D projections and have yielded spectacular results to high resolution (e.g. Gonen et al., 2005, Sachse et al., 2007, Zhang et al., 2010). However, these methods rely strictly on averaging 2D projections containing various views of an identical structure and in some cases take advantage of an intrinsic symmetry of the macromolecule being studied. As such, identical, inflexible complexes, 2D crystalline arrays, perfect icosahedrons or helices are required. Furthermore, the nature of averaging means that small isolated changes in individual macromolecules get averaged out during image

processing and cannot be visualized in final averages. In this chapter, I show the benefits of applying cryo-ET to isolated complexes using *in vitro* prepared kinesin-decorated MTs as an example.

The need for subvolume averaging

In Chapter 2, I described the advantages of using vitrification as a means of immobilizing samples to visualize them as close as possible to their native hydrated state. Unfortunately, a major setback of cryo-EM is that frozen-hydrated specimens are extremely sensitive to the electron beam and valuable structural information is quickly lost at high electron doses. This is particularly problematic for cryo-ET which requires ~80 images of the same imaging area at different tilt angles. Thus, the total dose that can be applied to the specimen during tilt series acquisition is limited (typically 1 electron/$Å^2$ per image) which results in a very low signal-to-noise ratio.

In addition, being able to tilt a sample only from ±70° or less (instead of ±90°) results in a 'missing wedge' of information that introduces smearing and other artifacts into the reconstruction (Figure 4-1C-E). For a ± 60° tilt range the effects of the missing wedge typically limit the resolution of cryo-tomograms by a factor of 1.5-2 in the direction parallel to the electron beam. Thus, a software package for aligning and averaging assumed identical subvolumes from tomograms has been developed in our lab as a means of increasing the signal-to-noise ratio and reducing missing wedge effects (Nicastro et al., 2006). The goal of the work presented here was to test the application and demonstrate the benefits of the subvolume averaging software utilizing kinesin-MT complexes.

Kar3Vik1 is an ideal specimen for developing and testing subvolume averaging software

During my cryo-EM work with WT GCN4-Kar3Vik1, I noticed a number of characteristics about Kar3Vik1's interactions with MTs that did not conform to helical symmetry and thus could not be studied by helical reconstruction. An obvious characteristic is Kar3Vik1's cooperative binding pattern which provided a good dataset to test the application of the subvolume averaging software. Related to this, I noticed many occasions where Kar3Vik1 would bind preferentially between two adjacent MTs, appearing to form 'bridges' between the two MTs. I believe this to be a consequence of Kar3Vik1's cooperativity *in vitro* rather than a significant biological function. Nevertheless this binding pattern presented another opportunity for experimenting with the subvolume averaging software. Finally, Kar3Vik1 is also able to completely decorate MTs. Complete decoration of a MT that lacks a seam possesses helical symmetry and thus is ideal to test the incorporation of symmetry parameters into the subvolume averaging software, and also provide a direct comparison to kinesin-MT averages obtained by helical reconstruction. Here I demonstrate the implementation of our subvolume averaging software on kinesin-decorated MTs. The methods used here can be applied to other samples, enhancing the scope of biological questions that can be answered with cryo-ET in the future.

Materials and Methods

Preparation of kinesin-MT complexes for cryo-ET

MTs were polymerized as described in Chapter 2.

Eg5-monomer-MT complexes: Monomeric Eg5, comprising residues Met^{1}-Gln^{367} of the human Eg5 kinesin motor domain, was purified in the lab of Susan Gilbert as reported previously (Cochran et al., 2004). Eg5-monomer-MT complexes were formed in solution in the presence of

2 mM AMP-PNP (Sigma–Aldrich Corp., St Louis, MO), at a final tubulin concentration of 4.5 μM and a final Eg5 concentration of 18 μM. Eg5-MT complexes were adsorbed to C-flat holey-carbon grids (Protochips, Inc., Raleigh, NC) for 45 s and subsequently plunge-frozen into liquid ethane using a home-made plunge-freezing device.

WT GCN4-Kar3Vik1-MT complexes: MTs at a concentration of 4.5 μM were adsorbed onto grids for 45 s and excess liquid was blotted away. GCN4-Kar3Vik1 at 4.5 μM was incubated with the MTs for 2 min in the presence of 2 mM AMP-PNP and plunge-frozen as described above. 10 nm colloidal gold (Ted Pella, Redding, CA) was added to all samples before plunging for use as fiducial markers for improved alignment of images collected in the tilt-series.

CryoEM tilt-series data collection

Grids were transferred under liquid nitrogen to a Gatan-626 cryo-holder (Gatan, Inc., Pleasanton, CA) and imaged on an FEI Tecnai F20 FEG transmission EM (FEI Company, Eindhoven, The Netherlands) operating at 200kV. Tilt series were collected by tilting the grid between ± 60°, or ± 70°, and recording an image every 1.5°. Each tilt series consisted of approximately 80 low dose images. Tilt series images were acquired using a nominal magnification of 29 000 x and a defocus of -2.5 μm (Kar3Vik1-MT complexes) or -6 μm (Eg5-MT complexes). SerialEM software (Mastronarde, 2005) was used to automate the data acquisition and minimize exposure of the specimen to the electron beam. The image at zero tilt was recorded with an electron dose of 1 electron/Å^2 and the dose was varied for all other images by a factor of 1/cosine of the tilt angle. This was so that images at higher tilts were recorded with a higher dose to compensate for the increase in sample thickness. The total dose on the imaging area for each tilt series was approximately 100 electrons/Å^2. All images were recorded binned by two on a 4K x 4K Gatan

Ultrascan 895 CCD camera (Gatan, Inc. Pleasanton, CA). With this camera, at a nominal microscope magnification of 29 000 x, the pixel size corresponds to 7.6 Å on the specimen.

Tomogram reconstruction

Tomographic volumes were reconstructed from tilt series data by weighted back-projection using the IMOD software package (Kremer et al., 1996). First, X-rays and other CCD defects that appeared in tilt series images as extremely dark or extremely bright pixels were detected and replaced with an average value calculated by interpolation from surrounding pixels. Images were then aligned to each other coarsely by determining the translational shift between adjacent images based on cross-correlation peaks. Colloidal gold particles, 10 nm in diameter, were used as fiducial markers to finely and consistently align the images in the tilt series. The positions of the gold particles in the images were tracked and subsequently used to correct small differences in image rotation, translations, slight variations in magnification, or non-uniform changes in the specimen that resulted from its interaction with the electron beam. Gold particles generate strong ray artifacts when reconstructed in tomograms. These rays are undesirable because they can obscure the specimen. Thus, after aligning the images, the gold particles were erased by selecting and replacing them with pixels of average gray value. The finely aligned stack of images, with gold particles erased, was then used to compute the tomogram.

Subvolume averaging

Tomogram denoising

To enhance contrast in the tomogram for subvolume selection, tomograms were filtered using an algorithm for nonlinear anisotropic diffusion with edge enhancing diffusion (Frangakis and

Hegerl, 2001). Optimal results, judged by eye, were obtained using a K-value of 60 for 10 iterations. The filtered tomogram was used only to aid the process of modeling for particle selection (described below) and was never used as input for the subvolume averaging software.

Subvolume (particle) selection

Subvolumes for alignment and averaging were selected from tomograms by modeling with IMOD. For visualization of the MT seam and for averaging partially decorated MTs, one of the protofilaments of the MT was traced by placing a model point by hand every 15-30 nm along the length of the protofilament. At each point marking the protofilament on the surface of the MT, a corresponding model point was then placed at the center of the MT. The PEET program 'addModPts' was used to automatically fill in model points every 8 nm along the length of the MT (both along the protofilament trajectory and the MT center), the distance corresponding to one αβ-tubulin repeat. The PEET program 'ModTwist2EM' was then used to calculate the approximate twist of the MT using the points modeled along the protofilament trajectory. The information of the MT twist was used as a set of initial orientations for aligning the selected particles in the first round of alignment and averaging. To select particles for averaging the 'bridges' between two adjacent MTs, a model point was placed by hand at the center of each GCN4-Kar3Vik1 'bridge'.

Subvolume (particle) alignment and averaging

The alignment and averaging of selected subvolumes was carried out using the software package PEET (for Particle Estimation for Electron Tomography) (Nicastro et al., 2006, Cope et al., 2010). The tomogram of interest and corresponding model with selected subvolumes was input

into PEET. A single particle chosen from the model was used as an initial reference to which to align all other selected subvolumes. In the cases where an initial motive list (information of the MT twist output from ModTwist2EM as described above) was available, these were input to be used as an initial set of orientations to aid alignment of the particles to each other in the first round of averaging. In the case where no initial motive list was available, larger search angles were used and an initial motive list was generated following the first round of alignment. In all cases, the tilt angles of the tilt series from which the tomogram was reconstructed were input so that missing wedge compensation could be applied during alignment and averaging. With missing wedge compensation, weighted averaging is carried out in Fourier space so that each particle contributes only the information that lies outside its missing wedge.

Each PEET 'run' entailed aligning the selected subvolumes to the reference according to a set of user-defined search parameters that were used to find the best alignment of the particles to the reference. This process was iterative. After each round of searching and alignment, the reference was improved and the search parameters in subsequent rounds were refined for further improvement of the reference and the final average. The iteration table with typical parameters of the search angles and search radius used for each round (iteration) of alignment and averaging is shown in Table 4-1. The rotation angles in the table are such that Phi is the rotation around the first axis described below, with the second (Theta) and third (Psi) axes determined using a right handed Cartesian coordinate system. The first axis of rotation for the alignment search was defined as being the vector between two model points and was thus different for each particle. A low-pass filter with a cutoff frequency of 0.15-0.35 and a Gaussian falloff standard deviation of 0.05 was applied to the data for each iteration to remove high-frequency noise for better alignment (the filter was applied only to align the subvolumes, and not during averaging). For all

PEET runs, the reference threshold was set to include no more than two-thirds the total number of particles to prevent particles with poor cross-correlation scores from being included in the reference. Parameters were also given to instruct the software to remove any duplicate particles to prevent any one subvolume from being included multiple times and biasing the final average. The subvolume size extracted from the tomograms for averaging varied for each dataset but was in the range of 70-100 pixels in *X*, *Y* and *Z*. The number of subvolumes included in the final averages was: Figure 4-2B, 218; Figure 4-3C, 146; Figure 4-4B, 44; Figure 4-5E, 99 and Figure 4-5F, 1242.

Subvolume averages were visualized with IMOD. Isosurface rendering of the averages was carried out in IMOD and UCSF Chimera. A low-pass filter was applied to each of the averages prior to rendering to remove high-frequency noise.

Iteration number	**Angular search range** (degrees)						**Search radius** (pixels)
	Phi		Theta		Psi		
	Max	Incr.	Max	Incr.	Max	Incr.	
1	5.0	1.0	5.0	1.0	5.0	1.0	4
2	3.0	0.6	3.0	0.6	3.0	0.6	3

Table 4-1: Typical search parameters used for alignment during subvolume averaging. This table shows the search parameters used to obtain the results presented in this chapter. Continued testing and development of the PEET software by others has resulted in an improved set of search parameters which can be found in Cope et al., 2011. Search parameters are highly dataset specific and vary depending on the type of subvolume being averaged and what is already known about the relative orientations of the subvolumes to the reference being used.

Applying symmetry to a helical MT using subvolume averaging

For a 16-protofilament MT that lacks a seam, the signal-to-noise ratio was improved, and missing wedge artifacts eliminated by taking advantage of its helical properties. Subvolumes

from the 16-protofilament MT were selected by modeling with IMOD as described above. An unsymmetrized average was obtained by completing a PEET average as described above with search parameters similar to those shown in Table 4-1.

To facilitate application of the rotational averaging parameters, it was necessary to have the long axis of the MT oriented parallel to the *Y*-axis of the average. To achieve this, the final reference from the first PEET run was rotated using the IMOD program 'rotatevol' so the long axis of the MT was oriented along the *Y*-axis of the reference volume. This rotated reference was used to complete a second PEET run so that all particles were aligned to the rotated reference and the final average contained the MT in the desired orientation. To apply the rotational averaging, a third PEET run was performed. For this third run, the original tomogram and corresponding particle selection model was input into the software 16 times and treated as 16 separate volumes each with a relative orientation of 22.5° (360°/16) to each other along the *Y*-axis. For example, the first volume had a relative orientation of 0, 0, 0 in *x*, *y* and *z* respectively, the second had a relative orientation of 0, 22.5, 0, the third a relative orientation of 0, 45, 0 etc. The reference volume used was the final reference generated from the second PEET run. Similarly, the final motive list generated from the second PEET run that specified the translations and rotations required to align the particles to the reference, was used as the input initial motive list for this third PEET run.

Estimation of subvolume average resolution using Fourier shell correlation

The PEET program 'calcFSC' was used to calculate the Fourier shell correlation (FSC) to estimate the resolution of subvolume averages. The subvolumes included in the final average were divided randomly into two groups and independent averages from each of the two groups

were compared to each other by cross correlation over twenty frequency space shells from 0.025 - 0.5. FSC curves were plotted using the program 'plotFSC', which is also part of the PEET package. The curves show the average result of ten FSC calculations (i.e. splitting the data randomly in half ten different times and calculating the FSC from each of these 10 different splits). The resolution reported here was determined from the spacial frequency value corresponding to 50% correlation.

Results

Cryo-ET and subvolume averaging permit visualization of the MT seam

Most MTs that are composed of any number other than 15 or 16 protofilaments possess a lattice seam as described in Chapter 1. Monomeric head domains of the kinesin-5 Eg5 are a useful tool for studying lattice structure because (just like Kar3Vik1 and other kinesin heads) they bind to β-tubulin every 8 nm along a MT protofilament and thus provide a specific marker to differentiate between α- and β-tubulin (McIntosh et al., 2009). However, even when fully decorated with Eg5, the MT seam is generally not seen in 2D projections because of the superposition of the 3D structural information in the resulting image.

Here I have analyzed Eg5-decorated MTs by cryo-ET. Tomographic reconstructions of Eg5-decorated MTs that are tilted in the image plane provide some optimal views where the top, lumen, and bottom of the same MT can be seen in a single 4.5 nm thick tomographic slice (Figure 4-2A). A benefit of cryo-ET is illustrated in how the opposing angular orientations of the helical path on the top (toward the reader) and bottom of the MT can be clearly visualized. In a fortunate case, the MT seam can be seen directly in the tomogram (Figure 4-2A inset). At the seam there is a 4 nm shift of one protofilament relative to the other to form the A-lattice contacts.

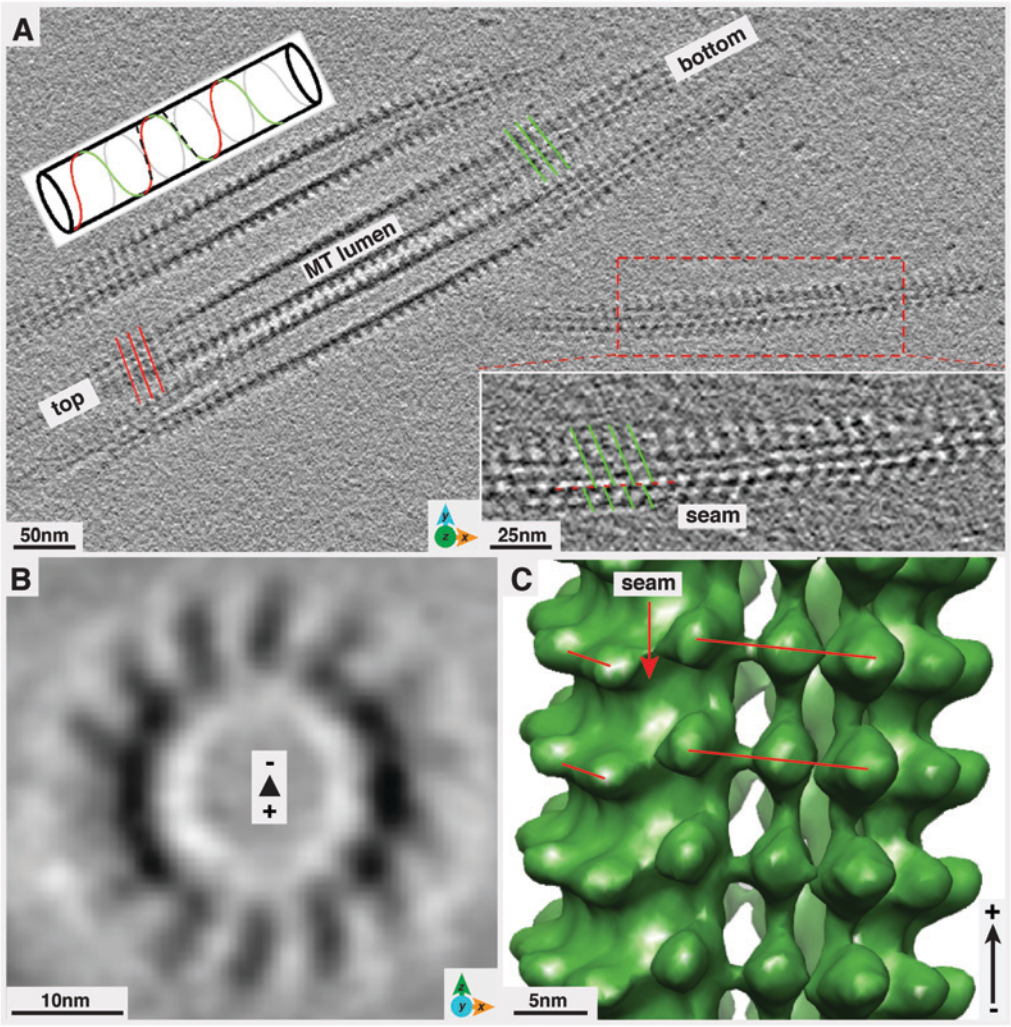

Figure 4-2: Cryo-ET of MTs decorated with Eg5 monomers permits visualization of the MT seam. (A) A 4.5 nm slice from a tomogram of MTs decorated with monomeric Eg5 motors. MTs that are slightly tilted to the image plane expose a sequence of their top, lumen and bottom regions as they cut through the slice. The B-lattice pattern emphasized by the motor decoration shows a different angle along the Bessel -2 helix according to the sketch. Since this is a left-handed helix, red lines show the angular orientation of the helical path according to the top view (towards the reader), while the green lines indicate the course of the helix at the bottom of the MT. Occasionally a lattice seam, typical for non-helical MTs with B-lattices, can be seen directly. The inset magnifies the framed area and reveals a bottom view of the seam, here made visible by the motor decoration. The seam is visible due to the shift of one protofilament by 4 nm in the axial direction relative to the other (interruptions in green lines). **(B)** Cross-section through a 9 nm projection of a subvolume average obtained using PEET, combining 218 subvolumes selected from a single MT. This MT is composed of 14 protofilaments, which can be identified despite the obvious loss of resolution along the *Z*-axis due to anisotropy caused by the missing wedge of data. **(C)** The surface rendering of the average shows the helical path of the MT as well as the lattice seam typical for a 14-protofilament MT.

The visualization of this shift is possible due to the presence of the Eg5 motor domains that specifically mark β-tubulin, and are thus staggered every 4 nm at the seam.

Despite the presence of the MT seam, the axial repeat along the MT remains the same, with 8 nm units that are identical to each other except for a relative rotational shift at an angle according to the MT's twist. This repeat allows for identical subvolumes to be selected, aligned to each other and averaged to increase the signal-to-noise ratio and provide a clearer look at the MT. Subvolumes, every 8 nm along the MT length were selected from a single MT in the tomogram in Figure 4-2A. Selected subvolumes were aligned and averaged using PEET. The resulting average of 218 subvolumes is shown in Figure 4-2B and C. The cross-sectional view shows this MT to have 14 protofilaments, indicating that is must possess a lattice seam (Figure 4-2B). The isosurface rendering of the average (Figure 4-2C) shows the presence of the seam as indicated by the break in the helical symmetry of the lattice. These results demonstrate how cryo-ET, both with and without subvolume averaging can be used to obtain structural information about the MT seam that would not be possible by traditional 2D imaging or 2D image averaging based methods that apply helical symmetry.

Cryo-ET and subvolume averaging can be used to obtain a 3D view of Kar3Vik1's cooperative binding to MTs

MTs fully and partially decorated with Kar3Vik1 were examined using cryo-ET (Figure 4-3A). Tomographic slices through the top, center, and bottom of a partially decorated MT confirm that it is only the bottom of the MT that is completely decorated by the motor, while the top of the MT has only naked protofilaments (Figure 4-3B). Interestingly, a further benefit of

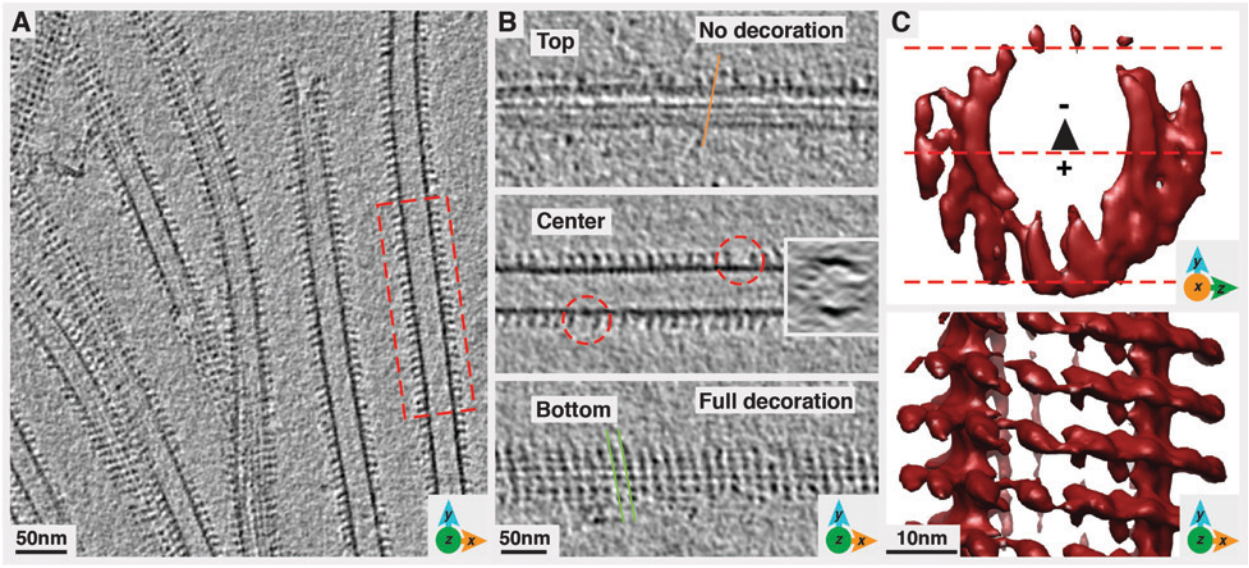

Figure 4-3: Dissection of MTs partially decorated with Kar3Vik1 by cryo-ET. (A) A 9 nm slice through a tomogram of MTs decorated with Kar3Vik1 heterodimers shows that Kar3Vik1 decorates MTs in a cooperative fashion leaving empty protofilaments besides fully decorated areas. **(B)** Three individual 4.5 nm sections through the top, center, and bottom of the tomogram of the MT boxed in **A**.The inset in the center panel shows an end-on view of the MT. While the bottom region shows strong striations every 8 nm corresponding to a fully motor-decorated surface (green lines) the top region reveals empty protofilaments running axially. A striking advantage of tomographic reconstruction is observed in the center panel in that small isolated events such as individual missing motors (red circles) are revealed with much better clarity than in 2D projections. These types of events are lost after helical averaging due to the symmetry constraints. **(C)** An isosurface representation from a PEET average of 146 particles selected from the MT in **B** gives a 3D view of how the top of the MT is free of motor decoration while the bottom and sides of the MT are completely decorated by Kar3Vik1.

cryo-ET is illustrated here by being able to see some spaces in the longitudinal section view of the MT where individual motors are missing (Figure 4-3B, center). These small events are not readily seen in 2D projections and get averaged out during helical reconstruction (as they do also with subvolume averaging).

The lack of helical symmetry and strong cooperativity of Kar3Vik1's partial decoration made it an excellent candidate for testing the PEET software. Subvolumes every 8 nm along a partially decorated MT were extracted from the tomogram in Figure 4-3A and averaged using PEET. Figure 4-3C shows the isosurface rendering of an average of 146 subvolumes. The average shows that PEET could successfully align the selected subvolumes for a higher resolution 3D view of a cooperatively decorated MT. Unfortunately, the average suffers from strong missing wedge effects that prevent us from obtaining any insight into the structural basis of Kar3Vik1's cooperative binding behavior.

Cryo-ET and subvolume averaging can be used to study complexes that form 'bridges' between adjacent filaments

While studying Kar3Vik1-MT complexes at low ratios of motor to motor-binding sites on tubulin, I noticed many instances where motors would bind preferentially between two adjacent MTs. The tomographic reconstruction of Kar3Vik1-decorated MTs in Figure 4-4A shows an example of two MTs lying parallel in the same image plane with Kar3Vik1 heterodimers extending towards each other between the two MTs. For averaging with PEET, multiple models were tested for extracting subvolumes of various sizes. The best results were obtained by extracting subvolumes that contained only the 'bridging' motors and very little of the adjacent

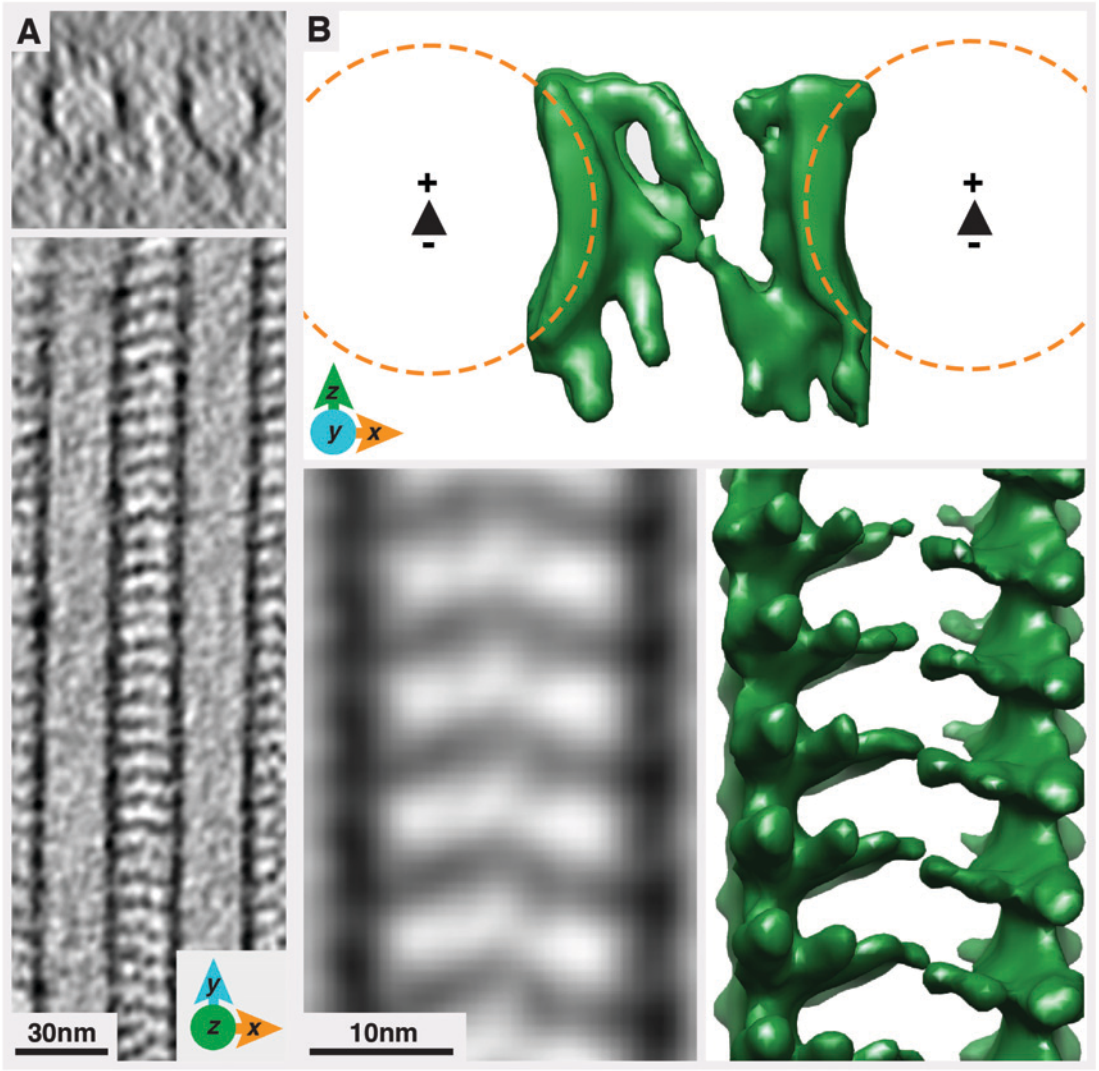

Figure 4-4: Cryo-ET of Kar3Vik1 'bridges' between adjacent MTs. (A) 18 nm *X-Z* (top) and *X-Y* (bottom) slices through a tomogram showing the cross section through two adjacent MTs (top) and the Kar3Vik1 motors extending toward each other between the two MTs (bottom). **(B)** An 18 nm projection and surface rendering of an average obtained with PEET using 44 subvolumes selected from the tomogram in **A**. The 'bridging' motors appear to bend towards each other in a manner different from the regular radially extending conformations shown in Figures 4-3 and 4-5. Since this is a highly artificial *in vitro* situation, the biological significance of these 'bridging' motors is not clear. Rather, this exemplifies the way cryo-ET and subvolume averaging can be used to analyze structural details that would not be possible by other averaging methods.

MTs. Only 44 subvolumes could be selected for averaging. Views of the resulting average are shown in Figure 4-4B. From the average it is not clear whether the motors are actually touching each other, but it appears as though they extend toward each other in a way that is different from their usual radial conformation shown in Figures 4-3 and 4-5. It is possible that this difference arises from averaging subvolumes that are actually not precisely identical, which would occur if the adjacent MTs each had a different angular twist arising from having different numbers of protofilaments. Regardless, these results exemplify the way that cryo-ET and PEET can be used to analyze bridge-like structures that would not be possible by other averaging methods.

Rotational averaging of helical structures effectively abolishes missing wedge effects

To be able to compare the results of subvolume averaging with those of helical reconstruction, I analyzed MTs fully decorated with Kar3Vik1 by cryo-ET. Subvolumes every 8 nm along the length of the MT shown in Figure 4-5A were modeled and extracted for alignment and averaging with PEET. Various views from the initial PEET run, an average of 99 subvolumes, is shown in Figure 4-5B-E. A longitudinal section through the averaged MT in the *X*-*Y* image plane shows well-defined densities corresponding to the subunits of α- and β-tubulin as well as the globular domains of Kar3 and Vik1 extending from the MT (Figure 4-5C). Conversely, a longitudinal section through the same location in the average, but instead in the *Y*-*Z* image plane illustrates the devastating effects of the missing wedge (Figure 4-5D) where image information along the *Z*-axis is smeared out, and the tubulin subunits and Kar3 and Vik1 domains cannot be resolved.

The cross-sectional slice through the average in Figure 4-5E reveals this MT to have 16 protofilaments. As for most 16-protofilament MTs, this MT lacks a lattice seam and thus forms a

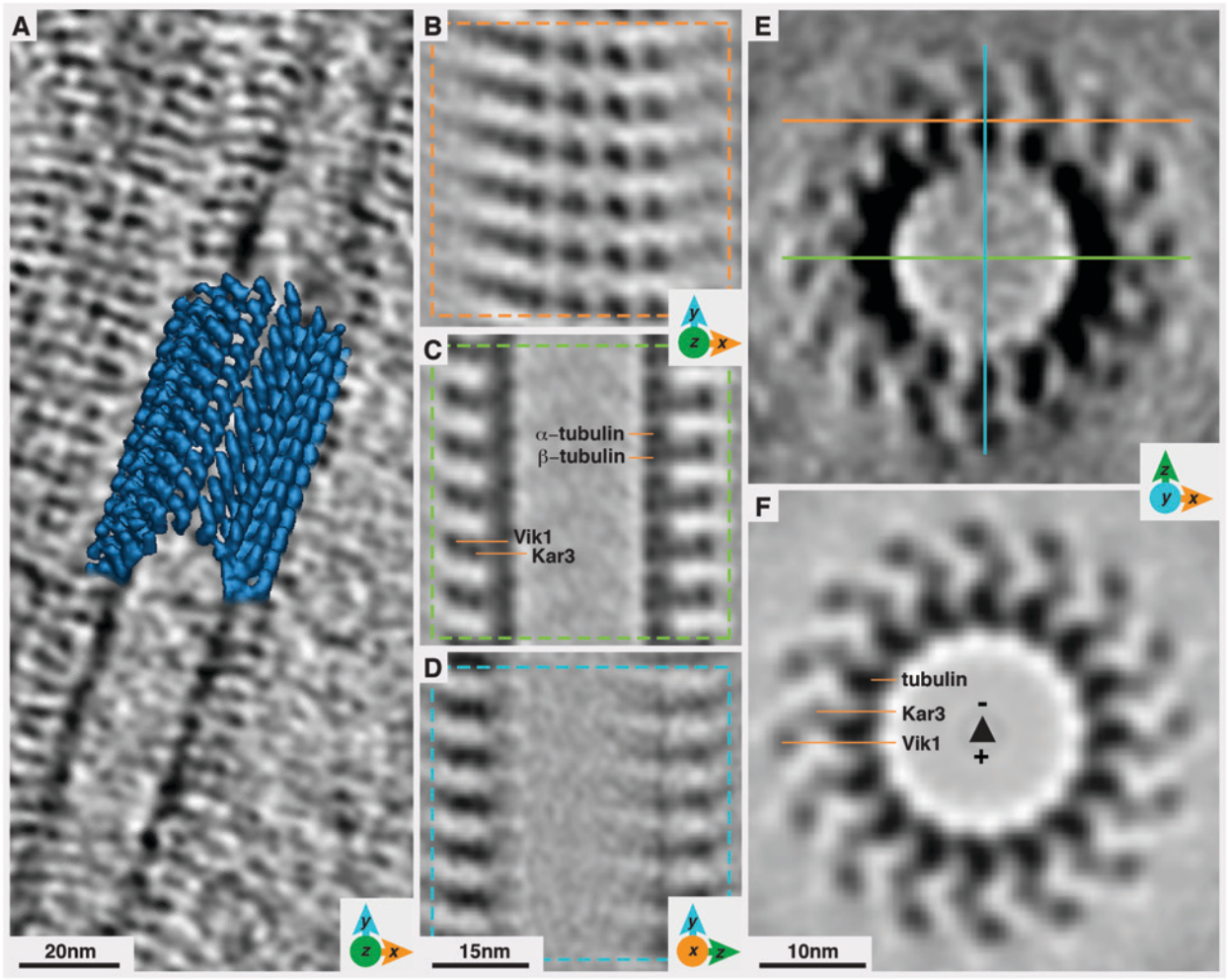

Figure 4-5: Cryo-ET and subvolume averaging of a helical MT fully decorated by Kar3Vik1. (A) A 3 nm thick tomographic *X-Y* slice of a MT decorated with Kar3Vik1 overlaid with the averaged volume shown in **B-E (**and Figure 4-6A and B). **(B-D)** 4 nm *X-Y* slices through the top and center of an average of 99 particles selected from the tomogram in **A** according to the planes indicated in **E**. The longitudinal *X-Y* slice **(C)** through the MT clearly shows densities corresponding to the α- and β-tubulin subunits and to the two globular domains of Kar3 and Vik1 extending out from the MT. Conversely, the longitudinal *Y-Z* slice in **D** cuts along the missing wedge, noticeable as reduced resolution compared to the *X-Y* slice in **C**. **(E & F)** Cross-sectional view of the 3-D map before **(E)** and after rotational averaging over all protofilaments **(F)**. The rotationally averaged map now looks indistinguishable from a helical reconstruction map at the same resolution. While the missing wedge effects are clearly visible before rotational averaging as the strong densities and smearing out along the *Z*-axis, rotational averaging eliminates the missing wedge completely.

perfect helix. The helical symmetry is such that the repeating unit (a single αβ-tubulin subunit complexed with a Kar3Vik1 heterodimer) is projected at all orientations around the helical axis. I applied rotational averaging to determine whether PEET could be used to eliminate missing wedge effects by averaging around the helical axis, instead of only along the length of the MT. The asymmetric unit for the average shown in Figure 4-5B-E is an 8 nm segment along the MT axis. With rotational averaging, the asymmetric unit is an 8 nm segment along a single protofilament. Thus, the number of theoretical subvolumes obtained by rotationally averaging this dataset is 16 x more than that obtained by averaging along the MT length.

A cross section through the average obtained after rotational averaging using PEET is shown in Figures 4-5F and 4-6D and a view along the averaged MT axis is shown in Figure 4-6E. When compared to the PEET average before rotational averaging (Figures 4-5E, 4-6A and 4-6B), a significant improvement can be seen. Prior to rotational averaging, strong missing wedge effects limit the resolution along the *Z*-axis. After rotational averaging the effects of the missing wedge have been completely eliminated and the average is comparable to one obtained from a helical reconstruction, with equal resolution along all axes. Furthermore, the large increase in the number of particles included in the rotationally averaged dataset results in a higher signal-to-noise ratio with subsequent improvements in resolution.

To quantify the resolution improvement, FSC calculatations were used (Figure 4-6C and F) (Harauz and van Heel 1986). Based on the resolution corresponding to a correlation of 0.5 (the 50% correlation criterion), the average prior to rotational averaging shows a resolution of 3.8 nm (Figure 4-6C) which is improved to 3.2 nm for the average after rotational averaging has been applied (Figure 4-6F). These results illustrate that taking advantage of symmetry

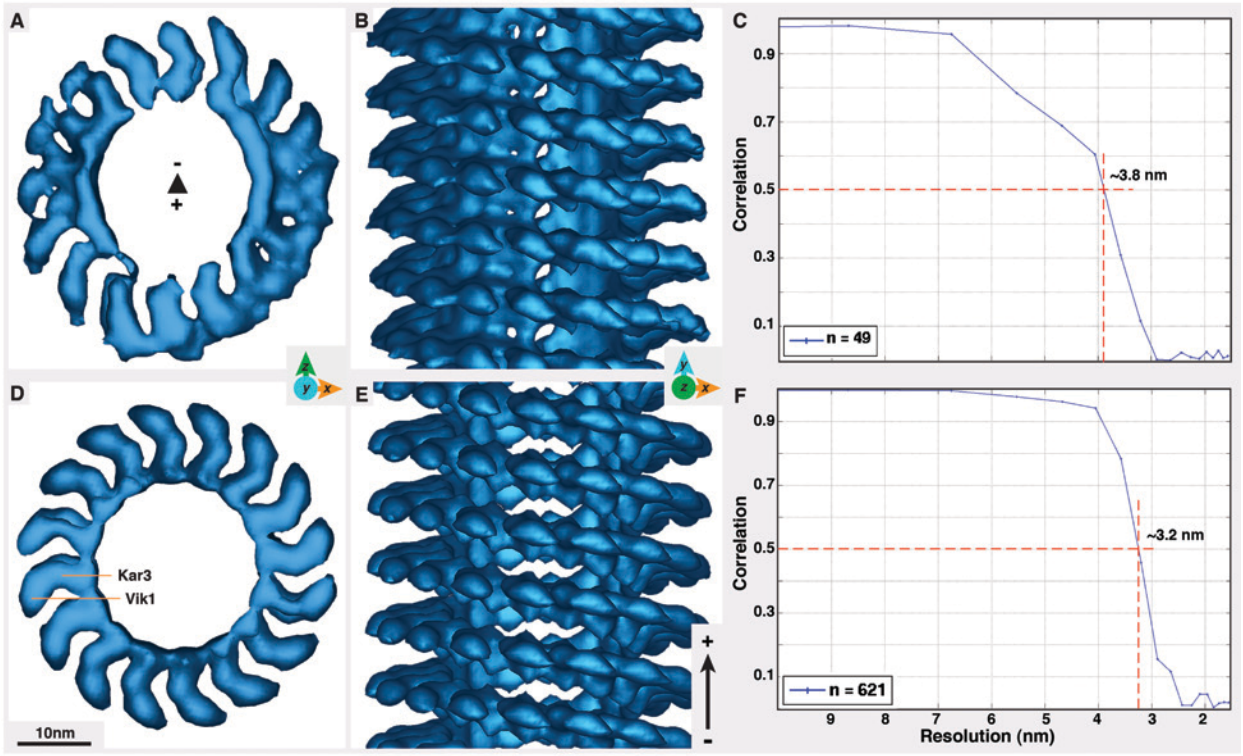

Figure 4-6: **Rotational averaging around the MT axis effectively eliminates the missing wedge. (A & B)** Surface renderings of the averaged 3D map shown in Figure 4A-E. The cross-section reveals the number of protofilaments of this MT to be 16, which produces a perfectly helical MT without seams as shown in **B**. **(D & E)** Surface rendered 3D map after rotational averaging of the map in **A** (also shown in Figure 4-5F) showing that the effects of the missing wedge have been eliminated. By rotationally averaging over all 16 protofilaments the asymmetric unit changes from 8 nm axial slices along the MT axis to one αβ-tubulin–motor domain complex. Hence, the theoretical maximum number of asymmetric units included in the average is increased from 99 to 1584 (16 x 99). However, our average is based on the 1242 particles with the best correlation to the reference because this subset gave the highest resolution. **(C & F)** For FSC calculations, the datasets were split in half on a random basis and the two halves were correlated against each other. FSC graphs obtained from the maps in **A** (**C**) and **D** (**F**) reveal resolution limits of 3.8 nm and 3.2 nm respectively based on the 50% correlation criterion.

parameters in the data can effectively eliminate missing wedge artifacts and significantly increase the signal-to-noise ratio for a corresponding improvement in resolution.

Discussion

Here I have used both the non-helical and helical MT-binding patterns of Eg5 monomers and Kar3Vik1 dimers to demonstrate the power of cryo-ET especially when combined with subvolume averaging. Traditionally, motor-decorated MTs have been studied using helical reconstruction (see Chapter 3). Helical reconstruction has the benefit of being able to rapidly incorporate very large numbers of asymmetric units for averaging and, because of the helical symmetry, isotropic resolution can be achieved. The raw data for helical averaging are obtained from single 2D projections so the electron dose that can be applied to each image is much higher than that for tilt series acquisition and consequently the signal-to-noise ratio is already higher in the raw data than it is in tomograms.

A major drawback of helical reconstruction (and other 2D-image averaging procedures) is that small isolated events cannot be observed as they get averaged out during image processing. Here I have shown a benefit of cryo-ET in that events such as missing motors can be visualized with much better clarity than in 2D-projections.

Another disadvantage of helical reconstruction is that a perfect helix is required, and thus there are many situations where it cannot be used, notably, on the majority of MTs that possess a lattice seam that interrupts the helical symmetry. But there are applications when it is desirable to retain the information of the MT seam. For example, Mal3, the EB1 homolog in *S. pombe*, has been observed to bind exclusively to the MT seam (Sandblad et al. 2006), a result that was only

obtained by unidirectional heavy metal shadowing of the MT surface. Furthermore, the majority of MTs *in vivo* are comprised of 13 protofilaments and all contain seams (Tilney et al., 1973; McIntosh et al., 2009). This may be important for specific binding of other proteins with direct consequences on their function.

Using subvolume averaging as a means to observe Kar3Vik1's cooperative binding pattern has provided results showing that this method could potentially be a way to study the basis of cooperative decoration by molecular motors such as Kar3Vik1 and Ncd (Wendt et al., 2002). The big hurdle here is that many subvolumes would need to be selected from multiple MTs at various orientations in several tomograms to fill in the information lost to the missing wedge and increase the signal-to-noise ratio enough to be able to note potentially subtle changes in tubulin. All subvolumes included in the final average would have to be obtained from MTs with the identical number of protofilaments and have the same number of protofilaments that are decorated and undecorated. Given that it is difficult (if not impossible) to control how many protofilaments of a single MT would contain motors, this would be an extremely laborious method to tackle this interesting question.

I have shown here that subvolume averaging can be a useful tool to study complexes that form bridges in between MTs or other filaments in greater structural detail. For example, the human MAP65 protein PRC1 that forms ordered crosslinks between antiparallel MTs (Subramanian et al., 2010). In our lab, researchers are using subvolume averaging in attempts to visualize the connections in between the MTs of the subpellicular MT array of *Trypanosoma*

brucei as a means of determining how the MTs are able to maintain the slender shape of the cell (J. Höög and C. Bouchet-Marquis).

Finally, I have shown how rotational averaging around the MT axis can be used successfully to remove missing wedge effects from subvolume averages and considerably increase the signal-to-noise ratio to improve resolution. This averaging technique can be applied to any structure that possesses an axis of symmetry, such as icosahedral virus particles (Xiong et al., 2009; Cope et al., 2011), helical filaments, or square or hexagonal planar arrays. It was some of this work that led to the PEET developers writing additional programs and providing new features in the graphic user interface to facilitate the incorporation of symmetry into subvolume averaging in a way that is more intuitive, less time-consuming and less prone to error than the methods that were used here.

Chapter 5. Metal-precipitating peptides and their potential as clonable labels for site-specific identification of proteins in the electron microscope

Introduction

The need for a clonable label for protein identification by EM

EM is a powerful tool for studying isolated macromolecular complexes, as well as examining the structure and organization of important components within cells. However, due to similarities in their shape and electron density most protein complexes cannot be readily identified within cells and indeed even the arrangement of individual proteins within a purified complex is not readily determined (see Chapter 3). It is thus highly desirable to have clonable tags that can be used for site-specific identification of proteins by EM, analogous to the array of colorful fluorescent labels currently used to identify and localize proteins by light microscopy.

The aim of the work presented here was to develop a short known metal-binding peptide into a clonable tag for use in EM. The sequence encoding the peptide tag could be cloned onto the gene for a protein of interest. In theory, when the tagged protein is incubated in an aqueous metal salt solution, the peptide would facilitate precipitation of small electron dense nanoparticles that remain tightly bound to the peptide (Figure 5-1A). The protein of interest could then be identified by visualizing the nanoparticles in the EM. While we chose to develop a single metal-precipitating peptide utilizing a few simple *in vitro* test systems (described below), the ultimate goal is to exploit a number of peptides that precipitate different electron dense materials to simultaneously identify multiple protein complexes within cells by EM.

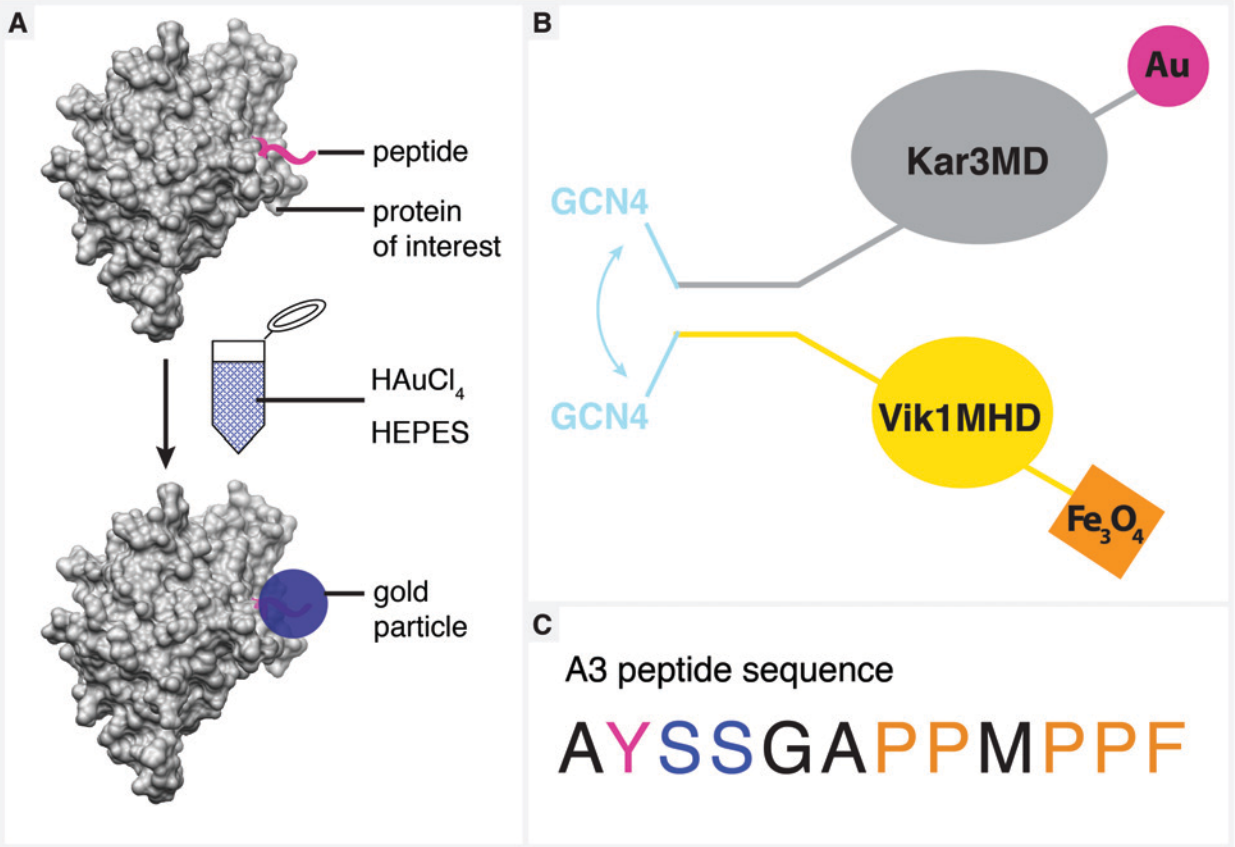

Figure 5-1: Nanoparticle-precipitating peptides for site-specific identification of proteins in the EM (A) A cartoon illustrating the ideal scenario of expressing a short peptide sequence onto the end of a protein such as the Kar3 head domain shown here (PDB accession: 3KAR, Gulick et al., 1998). Upon incubation with a metal salt solution and a reducing agent, the peptide would precipitate nanoparticles that can be visualized by EM, providing a means of identifying the protein. **(B)** Kar3Vik1 is an ideal specimen for testing two different particle-precipitating peptides. For example, by tagging Kar3 with a gold-precipitating peptide, and Vik1 with an iron oxide precipitating peptide, we could test the ability to distinguish between Kar3 and Vik1 based on differences in the size, shape, electron density or electron energy loss spectra of the two types of precipitated nanoparticles. **(C)** The amino acid sequence of the A3 peptide that is able to bind to gold and modulate the precipitation of gold particles with the help of a reducing agent such as HEPES (Slocik et al., 2005). The role of the amino acids in particle formation is not well understood (Diamanti et al., 2009). Serine (blue) is known to be able to bind metal salts and stabilize gold particles, and hydrophobic residues such as proline and phenylalanine (orange) often appear in gold-binding sequences. Though tyrosine (pink) is widely known to reduce gold salts, in A3 it reportedly has only a minimal reducing role (Diamanti et al., 2009).

Current labeling techniques for EM have drawbacks

The work described in Chapter 3 shows how identification of a protein in the EM can be performed using a small gold particle with a maleimide functional group that can be linked directly to a cysteine residue. While useful, the disadvantage of this technique is that it requires that the protein have only one exposed cysteine residue and the creation of a cysteine-light mutant can be an extremely time-consuming (or impossible) process as cysteine replacements may have detrimental effects on protein folding. Furthermore, labeling-efficiency by this method is generally only between 60-80%. This labeling method also cannot be applied to localize proteins within cells.

Cloning an additional protein domain onto a protein of interest for specific localization has also been reported. SH3 domains have been used to identify the precise location of the neck in Ncd (Wendt et al., 2002), and the position of the neck-linker in kinesin-1 (Skiniotis et al., 2003) with great success. The drawback here is that the location of such a small additional protein density can only be achieved when the EM imaging is combined with an averaging technique, such as helical reconstruction and subsequent difference mapping to show significant differences between electron density maps of the protein both with and without the additional domain. This method is thus labor intensive and not applicable to structures that do not possess symmetry.

Immunogold labeling is a technique used routinely to localize protein complexes within resin-embedded cells by EM. The embedded cells are sectioned and treated with a primary antibody to the protein of interest, followed by a secondary antibody complexed to a gold colloid 5-10 nm in diameter. A shortcoming of immunogold labeling is that only antigens present at the surfaces of the sections are accessible to the antibodies. The gold label also localizes relatively far away from the actual protein being labeled, especially if both a primary and secondary

antibody are used. Furthermore, immunogold labeling cannot be carried out on cryosections so is never combined with the improved structural preservation of unstained, frozen-hydrated material.

Small metal-precipitating peptides are promising candidates for use as a clonable label

For some time, chemists have been interested in discovering small peptides that are able to bind to specific metals and modulate the formation of metal particles. These studies are of interest for developing the controlled synthesis of metal structures (and other inorganic materials) using benign conditions for a wide array of applications in electronics and optics (Dickerson et al., 2008). Experiments screening for peptides that could bind gold were first conducted by Brown (1997). This was followed by work showing that in addition to binding gold, the identified peptides also influenced the nucleation rate and morphology of synthesized gold particles (Brown et al., 2000). Since then, numerous peptides involved in inorganic materials synthesis have been discovered, such as those that can mediate formation of silver, titanium dioxide and germanium dioxide, among others (reviewed in Dickerson et al., 2008).

The most common technique used to identify metal-binding peptides is screening of phage-display libraries against a target material by a process known as 'biopanning' (Kriplani and Kay, 2005). The A3 peptide, used in this chapter, with the amino acid sequence AYSSGAPPMPPF (Figure 5-1C), was first selected from a combinatorial phage-display library for its ability to bind to silver particles (Naik et al., 2002). A3 was later shown to be able to bind to gold surfaces and also mediate the precipitation of gold nanoparticles from an aqueous solution of chloroauric acid ($HAuCl_4$) (Slocik et al., 2005). In these experiments, HEPES was used as a buffer and its role in the gold-precipitating reaction was not recognized. Later, the unexpected reducing properties of

HEPES and its ability to rapidly precipitate polydisperse gold nanoparticles (in the absence of the A3 peptide) from $NaAuCl_4$ and $HAuCl_4$ were described (Habib et al., 2005; Xie et al., 2007). An investigation into the relative roles that A3 and HEPES might play in gold particle precipitation was carried out by Diamanti et al. (2009). They reported that in a nonreducing buffer, A3 mediates precipitation of gold particles very slowly (> 4 days). Conversely, in the presence of a reducing buffer such as HEPES, A3 serves to slow down particle nucleation and control the concentration of free Au(0) in the solution. The presence of A3 thus results in the formation of smaller, monodisperse gold nanoparticles as opposed to the large gold aggregates of various shapes and sizes formed by HEPES and $HAuCl_4$ in the absence of A3.

A3 is an attractive choice for use as a clonable label for EM. Gold nanoparticles are very electron dense and thus easy to see in the EM. With only 12 amino acids, it is unlikely that the peptide will interfere with protein folding or dramatically change the structure of the protein of interest. Furthermore, in the presence of HEPES, A3 has been shown to form particles of uniform size and shape that appear to remain bound to the peptide (Slocik et al., 2005; Chen et al., 2008; Diamanti et al., 2009).

Selection of test specimens for developing a single peptide as a clonable label

For the work in this chapter three test specimens were used: 1) the monomeric motor head domain of the kinesin-5 Eg5, 2) the intermediate filament vimentin, and 3) the major capsid protein of polyomavirus, VP1.

Monomeric Eg5 was chosen because the methods to study Eg5 bound to MTs *in vitro* are well-established and experimental reagents were readily available. The structure of Eg5-MT complexes is also well documented (Krzysiak et al., 2006; Bodey et al., 2009) and it thus

provides a good system to develop experimental conditions for proof-of-principle results. Furthermore, Eg5-MT complexes are amenable to a number of image averaging techniques such as helical reconstruction and subvolume averaging (see Chapters 3 and 4) that can be used to obtain 3D maps, should it prove difficult to identify particles directly in 2D projections.

Vimentin was also selected as a test specimen because the purification and EM imaging techniques were well-established (Kirmse et al., 2010). Upon incubation at 37°C, vimentin assembles into long filaments. The configuration of vimentin subunits in the elongated filament is not known, but it is likely that the configuration would place multiple peptide tags in close proximity that could aid in the formation of gold nanoparticles (Figure 5-2B) (Sokolova et al., 2006). It was also hoped that if we could develop the peptides as reliable labels, that others could use them to gain structural insight into how vimentin assembles by analyzing the locations of and distances between gold particles.

VP1 was chosen as a test sample due to problems that arose from working with Eg5-MT complexes. The MTs were very sensitive to the gold precursor and HEPES buffer and obtaining complete binding of Eg5 to MTs introduced an additional variable into the experiments. Furthermore, Eg5 could not be purified in high yields despite numerous attempts by myself and other lab members. As VP1 self-assembles into pentamers (Salunke et al., 1986) and could be purified in large quantities, it provided a simpler setup on which to conduct proof-of-principle experiments.

Kar3Vik1 is an ideal specimen for developing multiple peptides as clonable labels

Kar3Vik1's heterodimeric configuration (Chapters 2 and 3) makes it an ideal candidate for testing of two peptides that each precipitates a different metal or metal oxide. For example, a

gold-precipitating peptide sequence could be cloned onto the Kar3 gene and an iron oxide-precipitating peptide sequence onto the Vik1 gene (Figure 5-1B). This experimental setup would enable us to attempt conditions that allow for identification of two proteins within the same complex. Ideally, identification would be possible based on the differences in size, shape, electron density or electron energy loss spectra (EELS) of the two different metals or metal oxides precipitated by the two peptides. Kar3Vik1's asymmetric MT-binding configuration is also beneficial here because the precipitated particles would likely be spaced at a reasonable distance apart from each other and Kar3Vik1's highly cooperative binding behavior could allow for optimal side views of the motors bound to MTs without obstruction from motors on adjacent protofilaments (as shown in Figure 2-3C).

This project was a close collaboration with the lab of Dr Daniel Feldheim in the Department of Chemistry and Biochemistry at The University of Colorado at Boulder and the majority of the experiments described here were performed side-by-side with Carly Jo Carter, a graduate student in the Feldheim lab. The work presented here also relied on Maria Pagratis (Hoenger lab) who carried out all of the cloning, expression and purification of the A3-tagged proteins.

Materials and Methods

Cloning, expression and purification of A3-tagged proteins

A sequence encoding the 12 amino acids of A3, AYSSGAPPMPPF, was cloned onto the genes of 3 different test specimens:

Eg5-A3 consists of residues Met^{1}-Gln^{367} of the human Eg5 kinesin motor domain and has the A3 sequence at the C-terminus (Figure 5-2A). Purification of Eg5-A3 was carried out similarly to methods reported by Cochran et al. (2004).

Vimentin-A3 is a full-length human vimentin construct with A3 at the N-terminus (Figure 5-3B). Vimentin-A3 was expressed and purified as described previously (Herrmann et al., 1996)

VP1-A3 is the sequence of the polyomavirus major capsid protein VP1, with A3 at the C-terminus (Figure 5-3C). Purified VP1 for use as a control was obtained from Kim Erickson in the lab of Bob Garcea who also provided advice on working with VP1 for EM.

All cloning, expression and purification was performed by Maria Pagratis with the help of Cynthia Page and Robert Kirmse (WT vimentin and vimentin-A3) and advice from Susan Gilbert (Eg5) and Kim Erickson (VP1) and thus is not described here in any detail.

Particle formation by A3-tagged proteins and preparation of EM

A 'trial and error' approach was taken to determine the conditions that would result in formation of uniformly small (2-4 nm in diameter) gold particles specifically localized at the A3 tag and where minimal background particles would form in control samples under similar conditions. The general methods used for sample preparation are described here. The specific concentrations of $HAuCl_4$ and HEPES and incubation times that gave the best results are described in the 'Results' section and the figure legends.

Eg5-A3

Eg5-A3-MT complexes were prepared in the presence of AMP-PNP as described in Chapter 4. For 'on grid' experiments, Eg5-A3-MT complexes were adsorbed to either carbon-coated copper

grids (negative stain) or C-flat holey carbon grids (cryo) for 35-60 s and excess solution was blotted away. The grids were then inverted onto a droplet of $HAuCl_4$ and HEPES at the desired concentration for the planned incubation time. To minimize reduction of $HAuCl_4$ by HEPES in the absence of the peptide, $HAuCl_4$ was added to a droplet of HEPES after inverting the grid onto the droplet. Excess liquid was again blotted away and samples were stained immediately with NanoVan® (negative stain) or rapidly plunged into liquid ethane (cryo), as described in Chapter 2. These experiments were problematic because the MTs were severely degraded by incubation with the $HAuCl_4$ and HEPES. To overcome this, we also prepared 'in solution' experiments where Eg5-A3 was incubated with the desired concentrations of $HAuCl_4$ and HEPES for the appropriate incubation time and then added to MTs already adsorbed to a grid. To avoid rapid reduction of $HAuCl_4$ by HEPES in the absence of A3, Eg5-A3 was added to HEPES first and then $HAuCl_4$ was added immediately afterwards. The Eg5-A3 was allowed to bind to MTs for ~30 s before blotting away excess fluid for staining or freezing. These experiments were much more successful as Eg5-A3 was still able to bind to the MTs which retained their structural integrity.

Control experiments were performed using MTs only, WT Eg5 incubated in identical concentrations of $HAuCl_4$ and HEPES, and Eg5-A3 incubated with $HAuCl_4$ only or HEPES only. Experiments with Eg5-A3 only, in the absence of MTs, were prepared similarly except that no MTs were applied to the grid, and the sample was not stained.

Vimentin-A3

Vimentin-A3 filaments were polymerized from purified tetramers in 40 mM Tris pH 7.0, 320 mM NaCl, 2 mM $MgCl_2$, for 60 min at 37°C. Polymerized filaments were adsorbed to C-flat

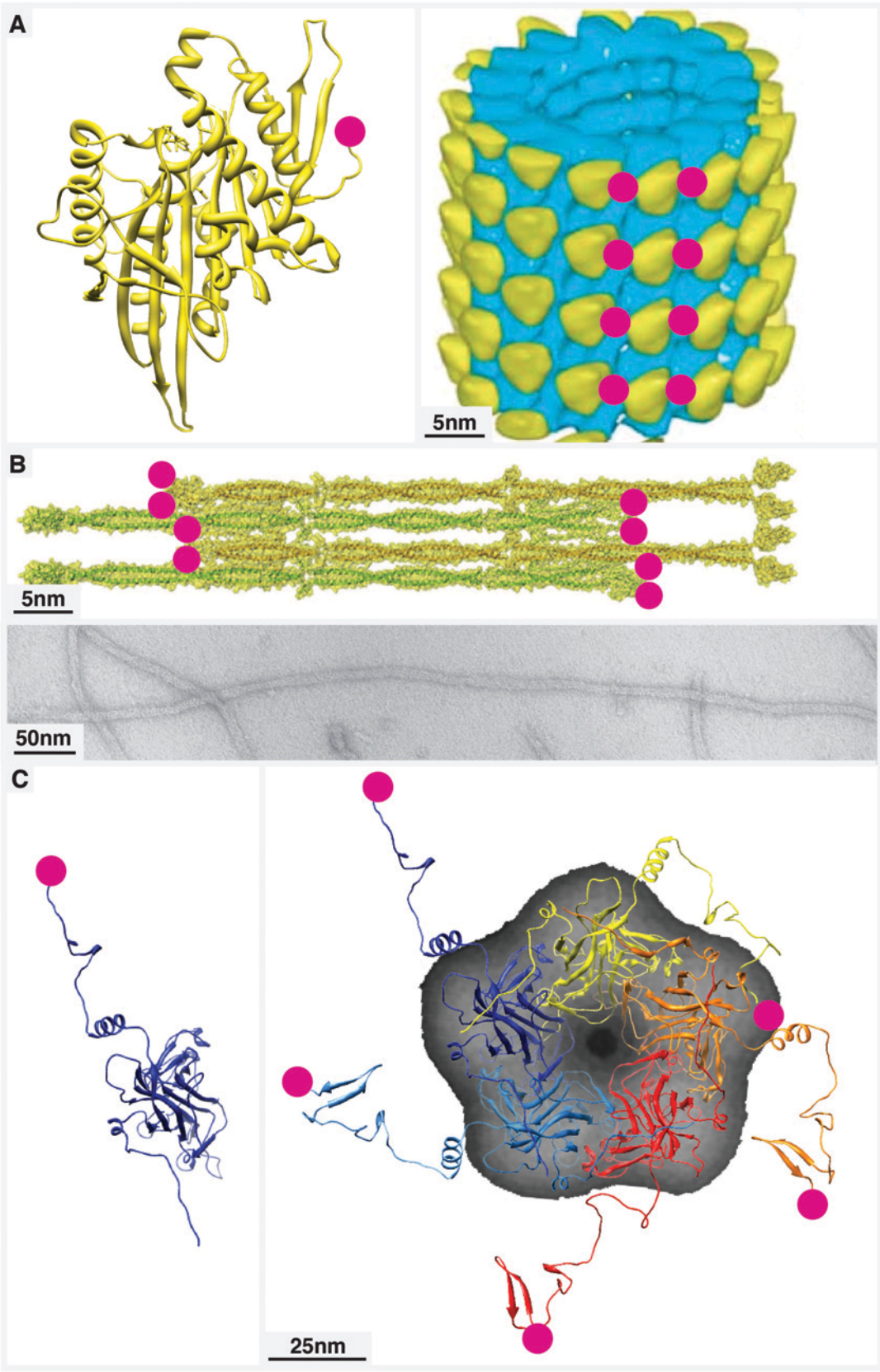
A
5nm
B
5nm
50nm
C
25nm

Figure 5-2: Cartoons showing the approximate locations of A3 peptides on test specimens. Pink dots represent A3 and are not drawn to scale. **(A)** Left: A3 was cloned as a C-terminal tag on the monomeric Eg5 motor domain (PDB accession:1II6; Turner et al., 2001). Right: The approximate location of the A3 peptide when Eg5-A3 is bound to MTs (adapted from Krzysiak et al., 2006). **(B)** Top: A3 was cloned as an N-terminal tag on vimentin. In solution, vimentin forms tetramers that associate laterally into octamers (adapted from Sokolova et al., 2006). Four octamers then assemble into unit length filaments that join longitudinally to form the mature filament in a configuration that is not yet known. Bottom: Electron micrograph of a negatively-stained mature vimentin filament. Image courtesy of Robert Kirmse, University of Colorado, Boulder. **(C)** Left: A3 was cloned as a C-terminal tag on polyomavirus VP1. Right: Individual VP1 units assemble into pentamers as shown with the VP1 X-ray crystal structure (PDB accession: 1SVA; Stehle et al., 1996) overlaid on a single-particle average obtained from negative stain EM (Salunke et al., 1986).

holey carbon grids for 35-60 s and excess solution was blotted away. The grids were then inverted onto a droplet of $HAuCl_4$ and HEPES at the desired concentration for either 2 or 5 min before blotting away excess fluid, followed by plunge-freezing. As a negative control, WT vimentin filaments were incubated with identical concentrations of $HAuCl_4$ and HEPES for the same amount of time as the vinemtin-A3 experiments.

VP1-A3

Experiments with VP1-A3 pentamers were performed by incubating VP1-A3 with various concentrations of $HAuCl_4$ and HEPES. After the designated incubation time, VP1-A3 was applied to carbon-coated copper grids for staining with NanoVan® as described for Eg5-A3 above. For control experiments, WT VP1 was prepared in the identical manner as VP1-A3.

Electron Microscopy

Negatively stained samples were imaged on a Philips CM-100 transmission EM operating at 80 kV. Nominal magnifications ranging from 5 200 - 72 000 x were used. Cryo-EM specimens were imaged on an FEI Tecnai F20 FEG transmission EM as described in Chapter 2.

Results

Eg5-A3 in solution can precipitate gold nanoparticles

The ability of Eg5-A3 to precipitate gold particles was tested by incubating 8.8 μM Eg5-A3 with 100 μM $HAuCl_4$ and 100 μM HEPES for 2 min. Small, round gold particles 2-5 nm in diameter could be visualized by EM (Figure 5-3A). As these samples were prepared in the absence of a stain, the biological material could not be seen. Thus, it was not possible to know

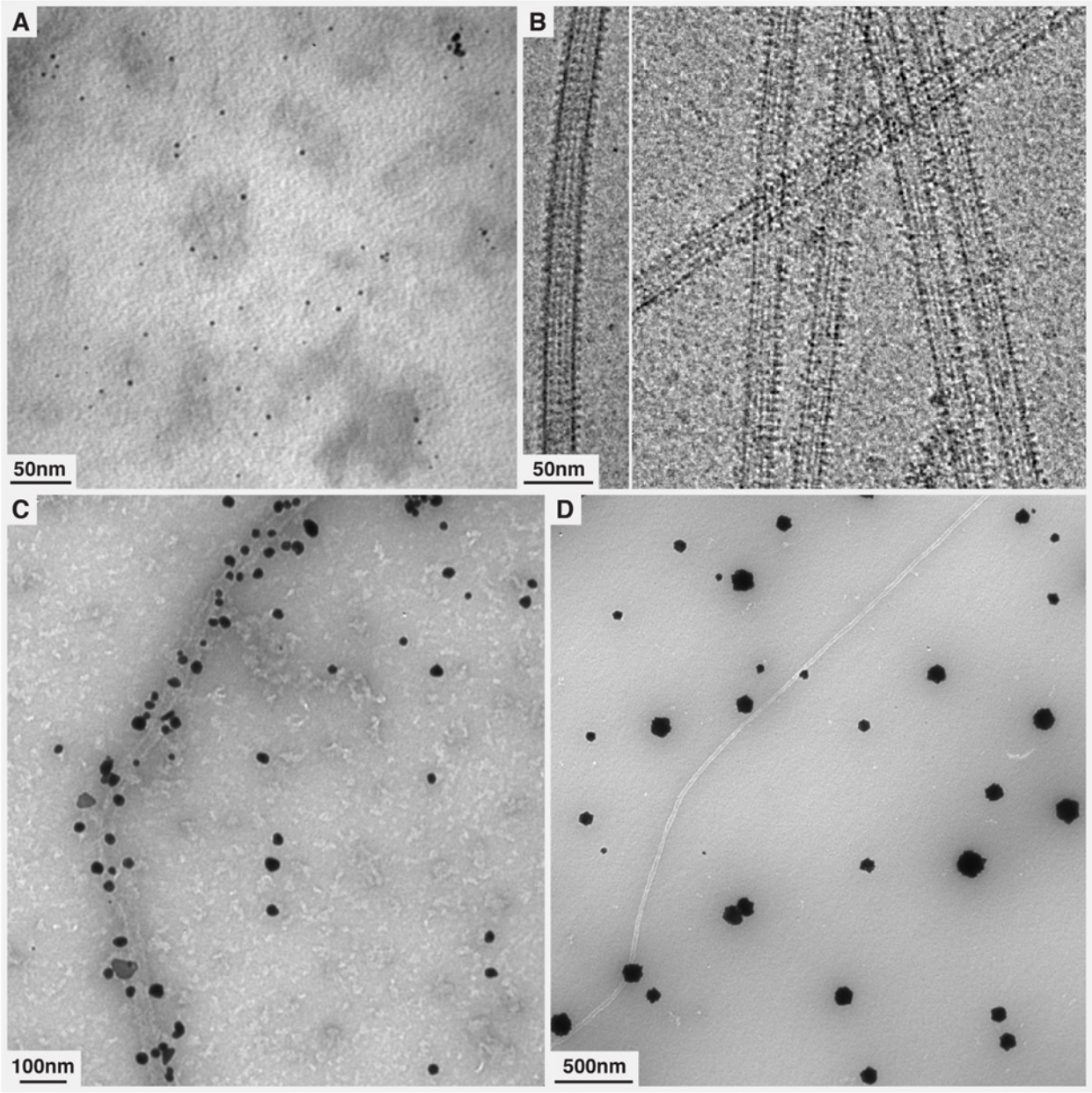

Figure 5-3: Eg5-A3 tests the usefulness of metal-precipitating peptides. (A) 8.8 μM Eg5-A3 incubated with 100 μM $HAuCl_4$ and 100 μM HEPES produces round particles that are 2-5 nm in diameter. Without complexing Eg5-A3 to MTs, we cannot know whether the particles are directly associated with a single or multiple Eg5-A3 molecules as the individual motor domains are too small to be seen. **(B)** Eg5-A3 (right) can bind to MTs in a manner akin to a WT Eg5 monomer (left) showing that the presence of the peptide does not interfere with protein folding or MT binding. **(C)** MTs decorated with Eg5-A3 and incubated with 500 μM $HAuCl_4$ and 500μM HEPES shows gold particles that cluster at the MT. (**D**) Conversely, MTs incubated with the same concentrations of $HAuCl_4$ and HEPES, but in the absence of Eg5-A3, show gold particles that do not cluster around the MT.

whether the gold particles were directly associated with Eg5-A3 and impossible to obtain an idea of how many Eg5-A3 molecules were required to precipitate each particle of this size.

MTs decorated with Eg5-A3 clusters gold particles at the MT

Eg5-A3's ability to bind to MTs was assessed by incubating Eg5-A3 with MTs and AMP-PNP. Eg5-A3 can be seen decorating MTs in a manner akin to WT Eg5 showing that the presence of A3 at the C-terminus of the motor head does not have adverse effects on the folding of the globular domain and does not interfere with Eg5's MT binding site (Figure 5-3B).

To determine whether gold particles would precipitate specifically at the location of Eg5-A3, MTs decorated with Eg5-A3 were incubated with 500 μM $HAuCl_4$ and 500 μM HEPES for 5 min. The MTs show severe structural deterioration from incubation with the gold salt solution and HEPES. However, gold particles can be seen to cluster preferentially around the MT, indicating that A3 may be able to facilitate formation of gold nanoparticles that remain bound to the peptide (Figure 5-3C).

Undecorated MTs incubated with 500 μM $HAuCl_4$ and 500 μM HEPES for 5 min were used as a control. The control sample did not appear to cluster gold particles at the MT (Figure 5-3D). Instead, large gold particles that vary in size appear in the background. This is consistent with reports that HEPES quickly reduces the Au(III) in $HAuCl_4$ to Au(0) in the absence of A3 (Habib et al., 2005; Xie et al., 2007; Diamanti et al., 2009).

Vimentin-A3 accumulates gold particles that can be seen directly on the filaments

Vimentin-A3 filaments were incubated with 100 μM $HAuCl_4$ and 100 μM HEPES for 2 min at room temperature and subsequently examined by cryo-EM. WT vimentin filaments were

prepared in the identical manner. Vimentin-A3 clearly shows the accumulation of gold nanoparticles on the filaments (Figure 5-4A). The particles vary greatly in size, and no obvious regular pattern can be seen in the distance between the particles that could be used to determine a structural repeat. Conversely, WT vimentin does not show accumulation of such gold particles in the presence of 100 μM $HAuCl_4$ and 100 μM HEPES, suggesting that A3 is influencing particle formation under these conditions (Figure 5-4B).

Polyomavirus VP1-A3 can form pentamers indistinguishable from those of WT VP1

WT VP1 self-assembles into distinctive pentamers that are easily visualized by EM (Figure 5-5A). To evaluate VP1 as a specimen for development of the A3 peptide, WT VP1 was incubated with 100 μM $HAuCl_4$ and 100 μM HEPES for 2 min. Examination of negatively stained pentamers by EM revealed that incubation of VP1 with 100 μM $HAuCl_4$ and 100 μM HEPES did not affect the pentameric structure (Figure 5-5B). Furthermore, the absence of gold particles showed that there was no non-specific gold precipitation in the absence of A3 under these conditions, verifying that VP1 is a good specimen for testing the A3 peptides.

The A3 sequence was cloned into the VP1 gene and VP1-A3 was tested for its ability to form pentamers. EM of negatively stained samples confirmed that VP1-A3 could self-assemble into pentamers indistinguishable from WT VP1 showing that the presence of A3 did not inhibit pentamer assembly (Figure 5-5C).

Subsequent experiments were performed to elucidate conditions for specific gold nanoparticle formation by VP1-A3. Promising results were obtained by incubating VP1-A3 in 100 μM $HAuCl_4$ and 50 μM HEPES for 2 min (Figure 5-5D). There appears to be some very

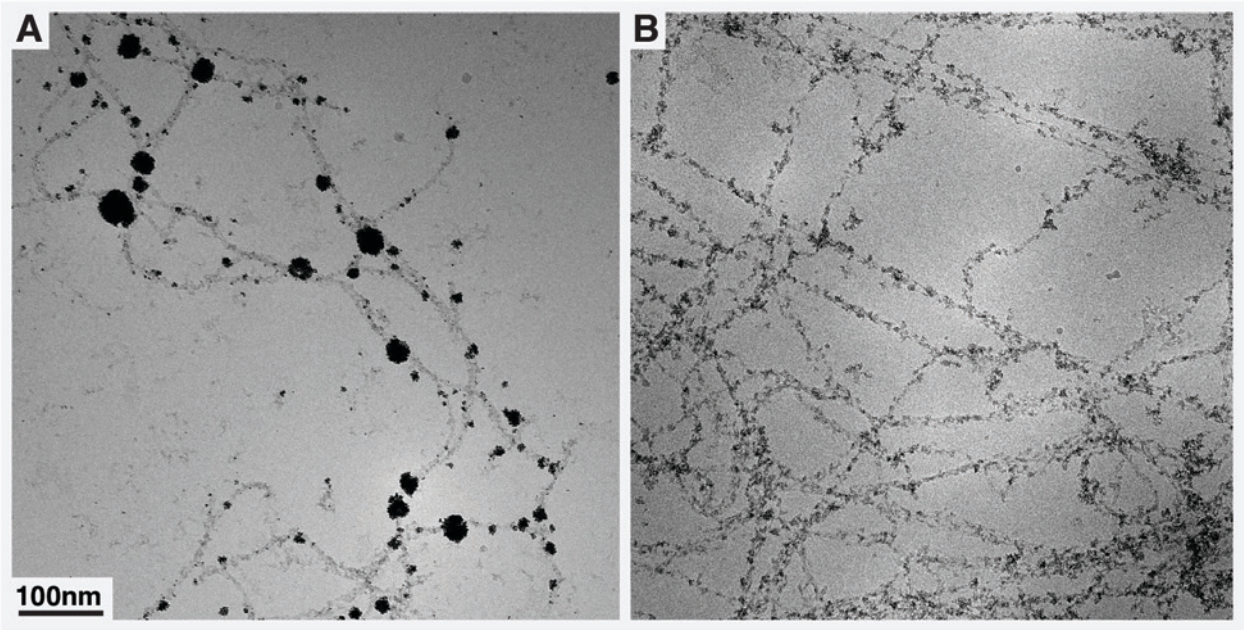

Figure 5-4: Vimentin-A3 accumulates gold particles that can be seen directly on filaments by cryo-EM. (A) Vimentin-A3 shows the accumulation of many gold particles when incubated with 100μM $HAuCl_4$ and 100μM HEPES for 2 minutes. The particles appear specifically on the filaments with few particles visible in the background. Conversely, no such particles can be seen on WT vimentin when incubated under the same conditions **(B)**.

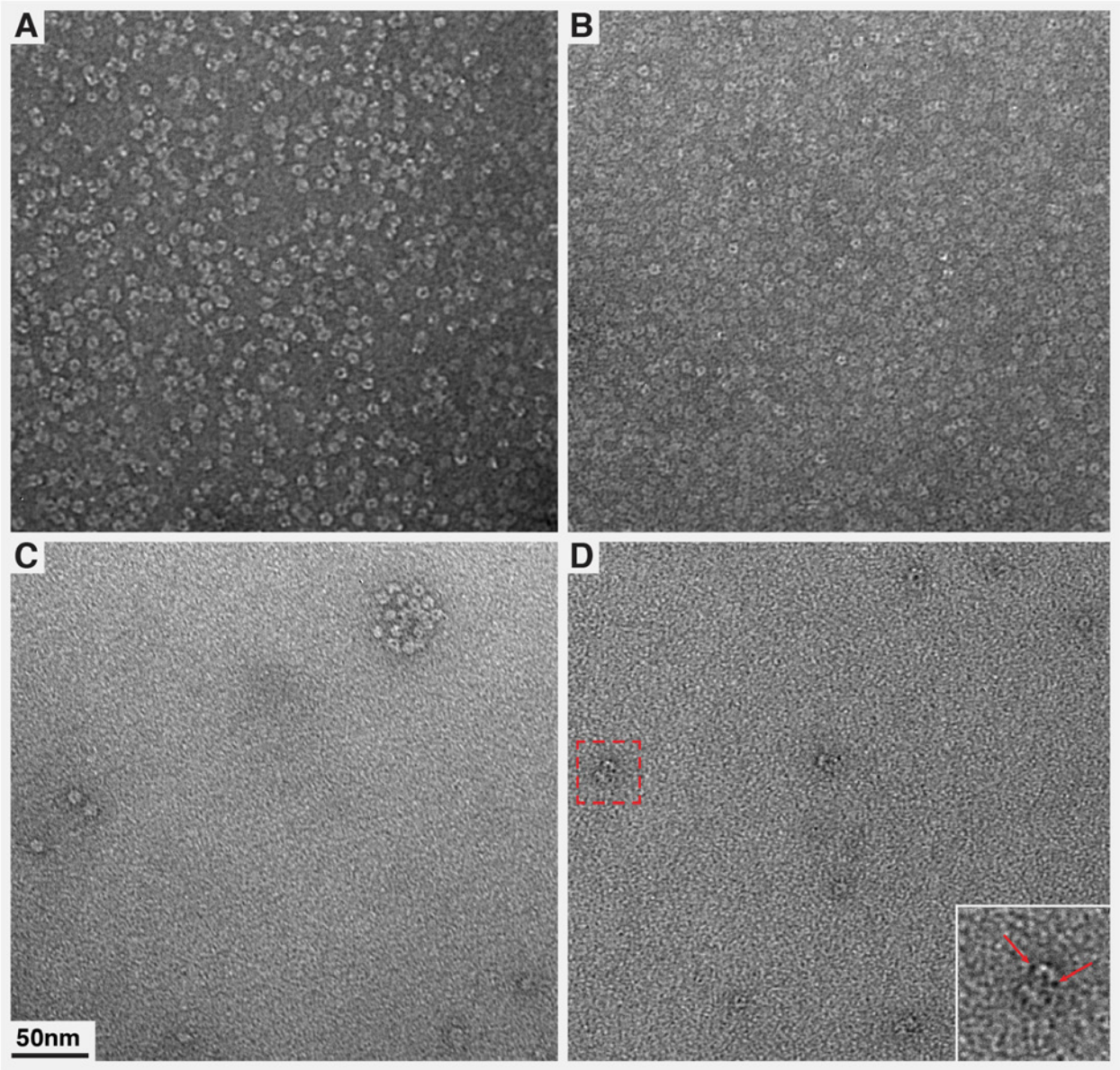

Figure 5-5: Polyomavirus VP1-A3 can form pentamers indistinguishable from those of WT VP1. (A) WT VP1 self-assembles into pentamers. **(B)** WT VP1 pentamers incubated with 100 μM $HAuCl_4$ and 100 μM HEPES for 2 min shows that the presence of the gold salt solution and reducing agent do not have adverse effects on the pentamer structure. **(C)** VP1-A3 forms pentamers akin to WT VP1. While the tagged pentamers are unlikely to be able to assemble in capsids, the addition of the A3 peptide onto the C-terminus of VP1 does not inhibit pentamer assembly. **(D)** VP1-A3 pentamers incubated with 100 μM $HAuCl_4$ and 50 μM HEPES for 2 min. shows some electron dense spots ~2 nm in diameter at each of the pentamer lobes that may correspond to gold particles.

small gold particles at each of the pentamer lobes. However, occasionally, similar electron dense spots could be seen in control specimens (VP1-A3 without $HAuCl_4$ or HEPES) that may arise from the staining solution interacting with the peptide.

Discussion

The findings reported in this chapter represent the best results obtained from a large number of experiments conducted from a 'trial and error' approach. The overwhelming conclusion from these experiments is that the use of metal-precipitating or metal-binding peptides as clonable labels for EM is still far from being adequately developed for routine use.

Our results suffered from being generally inconsistent and difficult to reproduce. For example, increasing the concentration of $HAuCl_4$ and HEPES did not always yield more or larger gold nanoparticles. Similarly, using lower concentrations did not always result in smaller particles, and neither did shorter incubation times. Thus, the reaction was not as 'tunable' as we had initially hoped. In addition, gold particle sizes would vary when experiments were repeated under the same conditions, and even in different areas of the same sample.

The success of this project relies on being able to carefully control both particle nucleation and particle growth (size). Ideally, we want to nucleate enough gold particles to have one particle bound per peptide, and we want the particle size to be 2-4 nm in diameter. Through our work it became clear that a trial and error approach was not the best way to tackle this project until more is understood about the chemistry of gold particle formation in the presence of A3, $HAuCl_4$ and HEPES because of the large number of variables in the reaction.

Two such variables are the concentration of metal salt solution ($HAuCl_4$) and concentration of reducing agent (HEPES) used. While a mechanism for how HEPES may reduce $HAuCl_4$ to form gold particles has been proposed (Habib et al., 2005), it is not completely clear how this is affected when A3 is present (Diamanti et al., 2009). Importantly, most metal salts (and their products when in combination with a reducing agent) can be extremely toxic to cells and biological complexes prepared *in vitro*. Indeed this is a major stumbling block in the application of these peptides as labels. In addition to varying $HAuCl_4$ concentration, other metal salt solutions such as $KAuCl_4$ and $NaAuCl_4$ may be tested. Similarly, alternative agents known to reduce gold salts aside from HEPES, such as citrate, sodium borohydride and other Good's buffers can be examined.

Additional variables in the gold particle formation reaction include the incubation time and incubation temperature. Given the toxicity of $HAuCl_4$ and HEPES to biological specimens, it is important to evaluate whether it is less detrimental to the sample to use lower concentrations of these reagents for longer incubation times, or use higher concentrations for shorter incubation times. All of our experiments were conducted at room temperature, however in other gold particle precipitation reactions, higher temperatures have been reported to increase particle nucleation resulting in smaller, more uniformly sized gold particles (Sardar and Shumaker-Parry, 2011) and may be beneficial here if higher temperatures can be tolerated by the specimen.

Finally, the concentration of peptide (in our case, the concentration of the protein of interest) is a particularly important variable to consider. While a previous report has suggested that only one A3 peptide is necessary to bind one gold nanoparticle (Chen et al., 2008), others have implied that multiple A3 peptides are necessary to influence the formation of the gold nanoparticles (Slocik et al., 2005; Diamanti et al., 2009). When the peptide is attached to a

biological molecule, it may not be able to function as it does when alone in solution especially if the peptide is confined to a certain position when attached to a protein that is part of a complex. Experiments aimed at gaining insight into the structure of A3-gold complexes may help to understand how many peptides are required to mediate precipitation of a single particle.

A drawback of the experiments presented here is that they suffer from the lack of a good negative control. HEPES reduces $HAuCl_4$ in the absence of the peptide, hence gold particles may still be present even when A3 is not in the sample. While these 'non-specific' particles usually appear larger and take on different shapes from those formed in the presence of A3, this will complicate data interpretation if these peptides are used for localizing proteins within cells.

Due to the problems associated with this project, I chose to focus my efforts elsewhere after one year. However, work on developing metal-binding tags is being continued in the lab. In the case of A3, using Au(I)Cl (which has Au(I)) instead of $HAuCl_4$ (which has Au(III)) seems to give better results. Using Au(I)Cl eliminates the need for a strong reducing agent such as HEPES which is required for reducing the Au(III) in $HAuCl_4$ to Au(0), thus taking one variable out of the reaction. However, Au(I)Cl is fairly insoluble in water and while smaller particles can be obtained which may bind specifically to A3, experiments still suffer from non-specific background particles and results are difficult to reproduce. Work is also currently being undertaken using proteins tagged with three tandem repeats of the peptide instead of one. While this work shows some initial success, additional insight into the gold particle precipitation reaction mechanism in the context of biological specimens must be obtained before metal-precipitating peptides can become useful marketable tools for EM.

Chapter 6. Disussion, Conclusions and Future Directions

The experiments presented in this thesis were directed at elucidating the mechanism that Kar3Vik1 uses for movement along MTs. Shortly before beginning this project, the crystal structure of Vik1 was published revealing that Vik1 possesses a structure very similar to a kinesin motor domain, despite lacking sequence similarity to any kinesin family members. Furthermore, Vik1 was shown to be able to bind to MTs by equilibrium cosedimentation, leading to the proposal of walking models where both Kar3 and Vik1 interact with the MT to facilitate movement. My work thus aimed to obtain structural details for how Vik1 interacts with the MT, and to reveal a novel mechanism for movement by a kinesin motor.

Despite numerous attempts using a wide variety of experimental conditions, I could never visualize Vik1 binding to MTs by EM. However, by analyzing the conformation of Kar3Vik1 bound to MTs in different nucleotide states, I have made a significant contribution to our understanding of Kar3Vik1's behavior when bound to MTs. My findings unexpectedly show that Kar3Vik1 moves along MTs in a way that is not novel, but instead provide evidence for conservation of a motility mechanism among minus end directed motors.

Kar3Vik1 uses a stalk rotation for minus-end directed motion

Using cryo-EM I have shown that Kar3Vik1 contacts MTs in a one-head-down, one-head-up binding configuration in the nucleotide-free, ATP and ADP+P_i states. I have also confirmed that Kar3Vik1 binds to MTs in a highly cooperative fashion which is different from Kar3 alone which binds stochastically to the MT lattice. Employing helical reconstruction, I have revealed that Kar3Vik1 undergoes a large conformational change upon uptake of ATP that

results in ~90° rotation of Kar3Vik1's coiled-coil stalk where it transitions from its plus end directed position in the nucleotide-free state, to point toward the MT minus end in the ATP state. Through the use of a maleimide-Nanogold label, I have demonstrated that Kar3 is the domain in contact with the MT to facilitate this powerstroke while Vik1 remains detached.

Utilizing an intermolecular crosslinked construct, I have provided evidence that the coiled-coil neck between Kar3 and Vik1 does not unwind to facilitate the powerstroke. Furthermore, a Kar3Vik1 construct with an intramolecular crosslink in Vik1 shows that Vik1 remains attached to the coiled-coil stalk during the stalk rotation, but that some rotation of Vik1 relative to the coiled-coil may be necessary for efficient uptake of nucleotide or for properly carrying out the powerstroke.

Based on my data, I propose a new model for Kar3Vik1 motility (Figure 6-1). When Kar3Vik1 is not bound to MTs, ADP is bound in the active site of Kar3. When Kar3 makes contact with an MT, ADP release from the active site is induced (Song and Endow, 1998). However, neither MT contact, nor ADP release cause large-scale structural changes in the overall conformation of the heterodimer. ATP is then taken up into Kar3's active site. This causes a ~90° rotation of Kar3Vik1's stalk that displaces the motor a short distance toward the minus end of the MT (keep in mind that *in vivo* Kar3Vik1 is tethered by its N-terminal domains to another microtubule, or perhaps a spindle matrix component that will support the powerstroke and retrograde displacement). ATP is then hydrolyzed, which does not result in a large structural rearrangement, but does reduce the affinity of Kar3 for the MT and Kar3Vik1 detaches from the MT either before or after the release of P_i. Away from the MT, the coiled-coil stalk resets to its original position and the cycle can start again.

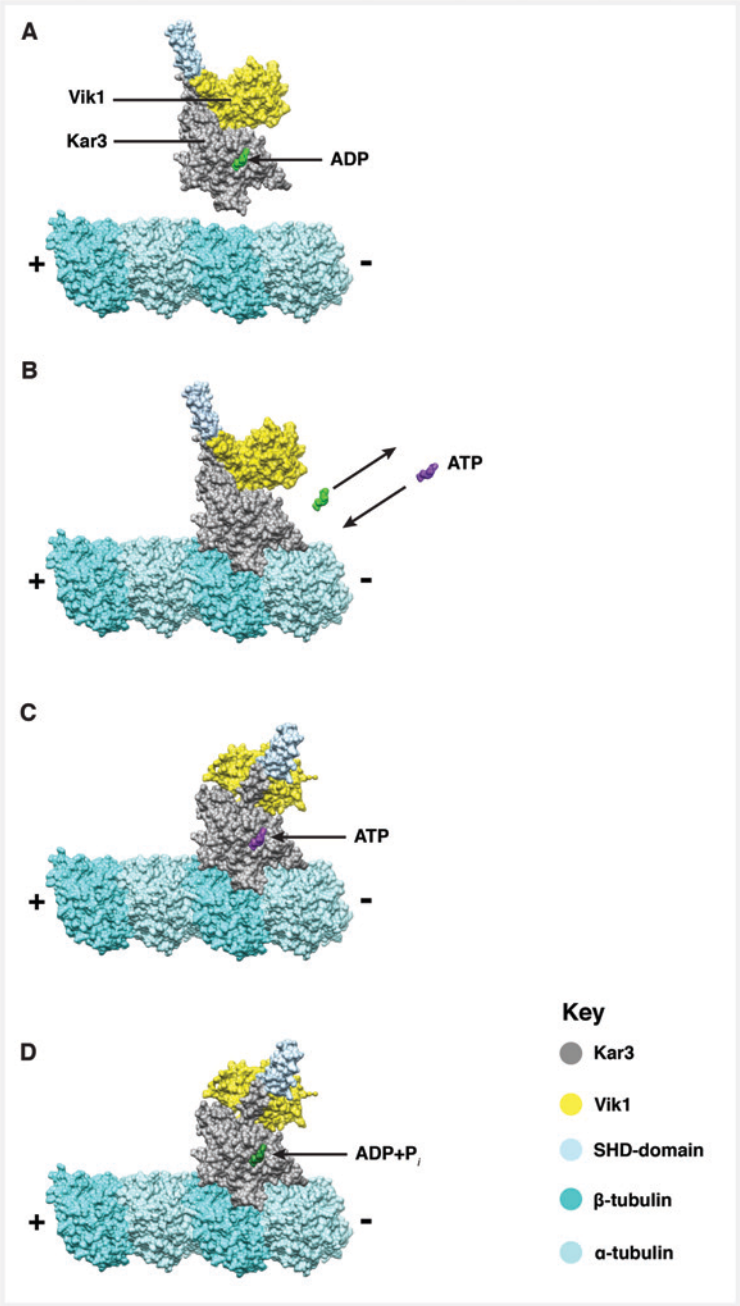

Figure 6-1: A new model for Kar3Vik1 movement along MTs. This model is proposed based on the conformational changes seen in helical reconstructions (Figures 3-4 and 3-7) and x-ray crystal structure docking into EM maps (Figure 3-16). **(A)** When Kar3Vik1 is not bound to MTs, ADP is present in Kar3's nucleotide-binding site. **(B)** Kar3 makes contact with an MT which induces ADP release from the active site, but does not cause large-scale conformational changes in Kar3Vik1. **(C)** ATP is subsequently taken up into Kar3's active site which results in a ~90° rotation of Kar3Vik1's coiled-coil that displaces the motor a short distance toward the MT minus end. **(D)** ATP is then hydrolyzed, which does not lead to a large-scale structural rearrangement, but does reduce the affinity of Kar3 for the MT. Kar3Vik1 can then detach from the MT and the coiled-coil stalk returns to its original position so the cycle can start again.

Kar3Vik1's powerstroke shares strong similarities to that of Ncd

The cryo-EM nucleotide-state conformations of Kar3Vik1 bound to MTs described here and Kar3Vik1's cooperative MT binding pattern are both highly reminiscent of those reported for the homodimeric kinesin-14 Ncd (Wendt et al., 2002; Endres et al., 2006). Cryo-EM and helical reconstruction of Ncd-MT complexes has shown that the Ncd stalk points to the MT plus end in the nucleotide-free state, and undergoes a ~70° rotation toward the minus end when complexed with AMP-PNP. Also similar is the close fit of an ADP-state X-ray crystal structure of Ncd into cryo-EM maps of Ncd bound to MTs in the nucleotide-free state (Wendt et al., 2002), and the observation that the Ncd-ADP-AlF_4^- binding state closely resembles the AMP-PNP state (Endres et al., 2006). These results have led to the proposal that Ncd uses a 'lever-arm' rotation to power its retrograde movement. This lever-arm model has been well supported by evidence demonstrating that the MT-gliding velocity of a number of Ncd truncation or extension mutants is proportional to the length of the coiled-coil stalk (Endres et al., 2006).

The similarity between the Kar3Vik1 and Ncd powerstrokes is not entirely surprising. At the sequence level, key residues reported to be critical for Ncd's retrograde motility are conserved in Kar3 (Figure 6-2). Notably, a point mutation, N340K, close to the base of Ncd's coiled-coil neck has been shown to move both toward the plus and minus end of MTs (Endow and Higuchi, 2000). This residue is conserved in Kar3 (N378) and indeed N378K mutants of Kar3 are able to suppress the lethality of deleting the plus end directed mitotic kinesin-5s better than a complete Kar3 deletion (Hoyt et al., 1993) indicating that this mutant can produce some of the outward force provided by plus end directed motors. In addition, the mutation K460A in Ncd results in a three-fold decrease in Ncd's MT gliding velocity, and an Ncd triple mutant

Figure 6-2: Sequence alignment of the C-terminal regions of Ncd, Kar3 and Vik1. Full length sequences of Ncd, Kar3 and Vik1 were aligned using ClustalW (EMBL-EBI, Cambridge, UK; Larkin et al., 2007) though only sequences of part of the stalk, the coiled-coiled neck and globular head regions are shown. The glycine residue at the base of the neck in Ncd and Kar3 is highlighted in pink. This residue, G347, is thought to be the pivot point for the stalk rotation that occurs upon uptake of ATP. G347, together with the preceding 12 residues, make up the neck region which is highly conserved among kinesin-14s. This region includes N340 (green), which when mutated in Ncd and Kar3 causes the motors to move bidirectionally. N340 as well as other conserved residues in the neck (turquoise) are shown in the Ncd dimer crystal structure to make contact with conserved residues in the head domain (red, navy and purple) (Sablin et al., 1998). The Ncd mutant K640A (purple) and Ncd triple mutant Q420A/S421A/Y426A (red) show 3- and 10-fold slower MT gliding velocities over WT Ncd respectively. All these residues are conserved in Kar3 reinforcing their importance in facilitating minus end directed motility.

Q420A/S421A/Y426A glides MTs ten times slower than WT Ncd (Sablin et al., 1998). All four of these residues are conserved in Kar3.

Finally, the residue at the base of the neck, G347 in Ncd (G385 in Kar3 and G373 in Vik1), is also highly conserved across all kinesin-14s. At G347, the coiled-coil ends and makes a sharp turn to the first residue of the globular head domain. G347 is thus believed to be the pivot point for the stalk rotation that occurs during upon uptake of ATP. Importantly, many of the residues mentioned here are conserved only among the C-terminal kinesins, which further implicates them in a fundamental role in retrograde stepping.

The work presented here highlights the conservation of a lever arm rotation as a mechanism of movement among the minus-end directed kinesins. Nevertheless, despite their similarities, Kar3Vik1 and Ncd have a striking difference in that Kar3Vik1 has only one ATP-binding site. While inconsistent with my data, Vik1's reported ability to bind to MTs despite lacking an active site for ATP hydrolysis, implies that Kar3Vik1 must have additional requirements besides the powerstroke for proper motility and perhaps a stronger reliance on structural communication between the Kar3 and Vik1 domains. Or perhaps, as my work suggests, Vik1 may not bind to MTs at all.

Does Vik1 truly bind to MTs?

Those that favor motility models involving Vik1's interaction with the MT propose that in the ADP state, Vik1 is in contact with the MT in an orientation different from Kar3 and that Kar3 is tethered. Strain in the coiled-coil would then position Kar3 such that it can bind the MT at its binding site on β-tubulin on an adjacent protofilament. As the ADP state represents the

'solution' or unbound state of kinesins, these events, if they occur represent the earliest stage in Kar3Vik1's motility cycle. In addition to the work shown in Chapter 3, I have also conducted experiments with Kar3Vik1 in the presence of high concentrations of ADP added immediately before plunge-freezing and incubated for up to 1 minute prior to freezing. Under these conditions, a close-to nucleotide-free (when added immediately before) or the nucleotide-free state is obtained (1 min incubation). Nanogold®-labeling has reinforced that it is Kar3 in contact with the MT under these conditions. My interpretation of these Kar3Vik1-ADP results is that Kar3 contacts the MT first, which stimulates loss of ADP from the active site, and the nucleotide-free state is achieved. Taken together with my results where Vik1MHD was never seen binding to MTs by EM and little binding of Kar3Vik1 with ADP (> 10 min incubation) was obtained, I believe that the question of whether Vik1 really does bind to MTs remains unanswered. Additional experiments that can add evidence for or against Vik1 binding are suggested.

An important test would be to create a ‘one headed’ construct which contains the Kar3 head and coiled-coil region of Kar3 and Vik1, but lacks the Vik1 C-terminal globular domain. Experiments with an analogous Ncd construct showed that the one-headed motor was able to glide MTs at the same velocity as WT homodimeric Ncd (Endres et al., 2006). This interesting result demonstrated the importance of the coiled-coil for movement, but implied that the second Ncd head was not necessary for proper motility. If Vik1’s interaction with the MT is an integral part of Kar3Vik1’s motility cycle then I would predict that the one-headed mutant would show drastically reduced MT gliding velocity compared to WT Kar3Vik1.

Another experiment would be to generate mutations in key residues involved in MT-binding on Kar3 to create a construct where Kar3 is unable to bind to MTs. While the residues in

kinesin involved in MT binding are known (Woehlke et al., 1997), attempts by the Rayment lab to replace these residues have been unsuccessful. Perhaps another way would be to use the cysteine free mutants and engineer a cysteine in the region of the MT binding site for labeling with a Nanogold® or larger particle (in fact the Rayment lab has generated a single-cysteine GFP that can be crosslinked to Kar3 for this purpose). If Vik1 does bind to MTs, then I would predict that equilibrium cosedimentation results with this construct in the ADP state would provide similar results to those with WT Kar3Vik1.

In addition to bulk motility and cosedimentation experiments, single molecule work can provide valuable insight into Kar3Vik1's mechanism of motility. A consequence of Vik1's interaction with the MT is that it requires Kar3 MT binding to provide the force for dissociation of Vik1 from the MT. Results from motility experiments with GCN4-Kar3Vik1-M4M, the construct with a 10 Å crosslink at the base of the coiled-coil (see Chapter 3) suggest that the only way Kar3 and Vik1 can simultaneously contact the MT is if they bind laterally to adjacent protofilaments and in opposite orientations. Thus, the distance changes between Kar3 and Vik1 in a motility cycle that involves Vik1's interaction with the MTs is predicted to be very different from distance changes predicted for binding only by Kar3 while Vik1 extends away from the MT. By placing fluorescent probes at key locations in Kar3Vik1, the structural changes that occur between the heads during stepping can be measured by monitoring the positions of the fluorescent probes on individual molecules. Similar work has been carried out successfully with kinesin-1 lending weight to the hand-over-hand model proposed for kinesin-1 motility (Asenjo et al., 2003).

Structural basis for the functional differences between Kar3Vik1 and Kar3Cik1

One of the unusual properties of Kar3 is that in addition to associating with Vik1, Kar3 also has another interacting partner, Cik1 as introduced in Chapter 1 (Page et al., 1994, Barrett et al., 2000). While Vik1 and Cik1 have a high level of sequence homology, genetics and *in vivo* localization have demonstrated that Kar3Vik1 and Kar3Cik1 have remarkably different properties and are responsible for carrying out very different functions (Manning et al., 1999). For example, Kar3Vik1 localizes predominantly at the spindle poles during mitosis while Kar3Cik1 localizes to the plus ends of MT and along the length of MTs in the spindle. The localization of Kar3 is completely dependent on its binding partner, such that when both Vik1 and Cik1 are deleted, Kar3 localizes throughout the nucleus (Manning and Snyder, 2000). Furthermore, deletion of either Vik1 or Cik1 gives rise to distinct phenotypes. When Cik1 is deleted, a high frequency of chromosome loss is observed (Page and Snyder, 1992). Conversely, when Vik1 is deleted, the level of chromosome loss is not much higher than that of WT cells (Manning et al., 1999). Consistent with this, Kar3Cik1 has been implicated in facilitating proper attachment of MTs to kinetochores, while there is no evidence that Kar3Vik1 is involved in this (Liu et al., 2011).

Disruption of Vik1 partially rescues the spindle collapse brought about by deleting both of the kinesin-5s (Cin8 and Kip1) in yeast. However, deletion of Cik1 does not rescue this phenotype (Manning et al., 1999). This result suggests that Kar3Vik1 provides an inward force in the mitotic spindle to oppose the outward force produced by the kinesin-5s, while Kar3Cik does not.

Interestingly, Kar3Cik1 has been reported to have robust depolymerizing activity *in vitro*, predominantly from MT plus ends (Sproul et al., 2005) and there is also evidence for

depolymerization by Kar3Cik1 *in vivo* (Page and Snyder 1992). In contrast, Kar3Vik1 lacks robust, specific depolymerizing activity and instead gradually depolymerizes MTs from both the plus and minus ends *in vitro*, similar to the depolymerizing activity reported for Ncd (Allingham et al., 2007).

My work with Kar3Vik1 has provided a strong foundation for examining Kar3Cik1 under similar conditions. By comparing the MT-interacting properties of Kar3Cik1 and Kar3Vik1 by EM, and analyzing helical reconstructions of Kar3Vik1-MT and Kar3Cik1-MT complexes, we can look for structural differences that may provide clues into how Kar3Vik1 and Kar3Cik1 are suited to carry out their respective activities.

Currently, Kar3Vik1 and Kar3Cik1 are the only known examples of a kinesin that heterodimerises with two distict non-motor proteins to regulate its function. However, Vik1 shares low sequence identity to kinesins even though their structures are similar. It is thus possible that motor homology proteins like Vik1 and Cik1 that serve to diversify kinesin activity, are present, but as yet undetected, in other organisms.

References

Allingham, J.S., L.R. Sproul, I. Rayment, and S.P. Gilbert. 2007. Vik1 modulates microtubule-Kar3 interactions through a motor domain that lacks an active site. *Cell*. 128:1161-1172.

Alushin, G.M., V.H. Ramey, S. Pasqualato, D.A. Ball, N. Grigorieff, A. Musacchio, and E. Nogales. 2010. The Ndc80 kinetochore complex forms oligomeric arrays along microtubules. *Nature*. 467:805-810.

Amos, L., and A. Klug. 1974. Arrangement of subunits in flagellar microtubules. *J Cell Sci*. 14:523-549.

Amos, L.A. 1995. The microtubule lattice--20 years on. *Trends Cell Biol*. 5:48-51.

Arnal, I., F. Metoz, S. DeBonis, and R.H. Wade. 1996. Three-dimensional structure of functional motor proteins on microtubules. *Curr Biol*. 6:1265-1270.

Asbury, C.L., A.N. Fehr, and S.M. Block. 2003. Kinesin moves by an asymmetric hand-over-hand mechanism. *Science*. 302:2130-2134.

Asenjo, A.B., N. Krohn, and H. Sosa. 2003. Configuration of the two kinesin motor domains during ATP hydrolysis. *Nat Struct Biol*. 10:836-842.

Barrett, J.G., B.D. Manning, and M. Snyder. 2000. The Kar3p kinesin-related protein forms a novel heterodimeric structure with its associated protein Cik1p. *Mol Biol Cell*. 11:2373-2385.

Beuron, F., and A. Hoenger. 2001. Structural analysis of the microtubule-kinesin complex by cryo-electron microscopy. *Methods Mol Biol*. 164:235-254.

Blangy, A., H.A. Lane, P. d'Herin, M. Harper, M. Kress, and E.A. Nigg. 1995. Phosphorylation by p34cdc2 regulates spindle association of human Eg5, a kinesin-related motor essential for bipolar spindle formation in vivo. *Cell*. 83:1159-1169.

Block, S.M., and K. Svoboda. 1995. Analysis of high resolution recordings of motor movement. *Biophys J*. 68:230s-241s.

Bodey, A.J., M. Kikkawa, and C.A. Moores. 2009. 9-Angstrom structure of a microtubule-bound mitotic motor. *J Mol Biol*. 388:218-224.

Bouchet-Marquis, C., V. Starkuviene, and M. Grabenbauer. 2008. Golgi apparatus studied in vitreous sections. *J Microsc*. 230:308-316.

Bouchet-Marquis, C., B. Zuber, A.M. Glynn, M. Eltsov, M. Grabenbauer, K.N. Goldie, D. Thomas, A.S. Frangakis, J. Dubochet, and D. Chretien. 2007. Visualization of cell microtubules in their native state. *Biol Cell*. 99:45-53.

Brady, S.T., R.J. Lasek, and R.D. Allen. 1985. Video microscopy of fast axonal transport in extruded axoplasm: a new model for study of molecular mechanisms. *Cell Motil*. 5:81-101.

Braun, M., D.R. Drummond, R.A. Cross, and A.D. McAinsh. 2009. The kinesin-14 Klp2 organizes microtubules into parallel bundles by an ATP-dependent sorting mechanism. *Nat Cell Biol*. 11:724-730.

Brown, S. 1997. Metal-recognition by repeating polypeptides. *Nat Biotechnol*. 15:269-272.

Brown, S., M. Sarikaya, and E. Johnson. 2000. A genetic analysis of crystal growth. *J Mol Biol*. 299:725-735.

Cai, S., L.N. Weaver, S.C. Ems-McClung, and C.E. Walczak. 2009. Kinesin-14 family proteins HSET/XCTK2 control spindle length by cross-linking and sliding microtubules. *Mol Biol Cell*. 20:1348-1359.

Carragher, B., M. Whittaker, and R.A. Milligan. 1996. Helical processing using PHOELIX. *J Struct Biol*. 116:107-112.

Chacon, P., and W. Wriggers. 2002. Multi-resolution contour-based fitting of macromolecular structures. *J Mol Biol*. 317:375-384.

Chandra, R., E.D. Salmon, H.P. Erickson, A. Lockhart, and S.A. Endow. 1993. Structural and functional domains of the Drosophila ncd microtubule motor protein. *J Biol Chem*. 268:9005-9013.

Chen, C.L., P. Zhang, and N.L. Rosi. 2008. A new peptide-based method for the design and synthesis of nanoparticle superstructures: construction of highly ordered gold nanoparticle double helices. *J Am Chem Soc*. 130:13555-13557.

Chretien, D., and R.H. Wade. 1991. New data on the microtubule surface lattice. *Biol Cell*. 71:161-174.

Cochran, J.C., C.A. Sontag, Z. Maliga, T.M. Kapoor, J.J. Correia, and S.P. Gilbert. 2004. Mechanistic analysis of the mitotic kinesin Eg5. *J Biol Chem*. 279:38861-38870.

Cope, J., S. Gilbert, I. Rayment, D. Mastronarde, and A. Hoenger. 2010. Cryo-electron tomography of microtubule-kinesin motor complexes. *J Struct Biol*. 170:257-265.

Cope, J., J. Heumann, and A. Hoenger. 2011. Cryo-electron tomography for structural characterization of macromolecular complexes. *Curr Protoc Protein Sci*. 65:17.13.1-17.13.31.

Cottingham, F.R., L. Gheber, D.L. Miller, and M.A. Hoyt. 1999. Novel roles for Saccharomyces cerevisiae mitotic spindle motors. *J Cell Biol*. 147:335-350.

Crowther, R.A., R. Henderson, and J.M. Smith. 1996. MRC image processing programs. *J Struct Biol*. 116:9-16.

Dagenbach, E.M., and S.A. Endow. 2004. A new kinesin tree. *J Cell Sci*. 117:3-7.

deCastro, M.J., R.M. Fondecave, L.A. Clarke, C.F. Schmidt, and R.J. Stewart. 2000. Working strokes by single molecules of the kinesin-related microtubule motor ncd. *Nat Cell Biol*. 2:724-729.

deCastro, M.J., C.H. Ho, and R.J. Stewart. 1999. Motility of dimeric ncd on a metal-chelating surfactant: evidence that ncd is not processive. *Biochemistry*. 38:5076-5081.

DeRosier, D.J., and A. Klug. 1968. Reconstruction of three dimensional structures from electron micrographs. *Nature*. 217:130-134.

DeRosier, D.J., and P.B. Moore. 1970. Reconstruction of three-dimensional images from electron micrographs of structures with helical symmetry. *J Mol Biol*. 52:355-369.

des Georges, A., M. Katsuki, D.R. Drummond, M. Osei, R.A. Cross, and L.A. Amos. 2008. Mal3, the Schizosaccharomyces pombe homolog of EB1, changes the microtubule lattice. *Nat Struct Mol Biol*. 15:1102-1108.

Desai, A., and T.J. Mitchison. 1997. Microtubule polymerization dynamics. *Annu Rev Cell Dev Biol*. 13:83-117.

Diamanti, S., A. Elsen, R. Naik, and R. Vaia. 2009. Relative functionality of buffer and peptide in gold nanoparticle formation. *J Phys Chem C*. 113:9993-9997.

Dias, D.P., and R.A. Milligan. 1999. Motor protein decoration of microtubules grown in high salt conditions reveals the presence of mixed lattices. *J Mol Biol*. 287:287-292.

Dickerson, M.B., K.H. Sandhage, and R.R. Naik. 2008. Protein- and peptide-directed syntheses of inorganic materials. *Chem Rev*. 108:4935-4978.

Dubochet, J. 2007. The physics of rapid cooling and its implications for cryoimmobilization of cells. *Methods Cell Biol*. 79:7-21.

Dubochet, J., M. Adrian, J.J. Chang, J.C. Homo, J. Lepault, A.W. McDowall, and P. Schultz. 1988. Cryo-electron microscopy of vitrified specimens. *Q Rev Biophys*. 21:129-228.

Dubochet, J., F.P. Booy, R. Freeman, A.V. Jones, and C.A. Walter. 1981. Low temperature electron microscopy. *Annu Rev Biophys Bioeng*. 10:133-149.

Endow, S.A., R. Chandra, D.J. Komma, A.H. Yamamoto, and E.D. Salmon. 1994a. Mutants of the Drosophila ncd microtubule motor protein cause centrosomal and spindle pole defects in mitosis. *J Cell Sci*. 107 (Pt 4):859-867.

Endow, S.A., S. Henikoff, and L. Soler-Niedziela. 1990. Mediation of meiotic and early mitotic chromosome segregation in Drosophila by a protein related to kinesin. *Nature*. 345:81-83.

Endow, S.A., and H. Higuchi. 2000. A mutant of the motor protein kinesin that moves in both directions on microtubules. *Nature*. 406:913-916.

Endow, S.A., S.J. Kang, L.L. Satterwhite, M.D. Rose, V.P. Skeen, and E.D. Salmon. 1994b. Yeast Kar3 is a minus-end microtubule motor protein that destabilizes microtubules preferentially at the minus ends. *EMBO J*. 13:2708-2713.

Endres, N.F., C. Yoshioka, R.A. Milligan, and R.D. Vale. 2006. A lever-arm rotation drives motility of the minus-end-directed kinesin Ncd. *Nature*. 439:875-878.

Enos, A.P., and N.R. Morris. 1990. Mutation of a gene that encodes a kinesin-like protein blocks nuclear division in A. nidulans. *Cell*. 60:1019-1027.

Fan, J., A.D. Griffiths, A. Lockhart, R.A. Cross, and L.A. Amos. 1996. Microtubule minus ends can be labelled with a phage display antibody specific to alpha-tubulin. *J Mol Biol*. 259:325-330.

Fink, G., L. Hajdo, K.J. Skowronek, C. Reuther, A.A. Kasprzak, and S. Diez. 2009. The mitotic kinesin-14 Ncd drives directional microtubule-microtubule sliding. *Nat Cell Biol*. 11:717-723.

Foster, K.A., J.J. Correia, and S.P. Gilbert. 1998. Equilibrium binding studies of non-claret disjunctional protein (Ncd) reveal cooperative interactions between the motor domains. *J Biol Chem*. 273:35307-35318.

Foster, K.A., and S.P. Gilbert. 2000. Kinetic studies of dimeric Ncd: evidence that Ncd is not processive. *Biochemistry*. 39:1784-1791.

Foster, K.A., A.T. Mackey, and S.P. Gilbert. 2001. A mechanistic model for Ncd directionality. *J Biol Chem*. 276:19259-19266.

Frangakis, A.S., and R. Hegerl. 2001. Noise reduction in electron tomographic reconstructions using nonlinear anisotropic diffusion. *J Struct Biol*. 135:239-250.

Gardner, M.K., J. Haase, K. Mythreye, J.N. Molk, M. Anderson, A.P. Joglekar, E.T. O'Toole, M. Winey, E.D. Salmon, D.J. Odde, and K. Bloom. 2008. The microtubule-based motor Kar3 and plus end-binding protein Bim1 provide structural support for the anaphase spindle. *J Cell Biol*. 180:91-100.

Gilbert, S.P., M.R. Webb, M. Brune, and K.A. Johnson. 1995. Pathway of processive ATP hydrolysis by kinesin. *Nature*. 373:671-676.

Gonen, T., Y. Cheng, P. Sliz, Y. Hiroaki, Y. Fujiyoshi, S.C. Harrison, and T. Walz. 2005. Lipid-protein interactions in double-layered two-dimensional AQP0 crystals. *Nature*. 438:633-638.

Gulick, A.M., H. Song, S.A. Endow, and I. Rayment. 1998. X-ray crystal structure of the yeast Kar3 motor domain complexed with Mg.ADP to 2.3 A resolution. *Biochemistry*. 37:1769-1776.

Habib, A., M. Tabata, and Y.G. Wu. 2005. Formation of gold nanoparticles by Good's buffers. *Bull. Chem. Soc. Jpn*. 78:262-269.

Hackney, D.D. 1994. Evidence for alternating head catalysis by kinesin during microtubule-stimulated ATP hydrolysis. *Proc Natl Acad Sci U S A*. 91:6865-6869.

Hackney, D.D. 1995. Highly processive microtubule-stimulated ATP hydrolysis by dimeric kinesin head domains. *Nature*. 377:448-450.

Hancock, W.O., and J. Howard. 1998. Processivity of the motor protein kinesin requires two heads. *J Cell Biol*. 140:1395-1405.

Harauz, G., and M. van Heel. 1986. Exact filters for general geometry three dimensional reconstruction. *Optik*. 73:146-156.

Heck, M.M., A. Pereira, P. Pesavento, Y. Yannoni, A.C. Spradling, and L.S. Goldstein. 1993. The kinesin-like protein KLP61F is essential for mitosis in Drosophila. *J Cell Biol*. 123:665-679.

Herrmann, H., M. Haner, M. Brettel, S.A. Muller, K.N. Goldie, B. Fedtke, A. Lustig, W.W. Franke, and U. Aebi. 1996. Structure and assembly properties of the intermediate filament protein vimentin: the role of its head, rod and tail domains. *J Mol Biol*. 264:933-953.

Hirokawa, N. 1998. Kinesin and dynein superfamily proteins and the mechanism of organelle transport. *Science*. 279:519-526.

Hirokawa, N., and Y. Noda. 2008. Intracellular transport and kinesin superfamily proteins, KIFs: structure, function, and dynamics. *Physiol Rev*. 88:1089-1118.

Hirokawa, N., Y. Noda, Y. Tanaka, and S. Niwa. 2009. Kinesin superfamily motor proteins and intracellular transport. *Nat Rev Mol Cell Biol*. 10:682-696.

Hirose, K., E. Akimaru, T. Akiba, S.A. Endow, and L.A. Amos. 2006. Large conformational changes in a kinesin motor catalyzed by interaction with microtubules. *Mol Cell*. 23:913-923.

Hoenger, A., and H. Gross. 2008. Structural investigations into microtubule-MAP complexes. *Methods Cell Biol*. 84:425-444.

Hoenger, A., and R.A. Milligan. 1997. Motor domains of kinesin and ncd interact with microtubule protofilaments with the same binding geometry. *J Mol Biol*. 265:553-564.

Hoenger, A., S. Sack, M. Thormahlen, A. Marx, J. Muller, H. Gross, and E. Mandelkow. 1998. Image reconstructions of microtubules decorated with monomeric and dimeric kinesins: comparison with x-ray structure and implications for motility. *J Cell Biol*. 141:419-430.

Hoenger, A., M. Thormahlen, R. Diaz-Avalos, M. Doerhoefer, K.N. Goldie, J. Muller, and E. Mandelkow. 2000. A new look at the microtubule binding patterns of dimeric kinesins. *J Mol Biol*. 297:1087-1103.

Howard, J., A.J. Hudspeth, and R.D. Vale. 1989. Movement of microtubules by single kinesin molecules. *Nature*. 342:154-158.

Howard, J., and A.A. Hyman. 2003. Dynamics and mechanics of the microtubule plus end. *Nature*. 422:753-758.

Howard, J., and A.A. Hyman. 2009. Growth, fluctuation and switching at microtubule plus ends. *Nat Rev Mol Cell Biol*. 10:569-574.

Hoyt, M.A., L. He, L. Totis, and W.S. Saunders. 1993. Loss of function of Saccharomyces cerevisiae kinesin-related CIN8 and KIP1 is suppressed by KAR3 motor domain mutations. *Genetics*. 135:35-44.

Hua, W., J. Chung, and J. Gelles. 2002. Distinguishing inchworm and hand-over-hand processive kinesin movement by neck rotation measurements. *Science*. 295:844-848.

Kapitein, L.C., E.J. Peterman, B.H. Kwok, J.H. Kim, T.M. Kapoor, and C.F. Schmidt. 2005. The bipolar mitotic kinesin Eg5 moves on both microtubules that it crosslinks. *Nature*. 435:114-118.

Karabay, A., and R.A. Walker. 1999. Identification of microtubule binding sites in the Ncd tail domain. *Biochemistry*. 38:1838-1849.

Kaseda, K., H. Higuchi, and K. Hirose. 2003. Alternate fast and slow stepping of a heterodimeric kinesin molecule. *Nat Cell Biol*. 5:1079-1082.

Kashina, A.S., R.J. Baskin, D.G. Cole, K.P. Wedaman, W.M. Saxton, and J.M. Scholey. 1996. A bipolar kinesin. *Nature*. 379:270-272.

Kikkawa, M., T. Ishikawa, T. Nakata, T. Wakabayashi, and N. Hirokawa. 1994. Direct visualization of the microtubule lattice seam both in vitro and in vivo. *J Cell Biol*. 127:1965-1971.

Kikkawa, M., E.P. Sablin, Y. Okada, H. Yajima, R.J. Fletterick, and N. Hirokawa. 2001. Switch-based mechanism of kinesin motors. *Nature*. 411:439-445.

Kirmse, R., C. Bouchet-Marquis, C. Page, and A. Hoenger. 2010. Three-dimensional cryo-electron microscopy on intermediate filaments. *Methods Cell Biol*. 96:565-589.

Kremer, J.R., D.N. Mastronarde, and J.R. McIntosh. 1996. Computer visualization of three-dimensional image data using IMOD. *J Struct Biol*. 116:71-76.

Kriplani, U., and B.K. Kay. 2005. Selecting peptides for use in nanoscale materials using phage-displayed combinatorial peptide libraries. *Curr Opin Biotechnol*. 16:470-475.

Krzysiak, T.C., T. Wendt, L.R. Sproul, P. Tittmann, H. Gross, S.P. Gilbert, and A. Hoenger. 2006. A structural model for monastrol inhibition of dimeric kinesin Eg5. *EMBO J*. 25:2263-2273.

Kuriyama, R., M. Kofron, R. Essner, T. Kato, S. Dragas-Granoic, C.K. Omoto, and A. Khodjakov. 1995. Characterization of a minus end-directed kinesin-like motor protein from cultured mammalian cells. *J Cell Biol*. 129:1049-1059.

Kwon, M., S.A. Godinho, N.S. Chandhok, N.J. Ganem, A. Azioune, M. Thery, and D. Pellman. 2008. Mechanisms to suppress multipolar divisions in cancer cells with extra centrosomes. *Genes Dev*. 22:2189-2203.

Larkin, M.A., G. Blackshields, N.P. Brown, R. Chenna, P.A. McGettigan, H. McWilliam, F. Valentin, I.M. Wallace, A. Wilm, R. Lopez, J.D. Thompson, T.J. Gibson, and D.G. Higgins. 2007. Clustal W and Clustal X version 2.0. *Bioinformatics*. 23:2947-2948.

Lawrence, C.J., R.L. Malmberg, M.G. Muszynski, and R.K. Dawe. 2002. Maximum likelihood methods reveal conservation of function among closely related kinesin families. *J Mol Evol*. 54:42-53.

Liu, H., F. Jin, F. Liang, X. Tian, and Y. Wang. 2011. The Cik1/Kar3 motor complex is required for the proper kinetochore-microtubule interaction after stressful DNA replication. *Genetics*. 187:397-407.

Lowe, J., H. Li, K.H. Downing, and E. Nogales. 2001. Refined structure of alpha beta-tubulin at 3.5 A resolution. *J Mol Biol*. 313:1045-1057.

Lucic, V., F. Forster, and W. Baumeister. 2005. Structural studies by electron tomography: from cells to molecules. *Annu Rev Biochem*. 74:833-865.

Mackey, A.T., and S.P. Gilbert. 2003. The ATPase cross-bridge cycle of the Kar3 motor domain. Implications for single head motility. *J Biol Chem*. 278:3527-3535.

Mackey, A.T., L.R. Sproul, C.A. Sontag, L.L. Satterwhite, J.J. Correia, and S.P. Gilbert. 2004. Mechanistic analysis of the Saccharomyces cerevisiae kinesin Kar3. *J Biol Chem*. 279:51354-51361.

Mandelkow, E., E.M. Mandelkow, H. Hotani, B. Hess, and S.C. Muller. 1989. Spatial patterns from oscillating microtubules. *Science*. 246:1291-1293.

Mandelkow, E., Y.H. Song, and E.M. Mandelkow. 1995. The microtubule lattice--dynamic instability of concepts. *Trends Cell Biol*. 5:262-266.

Mandelkow, E.M., G. Lange, A. Jagla, U. Spann, and E. Mandelkow. 1988. Dynamics of the microtubule oscillator: role of nucleotides and tubulin-MAP interactions. *EMBO J*. 7:357-365.

Mandelkow, E.M., R. Schultheiss, R. Rapp, M. Muller, and E. Mandelkow. 1986. On the surface lattice of microtubules: helix starts, protofilament number, seam, and handedness. *J Cell Biol*. 102:1067-1073.

Manning, B.D., J.G. Barrett, J.A. Wallace, H. Granok, and M. Snyder. 1999. Differential regulation of the Kar3p kinesin-related protein by two associated proteins, Cik1p and Vik1p. *J Cell Biol*. 144:1219-1233.

Manning, B.D., and M. Snyder. 2000. Drivers and passengers wanted! The role of kinesin-associated proteins. *Trends Cell Biol*. 10:281-289.

Mastronarde, D.N. 2005. Automated electron microscope tomography using robust prediction of specimen movements. *J Struct Biol*. 152:36-51.

Mayer, T.U., T.M. Kapoor, S.J. Haggarty, R.W. King, S.L. Schreiber, and T.J. Mitchison. 1999. Small molecule inhibitor of mitotic spindle bipolarity identified in a phenotype-based screen. *Science*. 286:971-974.

McDonald, H.B., R.J. Stewart, and L.S. Goldstein. 1990. The kinesin-like ncd protein of Drosophila is a minus end-directed microtubule motor. *Cell*. 63:1159-1165.

McIntosh, J.R., M.K. Morphew, P.M. Grissom, S.P. Gilbert, and A. Hoenger. 2009. Lattice structure of cytoplasmic microtubules in a cultured mammalian cell. *J Mol Biol*. 394:177-182.

McIntosh, R., D. Nicastro, and D. Mastronarde. 2005. New views of cells in 3D: an introduction to electron tomography. *Trends Cell Biol*. 15:43-51.

Medalia, O., I. Weber, A.S. Frangakis, D. Nicastro, G. Gerisch, and W. Baumeister. 2002. Macromolecular architecture in eukaryotic cells visualized by cryoelectron tomography. *Science*. 298:1209-1213.

Megraw, T.L., L.R. Kao, and T.C. Kaufman. 2001. Zygotic development without functional mitotic centrosomes. *Curr Biol*. 11:116-120.

Meluh, P.B., and M.D. Rose. 1990. KAR3, a kinesin-related gene required for yeast nuclear fusion. *Cell*. 60:1029-1041.

Miki, H., Y. Okada, and N. Hirokawa. 2005. Analysis of the kinesin superfamily: insights into structure and function. *Trends Cell Biol*. 15:467-476.

Milligan, R.A., and P.F. Flicker. 1987. Structural relationships of actin, myosin, and tropomyosin revealed by cryo-electron microscopy. *J Cell Biol*. 105:29-39.

Mitchison, T.J. 1993. Localization of an exchangeable GTP binding site at the plus end of microtubules. *Science*. 261:1044-1047.

Miyamoto, D.T., Z.E. Perlman, K.S. Burbank, A.C. Groen, and T.J. Mitchison. 2004. The kinesin Eg5 drives poleward microtubule flux in Xenopus laevis egg extract spindles. *J Cell Biol*. 167:813-818.

Mountain, V., C. Simerly, L. Howard, A. Ando, G. Schatten, and D.A. Compton. 1999. The kinesin-related protein, HSET, opposes the activity of Eg5 and cross-links microtubules in the mammalian mitotic spindle. *J Cell Biol*. 147:351-366.

Naik, R.R., S.J. Stringer, G. Agarwal, S.E. Jones, and M.O. Stone. 2002. Biomimetic synthesis and patterning of silver nanoparticles. *Nat Mater*. 1:169-172.

Nicastro, D., A.S. Frangakis, D. Typke, and W. Baumeister. 2000. Cryo-electron tomography of neurospora mitochondria. *J Struct Biol*. 129:48-56.

Nicastro, D., C. Schwartz, J. Pierson, R. Gaudette, M.E. Porter, and J.R. McIntosh. 2006. The molecular architecture of axonemes revealed by cryoelectron tomography. *Science*. 313:944-948.

O'Connell, M.J., P.B. Meluh, M.D. Rose, and N.R. Morris. 1993. Suppression of the bimC4 mitotic spindle defect by deletion of klpA, a gene encoding a KAR3-related kinesin-like protein in Aspergillus nidulans. *J Cell Biol*. 120:153-162.

Oladipo, A., A. Cowan, and V. Rodionov. 2007. Microtubule motor Ncd induces sliding of microtubules in vivo. *Mol Biol Cell*. 18:3601-3606.

Page, B.D., L.L. Satterwhite, M.D. Rose, and M. Snyder. 1994. Localization of the Kar3 kinesin heavy chain-related protein requires the Cik1 interacting protein. *J Cell Biol*. 124:507-519.

Page, B.D., and M. Snyder. 1992. CIK1: a developmentally regulated spindle pole body-associated protein important for microtubule functions in Saccharomyces cerevisiae. *Genes Dev*. 6:1414-1429.

Pettersen, E.F., T.D. Goddard, C.C. Huang, G.S. Couch, D.M. Greenblatt, E.C. Meng, and T.E. Ferrin. 2004. UCSF Chimera - a visualization system for exploratory research and analysis. *J Comput Chem*. 25:1605-1612.

Rank, K.C., J.C. Chen, J. Cope, K. Porche, A. Hoenger, S.P. Gilbert, and I. Rayment. Intramolecular communication within the kinesin Kar3Vik1 heterodimer: Kar3Vik1 dances rather than steps. *Submitted*.

Rice, S., A.W. Lin, D. Safer, C.L. Hart, N. Naber, B.O. Carragher, S.M. Cain, E. Pechatnikova, E.M. Wilson-Kubalek, M. Whittaker, E. Pate, R. Cooke, E.W. Taylor, R.A. Milligan, and R.D. Vale. 1999. A structural change in the kinesin motor protein that drives motility. *Nature*. 402:778-784.

Roof, D.M., P.B. Meluh, and M.D. Rose. 1992. Kinesin-related proteins required for assembly of the mitotic spindle. *J Cell Biol*. 118:95-108.

Sablin, E.P., R.B. Case, S.C. Dai, C.L. Hart, A. Ruby, R.D. Vale, and R.J. Fletterick. 1998. Direction determination in the minus-end-directed kinesin motor ncd. *Nature*. 395:813-816.

Sachse, C., J.Z. Chen, P.D. Coureux, M.E. Stroupe, M. Fandrich, and N. Grigorieff. 2007. High-resolution electron microscopy of helical specimens: a fresh look at tobacco mosaic virus. *J Mol Biol*. 371:812-835.

Salunke, D.M., D.L. Caspar, and R.L. Garcea. 1986. Self-assembly of purified polyomavirus capsid protein VP1. *Cell*. 46:895-904.

Sandblad, L., K.E. Busch, P. Tittmann, H. Gross, D. Brunner, and A. Hoenger. 2006. The Schizosaccharomyces pombe EB1 homolog Mal3p binds and stabilizes the microtubule lattice seam. *Cell*. 127:1415-1424.

Sardar, R., and J.S. Shumaker-Parry. 2011. Spectroscopic and microscopic investigation of gold nanoparticle formation: ligand and temperature effects on rate and particle size. *J Am Chem Soc*. 133:8179-8190.

Saunders, W.S., and M.A. Hoyt. 1992. Kinesin-related proteins required for structural integrity of the mitotic spindle. *Cell*. 70:451-458.

Schliwa, M. 2003. Kinesin: walking or limping? *Nat Cell Biol*. 5:1043-1044.

Schroeter, J.P., and J.P. Bretaudiere. 1996. SUPRIM: easily modified image processing software. *J Struct Biol*. 116:131-137.

Sharp, D.J., G.C. Rogers, and J.M. Scholey. 2000. Microtubule motors in mitosis. *Nature*. 407:41-47.

Sharp, D.J., K.R. Yu, J.C. Sisson, W. Sullivan, and J.M. Scholey. 1999. Antagonistic microtubule-sliding motors position mitotic centrosomes in Drosophila early embryos. *Nat Cell Biol*. 1:51-54.

Sindelar, C.V., and K.H. Downing. 2007. The beginning of kinesin's force-generating cycle visualized at 9-A resolution. *J Cell Biol*. 177:377-385.

Skiniotis, G., T. Surrey, S. Altmann, H. Gross, Y.H. Song, E. Mandelkow, and A. Hoenger. 2003. Nucleotide-induced conformations in the neck region of dimeric kinesin. *EMBO J*. 22:1518-1528.

Slocik, J.M., M.O. Stone, and R.R. Naik. 2005. Synthesis of gold nanoparticles using multifunctional peptides. *Small*. 1:1048-1052.

Sokolova, A.V., L. Kreplak, T. Wedig, N. Mucke, D.I. Svergun, H. Herrmann, U. Aebi, and S.V. Strelkov. 2006. Monitoring intermediate filament assembly by small-angle x-ray scattering reveals the molecular architecture of assembly intermediates. *Proc Natl Acad Sci U S A*. 103:16206-16211.

Song, H., and S.A. Endow. 1996. Binding sites on microtubules of kinesin motors of the same or opposite polarity. *Biochemistry*. 35:11203-11209.

Song, H., and S.A. Endow. 1998. Decoupling of nucleotide- and microtubule-binding sites in a kinesin mutant. *Nature*. 396:587-590.

Song, Y.H., and E. Mandelkow. 1993. Recombinant kinesin motor domain binds to beta-tubulin and decorates microtubules with a B surface lattice. *Proc Natl Acad Sci U S A*. 90:1671-1675.

Sosa, H., D.P. Dias, A. Hoenger, M. Whittaker, E. Wilson-Kubalek, E. Sablin, R.J. Fletterick, R.D. Vale, and R.A. Milligan. 1997a. A model for the microtubule-Ncd motor protein complex obtained by cryo-electron microscopy and image analysis. *Cell*. 90:217-224.

Sosa, H., A. Hoenger, and R.A. Milligan. 1997b. Three different approaches for calculating the three-dimensional structure of microtubules decorated with kinesin motor domains. *J Struct Biol*. 118:149-158.

Sproul, L.R., D.J. Anderson, A.T. Mackey, W.S. Saunders, and S.P. Gilbert. 2005. Cik1 targets the minus-end kinesin depolymerase kar3 to microtubule plus ends. *Curr Biol*. 15:1420-1427.

Stehle, T., S.J. Gamblin, Y. Yan, and S.C. Harrison. 1996. The structure of simian virus 40 refined at 3.1 A resolution. *Structure*. 4:165-182.

Subramanian, R., E.M. Wilson-Kubalek, C.P. Arthur, M.J. Bick, E.A. Campbell, S.A. Darst, R.A. Milligan, and T.M. Kapoor. 2010. Insights into antiparallel microtubule crosslinking by PRC1, a conserved nonmotor microtubule binding protein. *Cell*. 142:433-443.

Tilney, L.G., J. Bryan, D.J. Bush, K. Fujiwara, M.S. Mooseker, D.B. Murphy, and D.H. Snyder. 1973. Microtubules: evidence for 13 protofilaments. *J Cell Biol*. 59:267-275.

Tokai, N., A. Fujimoto-Nishiyama, Y. Toyoshima, S. Yonemura, S. Tsukita, J. Inoue, and T. Yamamota. 1996. Kid, a novel kinesin-like DNA binding protein, is localized to chromosomes and the mitotic spindle. *EMBO J*. 15:457-467.

Troxell, C.L., M.A. Sweezy, R.R. West, K.D. Reed, B.D. Carson, A.L. Pidoux, W.Z. Cande, and J.R. McIntosh. 2001. pkl1(+)and klp2(+): Two kinesins of the Kar3 subfamily in fission yeast perform different functions in both mitosis and meiosis. *Mol Biol Cell*. 12:3476-3488.

Turner, J., R. Anderson, J. Guo, C. Beraud, R. Fletterick, and R. Sakowicz. 2001. Crystal structure of the mitotic spindle kinesin Eg5 reveals a novel conformation of the neck-linker. *J Biol Chem*. 276:25496-25502.

Vale, R.D., and R.J. Fletterick. 1997. The design plan of kinesin motors. *Annu Rev Cell Dev Biol*. 13:745-777.

Vale, R.D., T.S. Reese, and M.P. Sheetz. 1985. Identification of a novel force-generating protein, kinesin, involved in microtubule-based motility. *Cell*. 42:39-50.

Valentine, M.T., P.M. Fordyce, and S.M. Block. 2006. Eg5 steps it up! *Cell Div*. 1:31.

Vanhecke, D., S. Asano, Z. Kochovski, R. Fernandez-Busnadiego, N. Schrod, W. Baumeister, and V. Lucic. 2010. Cryo-electron tomography: methodology, developments and biological applications. *J Microsc*. 242:221-227.

Varga, V., C. Leduc, V. Bormuth, S. Diez, and J. Howard. 2009. Kinesin-8 motors act cooperatively to mediate length-dependent microtubule depolymerization. *Cell*. 138:1174-1183.

Verhey, K.J., and J.W. Hammond. 2009. Traffic control: regulation of kinesin motors. *Nat Rev Mol Cell Biol*. 10:765-777.

Walczak, C.E., I. Vernos, T.J. Mitchison, E. Karsenti, and R. Heald. 1998. A model for the proposed roles of different microtubule-based motor proteins in establishing spindle bipolarity. *Curr Biol*. 8:903-913.

Walker, R.A., E.D. Salmon, and S.A. Endow. 1990. The Drosophila claret segregation protein is a minus-end directed motor molecule. *Nature*. 347:780-782.

Wendt, T.G., N. Volkmann, G. Skiniotis, K.N. Goldie, J. Muller, E. Mandelkow, and A. Hoenger. 2002. Microscopic evidence for a minus-end-directed power stroke in the kinesin motor ncd. *EMBO J*. 21:5969-5978.

Whittaker, M., B.O. Carragher, and R.A. Milligan. 1995. PHOELIX: a package for semi-automated helical reconstruction. *Ultramicroscopy*. 58:245-259.

Wittinghofer, A. 1997. Signaling mechanistics: aluminum fluoride for molecule of the year. *Curr Biol*. 7:R682-685.

Woehlke, G., A.K. Ruby, C.L. Hart, B. Ly, N. Hom-Booher, and R.D. Vale. 1997. Microtubule interaction site of the kinesin motor. *Cell*. 90:207-216.

Xie, J., J.K. Lee, and D.I.C. Wang. 2007. Seedless, surfactantless, high-yield synthesis of branched gold nanocrystals in HEPES buffer solution. *Chem. Mater.* 19:2823-2830.

Xiong, Q., M.K. Morphew, C.L. Schwartz, A.H. Hoenger, and D.N. Mastronarde. 2009. CTF determination and correction for low dose tomographic tilt series. *J Struct Biol*. 168:378-387.

Yildiz, A., M. Tomishige, R.D. Vale, and P.R. Selvin. 2004. Kinesin walks hand-over-hand. *Science*. 303:676-678.

Yun, M., C.E. Bronner, C.G. Park, S.S. Cha, H.W. Park, and S.A. Endow. 2003. Rotation of the stalk/neck and one head in a new crystal structure of the kinesin motor protein, Ncd. *EMBO J*. 22:5382-5389.

Zhang, X., L. Jin, Q. Fang, W.H. Hui, and Z.H. Zhou. 2010. 3.3 A cryo-EM structure of a nonenveloped virus reveals a priming mechanism for cell entry. *Cell*. 141:472-482.